New insights from multi-proxy data from West Antarctic drifts: Implications for dating and interpreting Late Quaternary palaeoenvironmental records from the Antarctic margin

C.-D. Hillenbrand [a,*], S.J. Crowhurst [b], M. Williams [a], D.A. Hodell [b], I.N. McCave [b], W. Ehrmann [c], C. Xuan [d], A.M. Piotrowski [b], F.J. Hernández-Molina [e], A.G.C. Graham [f,g], H. Grobe [h], T.J. Williams [a,b,i], J.R. Horrocks [j], C.S. Allen [a] & R.D. Larter [a]

[a] British Antarctic Survey, High Cross, Madingley Road, Cambridge CB3 0ET, UK

[b] Department of Earth Sciences, University of Cambridge, Downing Street, Cambridge, CB2 3EQ, UK

[c] Insitute for Geophysics and Geology, University of Leipzig, Talstrasse 35, Leipzig 04103, Germany

[d] School of Ocean and Earth Science, National Oceanography Centre Southampton, University of Southampton, Waterfront Campus, European Way, Southampton SO14 3ZH, UK

[e] Department of Earth Sciences, Royal Holloway University of London, Egham, Surrey TW20 0EX, UK

[f] College of Life and Environmental Sciences, University of Exeter, Exeter EX4 4RJ, UK

[g] College of Marine Science, University of South Florida, St Petersburg, Florida, USA

[h] Alfred-Wegener-Institut Helmholtz-Zentrum für Polar- und Meeresforschung, Bremerhaven, Germany

[i] Department of Geological Sciences, University of Florida, Gainesville, Florida, USA

[j] Department of Geography, Durham University, Durham DH1 3LE, UK

*corresponding author:

Dr. Claus-Dieter Hillenbrand

phone: ++44 (0)1223 221340; fax: ++44 (0)1223 221646

email: hilc@bas.ac.uk

Abstract

The Antarctic Peninsula's Pacific margin is one of the best studied sectors of the Antarctic continental margin. Since the 1990s, several research cruises have targeted large sediment drifts on the continental rise with geophysical surveys, conventional coring and deep-sea drilling. The previous studies highlighted the potential of the drift sediments as high-resolution palaeoenvironmental archives. However, these studies also suffered from chronological difficulties arising from the lack of calcareous microfossils, with initial results from geomagnetic relative palaeointensity (RPI) dating promising a possible solution.

This paper presents data from new sediment cores recovered on cruise JR298 from seven continental rise sites west of the Antarctic Peninsula and in the Bellingshausen Sea with the objectives to (i) seek calcareous foraminifera at shallow drift sites to constrain RPI-based age models, and (ii) investigate the depositional history at these locations. We present the results of chronological and multi-proxy analyses on these cores and two cores previously collected from the study area. We establish new age models for the JR298 records and compare them with published RPI-based age models. In addition, we evaluate the reliability of different palaeoproductivity proxies and reconstruct depositional processes.

Planktic foraminifera are present in various core intervals. Although their stable oxygen isotope ($\delta^{18}O$) ratios, tephrochronological constraints and glacial-interglacial changes in sediment composition provide age models largely consistent with the RPI chronologies, we also observe distinct differences, predominantly in the Bellingshausen Sea cores. Enrichments of solid-phase manganese together with evidence for "burn-down" of organic carbon in late glacial and interglacial sediments document non-steady-state diagenesis that may have altered magnetic mineralogy and, thus, RPI proxies. This process may explain discrepancies between age models based on RPI and derived from $\delta^{18}O$ data combined with tephrochronology. The data also indicate that organic carbon is a much less reliable productivity proxy than biogenic barium or organically-associated bromine in the investigated sediments.

In agreement with previous studies, sediment facies indicates strong control of drift deposition by bottom-current activity and supply of glacigenic detritus via gravitational transport. Bottom-current velocities underwent only minor changes over glacial-interglacial cycles at the drift crests, with down-slope deposition occasionally affecting

even the shallowest drift locations. Maximum concentrations of coarse iceberg-rafted debris (IRD) at the seafloor surfaces of the shallow sites result from upward pumping caused by extensive bioturbation. This process has to be taken into account when past changes in IRD deposition are inferred from quantifying clasts >1 mm in size.

Keywords: Antarctic Peninsula; bioturbation; bottom current; carbon burn-down; contourites; ice-rafted debris; manganese enrichment; non-steady-state diagenesis; sediment drifts

1. Introduction

The western continental rise of the Antarctic Peninsula is characterized by eight large and four smaller mounds rising between several hundred and ≤2000 meters above the surrounding seafloor (Fig. 1; Rebesco et al. 1998, 2002; Hillenbrand et al. 2008b; Hernández-Molina et al. 2017). The mounds are separated by deep-sea channels originating at the base of the continental slope, and most of them have a gentle NE side and a steep SW flank. They are interpreted as contourite mounded drifts formed by fine-grained detritus, which initially had been supplied by turbidity currents travelling through the channels before the fine-grained particles were entrained into a generally SW-ward flowing bottom current (Rebesco et al. 1996, 1997) [NB: here we use the term "contourite" *sensu lato*, i.e., as describing any sediment deposited or reworked by a bottom current (e.g., Rebesco et al. 2014; Stow & Smillie 2020)]. The bottom current follows the bathymetric contours and originates as highly modified Weddell Sea Deep Water (WSDW) or Lower Circumpolar Deep Water (LCDW) from the Weddell Sea (Camerlenghi et al. 1997; Giorgetti et al. 2003). The drifts were examined with high-resolution bathymetric surveys (Rebesco et al. 2002, 2007; Dowdeswell et al. 2004; Larter et al. 2016), reflection seismic investigations (Larter & Cunningham 1993; McGinnis et al. 1997; Rebesco et al. 1997, 2002; Hernández-Molina et al. 2006, 2017; Scheuer et al. 2006) and shallow gravity and piston coring (Pudsey & Camerlenghi 1998; Pudsey 2000; Lucchi et al. 2002; Vautravers et al. 2013). In addition, Drifts 7 and 4 were drilled at sites 1095, 1096 and 1101 by Ocean Drilling Program (ODP) Leg 178 (Barker et al. 1999, 2002).

Further west, the continental margin in the Bellingshausen Sea has been only sparsely studied by a few high-resolution bathymetric lines and seismic profiles. These surveys identified the Belgica Trough Mouth Fan ('Belgica TMF'; Dowdeswell et al. 2008; Graham et al. 2011; Gales et al. 2018) and one major sediment drift (Nitsche et al. 2000; Cunningham et al. 2002). In contrast to the Antarctic Peninsula rise, data from only two marine sediment cores have been published from the continental rise in the Bellingshausen Sea (PS2538, Hillenbrand et al. 2005, 2009; PS2556, Hillenbrand et al. 2008a) (Fig. 1).

Multi-proxy analyses of the sediment cores from the Antarctic Peninsula margin revealed that the drift bodies contain records of Late Neogene to Quaternary palaeoenvironmental changes, including past dynamics of the Antarctic Peninsula Ice

Sheet (APIS) and oceanographic variability in the Antarctic Zone of the Southern Ocean (e.g., Pudsey 2000; Lucchi et al. 2002; Barker et al. 2002; Cortese et al. 2004; Hillenbrand & Ehrmann 2005; Bart et al. 2007; Cowan et al. 2008; Hepp et al. 2006, 2009; Escutia et al. 2009). The rarity of calcareous microfossils in the predominantly terrigenous drift sediments prevented acquisition of reliable AMS ^{14}C ages and the application of stable oxygen isotope (δ^{18}O) stratigraphy; the cores could only be dated by lower-resolution bio-, magneto- and lithostratigraphy (Pudsey & Camerlenghi 1998; Pudsey 2000; Barker et al. 2002; Lucchi et al. 2002). This difficulty hampered high-resolution palaeoenvironmental reconstructions and thus exploitation of the full potential of the drift archives. Nevertheless, establishing age models for the drift cores by correlating reconstructions of relative palaeointensity (RPI) with independently dated regional/global RPI records has shown some promise (Guyodo et al. 2001; Sagnotti et al. 2001; Macrì et al. 2006; Venuti et al. 2011; Vautravers et al. 2013).

International Ocean Discovery Program (IODP) proposal 732-FULL2 (Channell et al. 2008) advocated the recovery of new drill cores spanning the Neogene and Quaternary from the western Antarctic Peninsula drifts and the Bellingshausen Sea. Its primary objective is to exploit the full potential of the drifts' palaeo-archives for reconstructing Miocene to Holocene oceanographic changes in the eastern Pacific sector of the Southern Ocean and the dynamics of the APIS and the marine based West Antarctic Ice Sheet (WAIS). The strategy is to obtain continuous records from shallow drift crest sites, where both accumulation rates and the preservation potential of calcareous foraminifera are expected to be high, in order to establish reliable, high-resolution age models using RPI proxies constrained by foraminiferal δ^{18}O stratigraphy.

Here, we present multi-proxy data sets from sediment cores recovered from the West Antarctic drifts during pre-site survey cruise JR298 in support of IODP proposal 732-FULL2 and two additional cores collected on earlier research cruises. The RPI records of the JR298 cores together with supporting data for some of those cores, were recently published by Channell et al (2019). Here, we present the sedimentological data sets, including the results of proxy analyses, such as measurements of sortable silt mean size ($\overline{SS}$) and X-ray fluorescence (XRF) scanning, which previously had not - or only to a very limited extent - been carried out on cores from the area. We focus our discussion on novel findings from these investigations.

2. Materials and methods

2.1. Materials

Seven piston cores (PC) paired with giant box cores (GBC) were recovered on IODP pre-site survey investigation cruise JR298 of the RRS *James Clark Ross* in austral summer 2015 (Table 1). Six of the PC deployments targeted drill sites of IODP proposal 732-FULL2 (Channell et al. 2008), i.e. the shallowest parts of Drifts 4, 5, 6 and 7 on the western Antarctic Peninsula rise, the Bellingshausen Sea drift, and the distal part of Belgica TMF (Fig. 1). In addition, PC734/GBC735 was deployed on the distal crest of Drift 5 to obtain a more condensed sedimentary sequence, and GBC733 was retrieved from the channel separating Drifts 5 and 5A (Fig. 1).

The PCs were collected using a piston coring system with a short, small-diameter trigger corer (TC). At most sites it was unclear, whether the TC had over-penetrated the seabed, so a GBC was deployed at each PC site to obtain undisturbed seafloor surface sediments. Data from GBC sub-cores and the corresponding PCs were spliced to compensate for sediment loss and/or possible core-top disturbance in the PCs. Overall, PC quality was excellent, with only minor core-top disturbance/sediment loss. However, X-radiographs revealed sediment inflow at the bases of several PCs, which is a common issue in piston coring (e.g., Skinner & McCave 2003). No data are presented (or were collected) from the corresponding core intervals. The PCs were cut into 1.5 m long sections and, together with the GBC sub-cores, split and sampled on board. All core sections and samples were stored at +4 °C after collection.

We also present data from gravity cores (GCs) PS1565-2 and PS2556-2 [including multiple core (MUC) PS2556-1], which were recovered during RV *Polarstern* cruises ANT-VI/2 (1987) and ANT-XI/3 (1994), respectively (Fig. 1; Table 1). PS1565-2 was recovered from the seaward, distal flank of Drift 3, and PS2556-2/-1 was collected from the crest of the Bellingshausen Sea drift, which was later targeted by JR298 core PC726. Some data from cores PS1565-2 and PS2556-2/-1 were previously published (Hillenbrand & Ehrmann 2002; Hillenbrand & Fütterer 2002; Hillenbrand et al. 2003, 2008a; Hillenbrand & Cortese 2006; Turney et al. 2020).

2.2. Methods

Whole-core magnetic susceptibility (MS) was measured on the PC sections using a 120-mm diameter Bartington loop sensor (MS2C) connected to a Bartington MS3 susceptibility meter. Afterwards, the PC and GBC sections were split on board using a router and a fishing line. Their working and archive halves were photographed before the lithology and sedimentary structures of the cores were described visually and using smear slides. After cruise JR298, the core logs were refined/revised using X-radiographs prepared from the PC and GBC archive halves. P-wave velocity, MS and wet-bulk density (WBD) of the archive halves were analysed with a GEOTEK multi-sensor core logger (MSCL-S). Semi-quantitative elemental data as well as diffuse-reflectance spectrophotometric data were measured on the archive halves of the PCs and GBCs using a 3rd generation Avaatech XRF scanner. Elemental data are recalculated and plotted as log-normalized (LN) peak-area ratios following Weltje & Tjallingii (2008) but in the following text we refer just to element ratios. Methodological details for the XRF scanning as well as for magnetic investigations, which were conducted on U-channels taken from the PC working halves and discrete bulk samples taken from the PCs and GBCs, are given in Channell et al. (2019).

Discrete 1-cm thick bulk samples (~48 cm^3) were taken from the PC and GBC working halves for post-cruise sedimentological, micropalaeontological, geochemical and mineralogical studies. The sampling intervals varied depending on the visually observed changes in core lithology and sedimentary structures. Water content was determined by weighing the samples before and after oven drying at 30 °C. Grain-size distribution in terms of weight percentages of gravel (>2000 µm), sand (63-2000 µm) and mud (<63 µm) was analysed on all cores by wet sieving over 63 µm and subsequent dry sieving of the retained coarse fraction over 2 mm. Given the limited sample volume of ~48 cm^3, the gravel percentages determined for gravel-rich samples have to be considered as semi-quantitative contents (e.g., Head 2006). Siliceous and calcareous biogenic components were removed from the mud fractions of cores PC727 and PC734 using 2M sodium carbonate and 1M dilute acetic acid, respectively, before their detailed grain-size distribution was measured with a Coulter Counter Multisizer-3 (MS3), to determine the mean grain size of terrigenous particles in the sortable silt fraction 10-63 µm ($\overline{SS}$) as a proxy for bottom-current speed (McCave et al. 1995, 2017; McCave & Hall 2006). The $\overline{SS}$ signal in marine sediments from polar regions can be affected by deposition of ice-rafted debris (IRD) (e.g. Hass 2002; McCave et al. 2014; McCave & Andrews 2019). In order to evaluate the IRD influence on $\overline{SS}$ of cores PC727 and PC734, percentage of sortable silt (SS%) in the fine fraction <63 µm was determined on selected samples by conducting a “one shot” pipette analysis at 10 µm threshold on the wet-sieved fine fraction. The mineralogical composition of the clay fraction (<2 µm) of cores PC727 and PC734 was investigated by X-ray diffraction (XRD), applying procedures outlined in Hillenbrand et al. (2009) and Ehrmann et al. (2011).

Geochemical analyses on discrete samples included the measurements of total carbon (TC) and total inorganic carbon (TIC) for determining the contents of $CaCO_3$ and total organic carbon (TOC). TIC content was measured by acidifying the samples with an Auto-MateFX carbonate preparation system and measuring evolved CO_2 with a UIC Coulometrics TM5011 CO_2 coulometer, and TC content was measured via combustion in a Flash Element Analyser (EA). TC and TOC were analysed on all samples from cores PC727, PC728 and PC734 and samples from distinct intervals in cores PC723, PC726, PC732 and PC736, which had been chosen based on the core descriptions. XRF measurements of major and trace element concentrations were conducted on selected discrete samples from cores PC723 and PC727 using an XRF spectrometer. The main purpose of the discrete XRF analyses was to establish, whether particular elemental ratios commonly used as palaeo-proxies in marine sediments, such as the productivity proxies barium/aluminium (Ba/Al) and bromine/aluminium (Br/Al) (e.g., Hillenbrand et al. 2017; Smith et al. 2017), showed identical down-core trends in the XRF data from discrete samples and scanning.

Stable oxygen ($\delta^{18}O$) and carbon ($\delta^{13}C$) isotope ratios using the VPDB standard on tests of the planktic foraminifera *Neogloboquadrina pachyderma* sinistral picked from the coarse fraction (>63 µm) of all samples containing sufficient tests in cores PC727, PC728, PC734 and PC736 and selected intervals in cores PC723 and PC727 were analysed with a Thermo-Finnigan MAT 253 mass spectrometer (2-26 tests per sample were picked, 10-12 tests were analysed on most samples). Age models for the cores were established by correlating the $\delta^{18}O$ data of a core with the Marine Isotope Stages (MIS) of the LR04 benthic foraminifera $\delta^{18}O$ stack (Lisiecki & Raymo 2005). Marine Tephra B, a widespread tephra layer, which originates from a Plinian eruption of the Mt. Berlin volcano in Marie Byrd Land, West Antarctica, identified in both West Antarctic marine sediment cores and Antarctic ice cores, was used as a marker for the MIS 5/MIS 6 boundary at ~130 ka (Hillenbrand et al. 2008a). Recently, an age of 130.7±1.8 ka has been assigned to Marine Tephra B based on its identification in the Dome Fuji ice core in East Antarctica (Turney et al. 2020), which is, within error, consistent with age estimates from previously RPI-dated sediment cores from Drift 7 (Macrì et al. 2006; Hillenbrand et al. 2008a; Venuti et al. 2011).

Seabed surface sediments of box cores GBC729 and GBC735 contained enough planktic foraminifera and other calcareous fossils to apply AMS ^{14}C dating (Table 2). Four samples from GBC729 and two samples from GB735 were dated at Beta Analytic Inc., Miami, U.S.A., for testing the hypothesis that the frequent occurrence of manganese-coated pebbles and cobbles at the surfaces of the JR298 GBCs resulted from current winnowing/non deposition.

Proxies on GCs PS1565-2 and PS2556-2 (incl. MUC PS2556-1) were investigated following the methods detailed in Hillenbrand & Ehrmann (2002), Hillenbrand & Fütterer (2002) and Hillenbrand et al. (2002, 2003, 2005). In addition, we present for the GCs percentages of microfossils, micro-manganese nodules and volcanic glass particles determined by identifying and counting 200-400 grains of the sand fraction (>63 µm) under a microscope (Hillenbrand 1994; Braun 1997). Notable differences between the investigations on the two GCs and the JR298 cores are that on the former cores (i) samples were decalcified before grain-size analysis, and (ii) IRD abundance was determined on X-radiographs by counting gravel-sized clasts (>2 mm) continuously down-core at 1 cm depth intervals (Grobe 1987).

All data are available under doi:10.1594/PANGAEA.[*doi to be assigned after acceptance*].

3. Results

Down-core data for all records (apart from GBC733) are shown in Figures 2-13 and (apart from PS1565-2) are plotted versus centimetres composite depth (cmcd). The splicing of the PCs with the GBCs was conducted by visual correlation of (i) distinct lithological and structural features, and (ii) characteristic down-core changes and/or prominent peaks in physical properties, XRF scanner data, water content, TOC and $CaCO_3$ contents, and grain-size composition. The following splicing depths were determined: PC723 20 cm =GBC724 28 cm; PC726 20 cm =GBC725 32 cm; PC727 20 cm =GBC730 17 cm; PC728 10 cm =GBC729 7 cm; PC732 17 cm =GBC731 17 cm; PC734 10 cm =GBC735 15 cm; and PC736 9 cm =GBC722 15 cm. The splicing indicates sediment loss in the PCs of between 0 and 12 cm, with GBC729 and GBC730 having been affected by some degree of sediment compression during sub-core retrieval. GBC data were used above and PC data below the established splicing depths to account for potential core-top disturbance in the PCs. Loss of ~13 cm of seafloor surface sediment in GC PS2556-2 was compensated for by splicing its data with those of MUC PS2556-1 (Braun 1997). In the following, only the JR298 PC numbers and site numbers PS1565 and PS2556 are used for the spliced core records, if not stated otherwise.

Site GBC733 from the channel between Drifts 5 and 5A was the only site on cruise JR298, where only a box core was collected. GBC733 recovered a disturbed, only 28 cm long, succession consisting of ~21 cm of bioturbated, diatom-bearing to diatomaceous mud overlying ~7 cm of laminated coarse silt and fine sand (Suppl. Fig. 1). No data are presented here for this core.

3.1. Lithology and sedimentary structures

The recovered sedimentary sequences in all cores consist predominantly of terrigenous muds and sandy muds, with low and variable contents of sand and gravel (Figs. 2-10). Most of the core intervals are laminated to stratified and characterized by up to several centimetres thick, internally structureless muddy horizons alternating with horizontal, silty to sandy layers. These coarser layers are often internally structureless, but occasionally laminated or stratified. Rarely, they are fining upwards and/or have an erosional base. Sediment intervals containing diatoms and/or foraminifera (nearly exclusively the planktic foraminifer *N. pachyderma* sin.) occur in all cores, and always bear scattered gravel grains. These microfossil-bearing sediments are usually bioturbated or structureless, with their thicknesses ranging from just under 10 cm to 45 cm. All cores retrieved such sediments at their tops, with another microfossil-bearing and bioturbated to homogenous interval occurring further down-core at sites PC726, PC727, PC734 and PS1565, and two such intervals occurring further down-core at sites PC723 and PS2556 (Figs. 2-4, 7, 9, 10).

Subordinate sedimentary structures include cross lamination, observed only once, in a thin interval of core PC734 (305-310 cmcd), and deformation structures, which are largely restricted to site PC732. The deformation structures comprise inclination, sloping, faulting and fanning of coarse- and fine-grained layers as well as convolute bedding. One horizon at site PC732 contained a slab of semi-consolidated sand that is orientated obliquely to the core axis. The structures are embedded between horizontally laminated and stratified intervals and are therefore considered to be primary features rather than coring or splitting artefacts.

A tephra layer sitting stratigraphically just below the second microfossil-bearing interval from the surface was found in cores PC727 and PC734 (Figs. 4, 7). In core PC734 the tephra formed a ~4 cm thick, bioturbated macroscopic bed (1153-1157 cmcd), whereas it was recognizable as a microscopic or “disseminated” tephra layer in core PC727. Tephra layers invisible to the naked eye, identified by microscopic investigations of smear slides or extracted grain-size fractions, are nowadays referred to as “cryptotephra” (e.g. Davies 2015). Notwithstanding the recent claim by Di Roberto et al. (2019), such microscopic/dispersed tephra layers originating from distinct individual volcanic eruptions have been identified in Antarctic marine sediment cores since at least the 1970s (e.g., Huang et al. 1975, Kyle & Seward 1984, Shane & Froggatt 1992, Moreton & Smellie 1998), with both micro- and macroscopic tephra layers having been reported from cores from the western Antarctic Peninsula margin and the Bellingshausen Sea, including cores PS2556 and PS1565 (Figs. 9, 10; Hillenbrand et al. 2008a and references therein). A series of sand fraction samples taken from cores PC723 and PC726 at a similar stratigraphic positions, where the tephra layer in cores PC727 and PC734 had been detected, were investigated under a microscope for the presence of volcanic particles. However, only in core PC726 were glass shards detected in low concentrations (<5%) from 532 to 535 cmcd.

3.2. Physical properties and grain size

Pronounced down-core changes in magnetic susceptibility, WBD and water content reflect predominantly the major lithological changes, i.e. the alternations between biogenic, bioturbated/homogenous sediments and laminated/stratified terrigenous sediments. Thereby, magnetic susceptibility and WBD display minima and water content displays maxima in the biogenic sediment intervals (Figs. 2-10). Individual magnetic susceptibility and WBD peaks correlate either with individual large (mafic) gravel grains or, within the terrigenous intervals, with discrete coarse-grained layers.

Overall, sand and gravel concentrations are low in the studied cores, but coarse-grained particles are consistently elevated in the biogenic intervals. Notably, the seafloor surface sediments at all JR298 sites except PC727 display absolute maxima in gravel concentrations, associated with elevated sand contents. Even in the core-top sediments at site PC727 gravel and sand contents are considerably increased. This finding is corroborated by photographs of the GBC surfaces showing dispersed, manganese-coated gravel grains and pebbles (Fig. 14; Suppl. Fig. 1).

$\overline{SS}$ in core PC727 varies from 19 to 22 µm within both the biogenic intervals and the terrigenous interval directly underlying the lower biogenic interval. In the other terrigenous interval $\overline{SS}$ predominantly ranges from 16-19 µm (Fig. 4). In contrast, $\overline{SS}$ in core PC734 varies mainly between 16 and 21 µm, without showing a clear difference between biogenic and terrigenous intervals (Fig. 7). However, similar to the gravel content, $\overline{SS}$ reaches an absolute maximum in the (near-)surface sediments at site PC734 (>22 µm). Furthermore, the tephra layer in core PC734 is characterized by relative sand and $\overline{SS}$ maxima (Fig. 7).

A positive correlation is recorded between $\overline{SS}$ and SS% for samples from cores PC727 and PC734 (Suppl. Fig. 2), with a coefficient R of 0.74 indicating a significant correlation for PC727. In this core, just a single data point is responsible for reducing R from 0.93 to 0.74. In contrast, the data for PC734 show more scatter, with R of only 0.53, which is probably caused by the presence of unsorted iceberg-delivered silt and clay (e.g., McCave & Hall 2006). According to McCave & Andrews (2019), a running down-core correlation coefficient R_{run} of >0.5 is required for interpreting the $\overline{SS}$ of IRD-influenced sediments as a record of bottom-current speed.

3.3. Geochemical parameters and clay mineral composition

$CaCO_3$ concentration reaches its maxima at the seafloor surfaces of most sites (Figs. 2-13). Exceptions are PC734 from 3000 m and PS1565 from 3427 m water depth, which are the deepest sites west of the Antarctic Peninsula. At present, the water depth of the Calcite Compensation Depth (CCD) has been suggested to drop westwards from ~2800 m water depth on the Antarctic Peninsula margin to ~3000 m in the southern Bellingshausen Sea (Hillenbrand et al. 2003). In many cores $CaCO_3$ concentrations decrease to nearly zero immediately below the surface maximum but in some cores, such as PC728 and PS1565, they remain slightly, but continuously elevated (≥0.5 wt.%) in the underlying terrigenous interval, thereby showing a minor down-core increase (Figs. 5, 10). In the sub-surface biogenic intervals of cores PC723, PC726, PC727, PC734, PS2556 the $CaCO_3$ concentrations are considerably higher (Figs. 2-4, 7, 9). Similar $CaCO_3$ down-core patterns were previously reported from core PS1565 (Fig. 10; Hillenbrand & Fütterer 2002) and other sediment cores west of the Antarctic Peninsula (Pudsey & Camerlenghi 1998; Pudsey 2000).

Similarly to the $CaCO_3$ content, TOC content decreases immediately down-core beneath a maximum concentration at the seafloor surface at most sites. However, TOC remains elevated in the underlying terrigenous intervals of cores PC727, PC728, PC734 and PS2556 (Figs. 4, 5, 7, 9). In core PC734 the $CaCO_3$ maximum above its base coincides with a TOC maximum (Fig. 7). This contrasts with cores PC723, PC726, PC727 and PS2556, in which these down-core $CaCO_3$ maxima coincide with TOC minima (Figs. 2-4, 9, 11).

Biogenic barium (Ba_{bio}) is considered the most reliable palaeoproductivity proxy in Late Quaternary sediments recovered south of the Antarctic Polar Front (e.g., Nürnberg et al. 1997; Bonn et al. 1998; Pudsey & Camerlenghi 1998; Hillenbrand & Cortese 2006). Consequently, barium counts measured with an XRF scanner and normalised for terrigenous input using titanium (e.g., Williams et al. 2019), iron (e.g., Lamy et al. 2014) or aluminium (e.g., Wu et al. 2017) are widely used as a proxy for Ba_{bio} in these sediments. Ba/Al ratios for the investigated cores are higher in the biogenic intervals but their maxima often lie below $CaCO_3$ maxima, especially near the seabed surface (Figs. 2-8, 10-13). Because high Ba contents in marine sediments can also result from an increased supply of detrital barite rather than increased biological productivity, we also normalised Ba with respect to zirconium (Zr), which is a proxy for zircon and thus detrital heavy minerals.

Bromine has also been proposed as a proxy for marine organic carbon content in sediment cores (e.g., Ziegler et al. 2008) and was recently applied to Antarctic marine sediments (Smith et al. 2017), including most cores studied here (Channell et al. 2019). In general, the down-core trends of the Br/Al data reflect those of the Ba/Al data at all sites with XRF scanner data (Figs. 2-8). Furthermore, the Br/Al ratios in the discrete samples from core PC727 match the Br/Al data obtained from XRF scanning (Fig. 12), indicating that the Br/Al down-core variations are unlikely to reflect changes in water content only, although water concentrations are known to influence XRF scanner data for elements dissolved in high concentrations in seawater and/or pore-water (Tjallingii et al. 2007; Ziegler et al. 2008; Hennekam & De Lange 2012).

Normalised manganese (Mn) ratios in marine sediments are commonly used as a proxy for Mn-oxide concentration, an indicator of the the oxygenation state of the bottom water at the time of deposition (e.g., Jaccard et al. 2016; Wagner & Hendy 2017; Wu et al. 2018). In most of our investigated cores, Mn/Al ratios exhibit maxima in the biogenic intervals (Figs. 2-8, 10), which is also consistent with the Mn-coating of pebbles and cobbles at the seabed surface (Fig. 14; Suppl. Fig. 1). In general, the Mn/Al ratios match the down-core patterns of the Ba/Al and Br/Al data, but, notably, they also show maxima in the terrigenous sediments directly underlying the biogenic intervals (Figs. 2-8), which is particularly evident from the abundance of micro-Mn nodules in core PS2556 (Fig. 9). Mn/Al ratios analysed on discrete samples from cores PC723 and PC727 confirm this observation (Figs. 11, 12). In core PS1565 maxima in Mn/Al ratios of bulk sediments coincide with maximum abundances of micro-Mn nodules (Figs. 10, 13).

As in core PS1565 (Fig. 10; Hillenbrand & Ehrmann 2002), clay mineral assemblages in cores PC727 and PC734 consist mainly of chlorite, illite and smectite, with only very minor contents of kaolinite (Figs. 4, 7). In the three cores, smectite tends to be higher in the biogenic intervals, whereas chlorite shows higher concentrations in the terrigenous sediments (Figs. 4, 7, 10, 15). Along the core transect, smectite generally decreases at the expense of chlorite and illite in a SW-ward direction (Fig. 15).

3.4. Chronological constraints

The planktic $\delta^{18}O$ data exhibit low values in the biogenic sediments and high values in the terrigenous intervals, with the $\delta^{13}C$ data often showing the opposite pattern (Figs. 2-10). Where resolved, the $\delta^{18}O$ shift at the transition between the biogenic interval at the core top and the underlying terrigenous sediments is ~1.5‰ (Figs. 4, 5, 7-9), corresponding to the typical global $\delta^{18}O$ shift of 1.0-1.5‰ caused by the combined effect of decreasing ice volume and ocean warming at Late Quaternary glacial terminations, which is recorded by benthic and planktic foraminifera (e.g. Imbrie et al. 1984; Lisiecki & Raymo 2005; Elderfield et al. 2012). The corresponding planktic $\delta^{13}C$ changes in our cores are on average 0.6‰, ranging from 0.3‰ (PC734) to 0.7‰ (PC727, PC728), and thus also lie within the range of typical global glacial-interglacial $\delta^{13}C$ shifts recorded by benthic foraminifera, although the entire whole-ocean change probably did not exceed 0.3±0.2‰ (e.g. Peterson et al. 2014; Gebbie et al. 2015). In the biogenic intervals of the middle and lower parts of our cores, the $\delta^{18}O$ decreases with respect to under- and overlying terrigenous sediments vary from 0.5‰ to 1.7‰, but, with an average range of 0.9‰, are generally less prominent than in the upper core sections. The corresponding $\delta^{13}C$ increases, with an average range of 0.5‰, are only slightly less prominent (Figs. 2-4, 7, 9).

AMS ^{14}C dates were obtained from calcareous epi-faunal organisms and planktic foraminifera (*N. pachyderma* sin.) from the seafloor surface sediments retrieved in core GBC729 (=PC728) and GBC735 (=PC734) (Fig. 14). For site GBC735, a bivalve shell and planktic foraminifera provided uncorrected ages of 1100 and 1000 ^{14}C yrs BP, respectively, while for site GBC729 benthic organisms and planktic foraminifera gave slightly older ages of c. 1360 and 1260 ^{14}C yrs BP, respectively (Table 2). Thus, the ages from site GBC729 match the pre-bomb marine reservoir effect (MRE) of c. 1300 ^{14}C yrs BP in the Southern Ocean, whilst those from site GBC735 lie within the pre-bomb MRE and the post-bomb MRE of c. 700 ^{14}C yrs BP (e.g. Berkman & Forman 1996; Berkman et al. 1998; Skinner et al. 2019). The dates from the planktic foraminifera are slightly younger than those from the calcareous benthos at both sites, reflecting the slightly lower MRE in Southern Ocean surface waters when compared to bottom waters (e.g., Sikes et al. 2000). In general, however, the ^{14}C dates document a recent age for the biogenic sediments at the core tops. No down-core AMS ^{14}C ages are available.

The stratigraphic positions of the tephra layers detected in cores PC727 and PC734 (Figs. 2, 7) and sand-sized glass shards found in core PC726 (532-535 cmcd) match that of Marine Tephra B in numerous cores from the study area (Hillenbrand et al. 2008a), including cores PS2556 and PS1565 (Figs. 9, 10), which has an age of 130.7±1.8 ka (Turney et al. 2020). Marine Tephra A, detected in both cores PS2556 and PS1565, was assigned an age of ~92 ka, whilst Marine Tephra C in core PS1565 has a likely age of ~136 ka (Hillenbrand et al. 2008a).

In view of these chronological results, together with the observed down-core fluctuations in palaeoproductivity proxies, especially the Ba/Al ratios which are usually unaffected by dissolution, the biogenic intervals at the core surfaces are assigned to interglacial MIS 1, the first sub-surface biogenic intervals in cores PC723, PC726, PC727, PC734 and PS2556 to interglacial MIS 5, and the lower biogenic intervals in cores PC734 and PS2556 to interglacial MIS 7. Consequently, the terrigenous intervals in between are assigned to the glacial periods MIS 2-4, 6 and 8. These assignments are consistent with previous age assignments for cores from the study area (Pudsey & Camerlenghi 1998, Pudsey 2000, Sagnotti et al. 2001, Hillenbrand & Ehrmann 2002, Lucchi et al. 2002, Villa et al. 2003, Macrì et al. 2006, Venuti et al. 2011; Vautravers et al. 2013). We provide the age-depth fix points for our cores, including linear sedimentation rates, in Table 3. Importantly, these age models are predominantly based on a combination of $\delta^{18}O$-, tephro- and lithostratigraphy, whereas in previous studies only the age model for core PC466 from Drift 4, which was recovered in close proximity to site PC736, had some chronological constraints based on planktic $\delta^{18}O$ data (Vautravers et al. 2013). Our new age models document that sedimentation rates during glacial periods were consistently higher than during the preceding or subsequent interglacial periods (Table 3; Suppl. Fig. 3). Our age assignments are generally consistent with the RPI-based age models for some of the JR298 cores published in Channell et al. (2019) (Suppl. Fig. 3a-d), and we discuss the discrepancies below (see section 4.4.).

4. Interpretation and discussion

4.1. Sediment facies and inferred depositional processes

We distinguish six common **Facies A** to **F** and five rare **Facies G** to **K** (Table 4; Fig. 16; see Supplementary Text for full facies descriptions and references). Bioturbated **Facies A** and structureless **Facies B** occur at all sites and consist of (sandy) muds bearing biogenic material and scattered gravel grains interpreted as IRD. These hemipelagic sediments are assigned to MIS 1, 5 and 7. **Facies C, D, E** and **F**, assigned to glacial MIS 2-4, 6 and 8, lack biogenic components (Figs. 2-13) and bioturbation, probably as a consequence of (nearly) permanent sea-ice coverage during glacial periods. Laminated **Facies C** consists of muds alternating with silty-sandy laminae. Its sediments are interpreted as contourites derived from detritus transported down the continental slope by debris flows and slumps that were initiated by the advance of grounded ice masses across the shelf during glacial periods. At the base of the slope, the material went into suspension forming turbidity currents. Fine-grained particles in the upper parts of the suspension clouds were captured by the SW-ward flowing bottom current and deposited on the drifts. **Facies D** comprises very finely laminated muds interpreted as meltwater plume deposits. **Facies E** and **F** comprise stratified and laminated sediments, consisting of terrigenous muds either alternating with sandy-gravelly layers or bearing scattered gravel grains. These sediments are interpreted as contourites, with the coarse-grained layers being lag deposits resulting from current winnowing, and hemipelagic deposits, with the gravel grains and coarse layers resulting from IRD deposition. **Facies G** consists of occasionally normally graded, sandy to gravelly sediments with an erosional base interpreted as grain-flow deposits and proximal turbidites. **Facies H**, encountered only once in core PC728 (97-148 cmcd), comprises sand fining upward into sandy mud interpreted as a thick turbidite bed. **Facies I** cannot easily be distinguished from coring disturbance as it is characterised by deformed muds with silty-sandy layers or scattered gravel grains. These sediments occur frequently at site PC732 on Drift 5 (Suppl. Fig. 4) and are interpreted as slump and debris-flow deposits. **Facies J**, only found in a single interval of core PC734 (305-310 cmcd), comprises cross-laminated mud and silt interpreted as turbidite. Also **Facies K**, which comprises a structureless bed of silty-sandy volcanic glass particles, was only observed at site PC734 (1153-1157 cmcd; Fig. 7). Based on its stratigraphic position, the tephra bed was identified as Marine Tephra B previously reported from numerous West Antarctic sediment cores, including PS2556 and PS1565, and also identified as disseminated tephra or "cryptotephra" layer in core PC727 (Figs. 4, 9, 10).

4.2. Comparison of proxies for productivity

The most complete sets of palaeo-productivity data come from cores PC723, PC727 and PS1565 (Figs. 11-13). Biogenic barium is considered to be the most reliable palaeoproductivity proxy south of the Antarctic Polar Front as it is resistant to dissolution under oxic conditions (e.g. Nürnberg et al. 1997; Bonn et al. 1998; Pudsey & Howe 1998; Pudsey 2000; Hillenbrand & Cortese 2006; Jaccard et al. 2013). Oxic conditions at the investigated core sites towards the end of glacials and during interglacials are evident from high Mn/Al ratios and the occurrences of micro-Mn nodules (Figs. 2-13) as well as the presence of Mn-coated dropstones at the seafloor surfaces (Fig. 14; Suppl. Fig. 1). Lucchi & Rebesco (2007) concluded from the absence of bioturbation in glacial-age drift sediments (corresponding to our **Facies C** to **J**) and the presence of the mineral pyrrhotite in these sediments (Sagnotti et al. 2001), that oxygen-depleted bottom waters had bathed the Antarctic Peninsula continental rise during Late Quaternary glacial periods. However, a subsequent comprehensive study of the magnetic mineralogy of these sediments conducted by Venuti et al. (2011) documented an absence of pyrrhotite, and negligible/trace amounts of iron (Fe) sulphides. Recently, Channell et al. (2019) concluded for the JR298 cores that the authigenic mineral maghemite is present throughout the sediment column recovered by the PCs. Maghemite is formed at (and near) the seafloor surface by oxidation of (detrital) magnetite. In pelagic sediments maghemite is dissolved at the oxic-anoxic boundary, typically just a few decimetres below the surface. In the drift sediments, however, sub-surface dissolution of maghemite is significantly reduced, thereby varying between sites, and maghemite is present down to at least ~10 metres below the seafloor (Channel et al. 2019). This strongly suggests that our down-core Ba records do not result from dissolution that varies with core depth (Figs. 2-8, 10).

We consider that, theoretically, the interglacial Ba/Al maxima in our records could result from a higher supply of terrigenous barite. Like zircon, this detrital heavy mineral is typically enriched in the sand fraction, which is increased in the interglacial intervals of our cores (Figs. 2-10), reflecting the higher IRD content that characterises sediments of **Facies A** and **Facies B** (section 4.1., Suppl. Text; Figs. 14, 16; Suppl. Fig. 1). The Ba/Zr data match the Ba/Al data in all XRF scanned cores indicating that the Ba/Al maxima result from a high Ba_{bio} supply during interglacial periods (Figs. 2-8). The Ba/Al and Ba/Zr data available from discrete samples of cores PC723, PC727 and PS1565 corroborate these findings (Figs. 10-13).

The Br/Al data measured with the XRF scanner (Figs. 2-8) reveal a very good correlation with those measured on discrete samples (core PC727; Fig. 12), with maxima observed during interglacials. Br has been used as a palaeo-productivity proxy in marine sediments (e.g., Smith et al. 2017); Ziegler et al. (2008) demonstrated that high Br contents in sediments reflect higher marine organic carbon content rather than terrestrial organic material. This assertion is supported by the fact that the Br/Al data in the JR298 cores mirror the Ba/Al data (Figs. 2-8, 12).

Apart from a positive correlation in the near-surface sediments, we observe no clear relationship between TOC and Br/Al or TOC and Ba/Al, but at sites PC723, PC726, PC727, PC734 and PS1565 maxima in Ba/Al and/or Br/Al during MIS 5 and 7 coincide with very low TOC contents (Figs. 2-4, 7, 10-13). This suggests that organic matter below the core surface, and especially in glacial sediments (cf. PC728, Fig. 5), predominantly consists of old refractory carbon, whilst degradable, non-refractory carbon has been dissolved. In support of this, a close inspection of the sand fraction from Termination II sediments in core PS1565, which are characterized by a prominent TOC maximum preceding the MIS 5 maximum in Ba/Al ratios (and other productivity proxies), revealed the presence of a coal fragment. The coal was probably supplied as IRD, which is suggested by a sand maximum coinciding with the TOC maximum at

Termination II (Fig. 10). A similar TOC peak is also observed at Termination I in core PS1565. In addition, in core PC101 from Drift 1, the record with continuous down-core TOC data nearest to site PS1565 (Fig. 1), TOC maxima at both Termination I and Termination II also precede interglacial Ba/Al maxima (Pudsey, pers. comm. 2005). This hints at a significant source for fossil organic matter on the part of the Antarctic Peninsula margin adjacent to Drifts 1, 2 and 3.

The interglacial Ba/Al maxima coincide with maxima in biogenic opal, siliceous microfossils and Si/Al ratios (Figs. 10, 13; note: a minor opal maximum preceding Termination II in core PS1565 is caused by the presence of Marine Tephra C, Hillenbrand et al. 2008a), as has been reported previously from Antarctic Peninsula drift sediments (Pudsey & Camerlenghi 1998; Pudsey 2000). The opal maxima are caused by maxima in the abundances of diatoms (cf. Pudsey & Camerlenghi 1998; Pudsey 2000; Villa et al. 2003) and, for the deep cores, also of radiolarians (Fig. 10). The $CaCO_3$ maxima during interglacials originate predominantly from maxima in the abundances of planktic foraminifera, with only minor contributions from calcareous benthic foraminifera (Figs. 9, 13). In addition, rare occurrences of calcareous nannofossils have been reported from the intervals with the highest $CaCO_3$ contents (Villa et al. 2003).

In all of our cores spanning past interglacials, the Ba/Al maxima and (where measured) the opal maxima lead the $CaCO_3$ maxima, which is most evident in the cores with expanded MIS 5 intervals (Figs. 2-4, 7, 9-13). This distinctive sequence of maxima in various palaeoproductivity proxies has been previously reported from records recovered at water depths below ~2000 m on the East Antarctic continental margin between 15° W and 44° E (Grobe & Mackensen 1992; Bonn et al. 1998), our study area (Pudsey & Camerlenghi 1998; Pudsey 2000; Hillenbrand & Fütterer 2002; Villa et al. 2003) and the continental margin offshore from Prydz Bay (Wu et al. 2017). It has been attributed to a maximum in primary productivity, evident from the Ba/Al maximum, during peak interglacial conditions, which resulted in a maximum flux of fresh degradable, organic carbon to the seafloor. The subsequent remineralisation of this organic material resulted in a shallowing of the Calcite Compensation Depth (CCD), so that only siliceous microfossils were preserved (Grobe & Mackensen 1992; Bonn et al. 1998; Hillenbrand & Fütterer 2002). A decrease in productivity during the later, cooler, part of an interglacial, and perhaps even during the early part of a glacial, caused a deepening of the CCD that led to the preservation of calcareous microfossils and, thus, dilution of siliceous microfossils in the sediments. Accordingly, $CaCO_3$ maxima coincide with moderate Ba/Al ratios (e.g., Figs. 10, 13). A deepening of the CCD during throughout interglacials is also reflected in productivity proxies in core PS2556: increases in opal content during early MIS 7 and early MIS 5 are initially followed by maxima in calcareous foraminifera fragments, and these peaks are in turn followed by maxima in whole foraminiferal test concentrations (Fig. 9).

4.3. Diagenetic manganese enrichments and their implications for the geochemical record

A new finding in our study from the West Antarctic continental margin are distinct Mn-enrichments at the end of glacials and during interglacials. These enrichments are evident from high Mn/Al ratios and high abundances of sand-sized micro-Mn nodules within the cores (Figs. 2-13) and Mn-coated dropstones at the seafloor surface (Fig. 14; Suppl. Fig. 1). In cores PC723, PC726 and PC727, high Mn/Al ratios during MIS 5 and MIS 7 coincide with high Ba/Al ratios and $CaCO_3$ maxima that are also characterized by a complete absence of TOC, i.e., TOC =0 wt.% (Figs. 2-4). In addition, some subordinate Mn/Al spikes occur in late MIS 6 and late MIS 8 (and, to a lesser extent, late MIS 2) sediments at these core sites. At sites PC734, PS1565 and especially PS2556, high Mn/Al ratios and maxima in micro-Mn nodules, respectively, coincide with TOC minima that precede productivity peaks during MIS 1, 5 and 7 (evident from maxima in Ba/Al and Br/Al ratios and/or opal contents).

In previous work, Pudsey and Camerlenghi (1998) reported micro-Mn nodules from MIS 6 sediments in cores from Drift 7 and explained their occurrence with condensed deposition, whilst Pudsey (2000) described micro-Mn nodules associated with *Chondrites* burrows from MIS 1 sediments at sites PC107 (Drift 5), PC109, PC110 (both Drift 4A), PC111 (Drift 4) and PC113 (Drift 3). Furthermore, XRF data from discrete samples of core PC106 (Drift 6) presented by Pudsey (2000; see their Fig. 6b) showed an MnO-peak in sediments of late MIS 6 age. However, the Al-normalised Mn data of this core reveal two, more prominent and broad, maxima which bracket Marine Tephra B (Hillenbrand et al. 2008a) and comprise Termination I to MIS 1, respectively (Pudsey, pers. comm. 2005). As in our cores with XRF data from discrete samples (Figs. 11-13), the Mn/Al ratios at sites PC106 and PC111 reached their highest ratios around glacial terminations (Pudsey, pers. comm. 2005).

Manganese enrichments at the end of glacial periods and during interglacials were previously reported from other parts of the deep Southern Ocean, including the Antarctic continental margin (e.g., Mangini et al. 1990, 2001; Presti et al. 2011; Jaccard et al. 2016; Wagner & Hendy 2017; Wu et al. 2018; Jimenez-Espejo et al. 2019). Often these Mn-enrichments are explained by the presence of well-oxygenated Antarctic Bottom Water (AABW), whose production restarted or intensified at the end of glacial periods, when grounded ice began to retreat from the continental shelf and allowed the formation of AABW precursor water masses in sub-ice shelf cavities and coastal polynyas (Wu et al. 2018; Jimenez-Espejo et al. 2019). However, as in other ocean basins (e.g., Mangini et al. 1990, 2001; Kasten et al. 2004; Funk et al. 2004a, 2004b; Löwemark et al. 2014), it needs to be kept in mind that Mn in marine sediments is dissolved in pore-water under sub- and anoxic conditions and precipitated at the redoxcline, which forms the base of the oxic zone and usually is situated just a few decimetres (or even a few centimetres) below the seafloor surface. Under steady-state diagenetic conditions, the oxic-suboxic boundary, and thus also the horizon of solid-phase Mn-enrichment, will remain at a constant depth with respect to the sediment surface over time (Kasten et al. 2004). This implies that under continued sediment deposition Mn is constantly dissolved below and, after transport in pore-water towards the seafloor surface, precipitated at an upward migrating Mn-redox front (e.g., Kasten et al. 2004; Presti et al. 2011).

Relict redox fronts, such as those manifest in Mn-enrichments, can be preserved in down-core sediments when a front shifts rapidly upwards (e.g., Kasten et al. 2004), the depositional environment is characterised by low supply of labile organic carbon (De Lange et al. 1994), or the grain size of the precipitated Mn-concretions and coatings (such as the micro-manganese nodules in our cores) is larger than that of the host sediments (e.g., Mangini et al. 1990). Furthermore, the pore-water oxygen content at the depth of the relict front has to remain sufficiently high to prevent complete dissolution of the precipitated element oxide/hydroxide. In most instances, relict redox fronts indicate non-steady-state diagenetic conditions that could have been initiated by: (1) changes in organic carbon burial induced by variations in sedimentation rate, organic carbon supply to the seafloor and/or oxygen content of bottom water, (2) rapid sediment burial associated with deposition of turbidites, debris flows, slumps, etc., (3) variable upward diffusive flux of reduced components (such as methane) from deeper in the sediment column, and (4) changes in pore water/fluid flow from greater sediment depths or across the seawater-seabed interface (e.g., De Lange et al. 1994; Kasten et al. 2004). For the cyclic deposition of Mn-rich layers in the Arctic Ocean, a dramatically increased supply of dissolved Mn from the surrounding continental shelves via recycling from shelf sediments and landmasses derived from fluvial input has been identified as an additional, crucial factor (Löwemark et al. 2012, 2014). The processes summarised under (1) change particularly rapidly during the transition from a glacial to an interglacial period, so that relict redox fronts are frequently preserved across glacial terminations (e.g. Mangini et al. 2001; Funk et al. 2004a, 2004b; Kasten et al. 2004; Reitz et al. 2004; Jimenez-Espejo et al. 2019). However, the geochemical mobility of Mn in the sediments before an Mn-enriched layer is eventually “fixed” in the sedimentary record reduces the usefulness of such layers for core correlations, which is apparent from their sometimes variable stratigraphic position on an ocean-basin wide or even regional scale (e.g., Löwemark et al. 2014; Meinhardt et al. 2016; Jimenez-Espejo et al. 2019). This also should be taken into account when using Mn-enrichments in sediment cores for identifying and interpreting the exact timing of bottom water oxygenation during a glacial-interglacial cycle.

Well oxygenated bottom-water conditions at our core sites during the present interglacial MIS 1 are documented by the Mn-enrichments in the surface sediments (Figs. 2-13), and especially the Mn-coating of the dropstones on the seafloor (Fig. 14, Suppl. Fig. 1). The bottom water flooding the drifts is derived from oxygen-rich deep-water masses originating in the Weddell Sea (Camerlenghi et al. 1997; Giorgetti et al. 2003; Hillenbrand et al. 2008b; Hernández-Molina et al. 2017). Mn-enrichments are also observed across Terminations I, II and III and during MIS 5 and MIS 7 but their exact stratigraphic positions slightly vary between the core sites (Figs. 2-13). We consider that the onset of well oxygenated bottom-water conditions at our cores sites during glacial terminations, which may not necessarily be expressed in a change in bottom-current vigour (section 4.5.), caused a down-ward progression of the Mn-redox front (e.g., Kasten et al. 2004), thereby causing Mn-precipitation within sediments deposited at the end of glacial periods (Table 5).

The reliable palaeoproductivity proxies Ba/Al and Br/Al often document a sharp increase of biological productivity at the beginning of interglacials, with the productivity remaining high throughout peak interglacials. In case of MIS 1, this increase is also evident from the high TOC contents in the surface sediments (Figs. 2-13). The associated increased input and burial of degradable marine organic carbon should have shifted the redox fronts upwards toward the seafloor surface, but it has been shown that metastable element enrichments, such as the Mn-spikes in the late glacial sediments of our cores, can be preserved when this shift happens suddenly (De Lange et al. 1994; Kasten et al. 2004). Alternatively, no such upward shift might have happened because the increase in degradable carbon supply was insufficient to overcome the supply of well oxygenated bottom water (Table 5). The continued bathing of the drifts with this water mass during an interglacial would have caused very efficient remineralisation of the non-refractory, degradable organic matter at the seafloor and within the uppermost part of the seabed. This is evident from the TOC minima observed at the end of glacial MIS 6 and MIS 8, as well as during interglacial MIS 5 and MIS 7 in the cores spanning these time periods (Figs. 2-4, 7, 9-13). We note that most of our records with continuous down-core TOC data, especially PC728, PC734 and PS2556 (Figs. 5, 7, 9), also show this process to affect organic matter across Termination I, but the corresponding TOC minima are often less pronounced, probably because the remineralisation of marine organic carbon is still ongoing.

Notably, TOC minima of 0 wt.% or just above 0 wt.% from late MIS 8 into MIS 7 and from late MIS 6 into MIS 5, respectively, are observed in the westernmost cores PC723, PC726, PC727 and PS2556 as well as in core PC734, which was collected further east but also from relatively deep water (3000 m). These TOC minima reveal considerable “burn-down” of organic carbon, i.e. post-depositional oxidation of non-refractory organic matter (Figs. 2-4, 7, 11), implying that (i) sedimentation rates during the corresponding times did not exceed 1-2 cm/kyr (Jung et al. 1997; Mangini et al. 2001; Kasten et al. 2004), and (ii) the input of fossil, refractory organic material was at a minimum. We argue that both the burn-down of organic carbon at a glacial termination and during the early part of an interglacial caused by the availability of well oxygenated bottom water and the decrease in the input of degradable, marine organic matter during the latter part of an interglacial evident from the decreases in Ba/Al and Br/Al resulted in the oxic-suboxic boundary remaining stationary at a similar level in the seabed over thousands to tens of thousands of years, even under continued sediment deposition, leading to the recorded Mn-enrichments (cf. Kasten et al. 2004)

(Table 5). The apparently lower stratigraphic positions of the TOC minima and Mn-enrichments across Terminations II and III in core PS2556 when compared to cores PC723 and PC726, where the most prominent Mn-enrichments and coinciding TOC minima are observed in the MIS 5 and MIS 7 sediments, respectively, may hint at a deeper downward progression of the oxidation front or its longer persistence in the late glacial sediments at site PS2556 (Table 5), probably as a result of a lower sedimentation rate at this site (Figs. 2, 3, 9; Table 3). We highlight the joint occurrence of TOC minima and peaks in micro-Mn nodule abundance at site PS2556. Sedimentation rates <1-2 cm/kyr, required for major burn-down of organic carbon, are also a prerequisite for growth of Mn-nodules (e.g., Löwemark et al. 2012; Dutkiewicz et al. 2019). The ages of 130 ka for Marine Tephra B and 92 ka for Marine Tephra A (Hillenbrand et al. 2008a) yield a linear sedimentation rate of 0.9 cm/kyr for the corresponding MIS 5 sediment interval at site PS2556 (Fig. 9). Such low sedimentation rates, which may have persisted across glacial terminations at site PS2556, are consistent with organic carbon burn-down and Mn-nodule growth.

We assume that during glacial periods, when the bottom waters bathing the Antarctic margin and the deep Southern Ocean became less ventilated in response to drastically reduced AABW production (e.g., Jaccard et al. 2016; Wu et al. 2018; Jimenez-Espejo et al. 2019), a new Mn-redox front rapidly established itself below the seafloor surface. Afterwards, this new Mn-redox front migrated constantly upwards under continuous sediment deposition until the next glacial termination (Table 5).

In line with our observations and interpretations, interstitial water profiles from ODP sites 1095, 1096 and 1101 (Fig. 1) reveal maximum pore-water Mn-concentrations at sub-seafloor depths ranging from 12 m to 25 m (Barker et al. 1999). Above this depth, which was interpreted to correspond to the boundary between oxidising and reducing conditions (Barker et al. 1999), but more likely still lies within the suboxic zone (Kasten et al. 2004), solid-phase Mn-enrichments marking fossil Mn-redox fronts, such as those recorded in our cores, can readily be preserved.

4.4. Impact of non-steady-state diagenesis on the palaeomagnetic record

The evidence for non-steady-state diagenetic conditions affecting our cores, especially the sediments deposited around glacial terminations (section 4.3.), has implications for the palaeomagnetic records reconstructed from the sediments. Channell et al. (2019) already noted that the sediments of the JR298 cores appear unusually oxic and attributed this to low concentrations of degradable marine organic carbon. The unusually oxic conditions promoted authigenic growth of maghemite through oxidation of detrital magnetite at the seafloor surface. The maghemite formed in the oxic zone is usually dissolved in the reducing environment, typically a few decimetres below the seabed surface in pelagic sediments, but is preserved down-core at numerous depth intervals in the majority of the JR298 cores (Channell et al. 2019). This down-core prevalence of maghemite has also been reported from sediment records in the Arctic Ocean, and the chemical remnant magnetisation (CRM) acquired during the maghematisation process is thought to have altered palaeomagnetic recording in some of the cores (Channell & Xuan 2009; Xuan & Channell 2010; Xuan et al. 2012). The maghematisation process appears to have a debilitating effect on RPI reconstructions for JR298 cores PC723, PC727 and PC734 (Channell et al. 2019). Nevertheless, a "trial" RPI age model was proposed for core PC723, but was considered to be of poor quality. Investigations of sedimentary records from other ocean basins, including the equatorial Atlantic (e.g., Funk et al. 2004a, 2004b; Kasten et al. 2004; Reitz et al. 2004), the NW Pacific (e.g., Korff et al. 2016) and the Arctic Ocean (e.g., Wiers et al. 2019, 2020), have also shown that non-steady-state diagenesis can modify the palaeomagnetic intensity and directional records through post-depositional alteration and dissolution of magnetic minerals.

We propose that (partial) alteration of the palaeomagnetic records due to non-steady state diagenesis could have led to the (predominantly minor) discrepancies between the RPI-based age models for cores PC723, PC726, PC728, PC732 and PC736 (Channell et al. 2019) and the new age models reported here (Figs. 2, 3, 5, 6, 8; Table 3; Suppl. Fig. 3a-d). There are very limited chronological constraints from the foraminiferal $\delta^{18}O$ data and the palaeoproductivity proxies for Termination I and the MIS 5/4 boundary, and positions of Termination I in the cores are largely consistent with the RPI-based age models of Channell et al. (2019) (see Suppl. Fig. 3a, 3b, 3d). However, positions of Termination II in Bellingshausen Sea cores PC726 with a high quality RPI-based age model and PC723 with a poor quality RPI-based age model lie apparently deeper (by 124 and 137 cm, respectively) according to the RPI-based age models (Figs. 2, 3; Suppl. Fig. 3a). The foraminiferal $\delta^{18}O$ record of core PC726 shows a typical glacial-interglacial shift at the depth of our preferred MIS 6/5 boundary, and a similar shift is suggested by the down-core trend of the oldest $\delta^{18}O$ data available from MIS 5 sediments in core PC723. Moreover, core PS2556, in which Marine Tephra B was clearly identified (Fig. 9; Hillenbrand et al. 2008a), can be unambiguously correlated both with core PC726 using whole-core magnetic susceptibility (Suppl. Fig. 5) and with core PC723 using palaeoproductivity proxies (Figs. 2, 9). Marine Tephra B provides a clear stratigraphic marker for Termination II, even if bioturbation and/or initial settling of the tephra on sea ice or glacial ice before its final deposition on the seabed could have resulted in a slightly time-transgressive occurrence at different core sites (Hillenbrand et al. 2008a). In addition, the RPI-based age model for core PC726 suggests the presence of MIS 7 between 945 cmcd and the core base (Channell et al. 2019). However, both the sediment composition and the palaeoproductivity proxies in core PC726 do not support the presence of interglacial sediments in the corresponding core interval (Fig. 3). According to the correlation between cores PC726 and PS2556 (Suppl. Fig. 5), MIS 7 sediments were not recovered in core PC726 because they lie deeper in the seabed, below the maximum corer penetration depth at this site. Finally, the burn-down of organic carbon during MIS 5 and MIS 7 at sites PC723 and PC726 (Figs. 2, 3) requires sedimentation rates of <1-2 cm/kyr (Jung et al. 1997; section 4.4.). Such low sedimentation rates are in agreement with the age models proposed here but in contrast with the RPI-based age models, which yielded sedimentation rates in the order of 5-7 cm/kyr for the corresponding core intervals (Channel et al. 2019).

We attribute the age model discrepancies for the JR298 cores, i.e. mainly for the two cores from the Bellingshausen Sea, to the overprinting of the palaeomagnetic records by post-depositional diagenesis, which is clearly expressed in all three cores from the Bellingshausen Sea by major burn-down of organic carbon during interglacials MIS 5 and 7 and across Terminations II and III, respectively (Figs. 2, 3, 9). The potential impact of non-steady-state diagenesis on RPI records may also explain the discrepancies between the original lithostratigraphy- and biostratigraphy-based age models for sediment cores from Drift 7 developed by Pudsey & Camerlenghi (1998) and Lucchi et al. (2002) and the RPI-based age models published by Sagnotti et al. (2001) and Macrì et al. (2006). Possible diagenetic overprint of the RPI record should be taken into account, when the timing of sedimentary Mn-enrichments in cores with RPI-based age models are interpreted in terms of bottom-water ventilation processes (Jimenez-Espejo et al. 2019).

Additional detailed geochemical and palaeomagnetic investigations are required to characterize the precise diagenetic overprint of the magnetic record. In the JR298 cores from the Bellingshausen Sea the stratigraphic positions of Termination II according to the RPI-based age models seem to be too deep (by ~124 and 137 cm). In the Drift 7 cores analysed by Sagnotti et al. (2001) and Macrì et al. (2006) the MIS 6/5 boundaries reconstructed from their RPI age models either match, or are also deeper than, those proposed by Pudsey & Camerlenghi (1998) and Lucchi et al. (2002), when the same sedimentological criteria are used to determine the position of this boundary (Hillenbrand et al. 2008a). It is possible that the post-depositional magnetisation lock-in process and non-steady-state diagenesis have led to delayed and (partially) altered recording of the palaeomagnetic signal. The Fe-redox front usually lies just below the Mn-redox front (e.g., Tarduno & Wilkison 1996, Kasten et al. 2004; Reitz et al. 2004; Roberts 2015). If, for example, at site PC726 the onset of highly-oxygenated bottom water flow at Termination II led to a down-ward oxygen diffusion and migration of the redox fronts, which may be indicated by the Mn-enrichments in the late MIS 6 sediments (Fig. 3), magnetic grains newly formed at the top of the Fe-redox front within the late MIS 6 sediments could carry a delayed chemical remanence similar to that reported in sediments from the equatorial Pacific Ocean by Tarduno & Wilkison (1996). A sudden subsequent upward shift of redox fronts in response to the interglacial productivity increase (De Lange et al. 1994; Kasten et al. 2004) or the fact, that even when the biological productivity reached its maximum, the availability of labile organic carbon was still too low to counteract the oxygen supply through the bottom water, could have allowed the preservation of the metastable element enrichments in the records.

Finally, we emphasize that below the oxic zone (i.e., below ~12-25 m sub-bottom depth in our study area; Barker et al. 1999) the effect of non-steady-state diagenesis on the palaeomagnetic record should be negligible. This is confirmed by the good match between the Mid-Pleistocene (~1.6 to 0.7 Ma) RPI record from ODP Site 1101 (Fig. 1) and global palaeointensity stacks (see Guyodo et al. 2001; Channell et al. 2019). At larger seafloor depths, however, Fe-oxide dissolution in the anoxic zone may overprint the palaeomagnetic signal, which is evident from the occurrence of magnetic susceptibility minimum zones in the Late Miocene to Late Pliocene sedimentary sequence from below ~80 m core depth at ODP Site 1095 (Hepp et al. 2009).

4.5. Variability of bottom current flow

We analysed $\overline{SS}$ together with SS% on cores PC727 from 2681 m water depth on Drift 7 and PC734 from 3000 m water depth on Drift 5 with the intention of reconstructing changes in bottom-current speed (Figs. 4, 7). Whilst the correlation coefficient R between $\overline{SS}$ and SS% of samples from both cores exceeds 0.5 (section 3.2.), we do not have SS% data for all our $\overline{SS}$ data (Suppl. Fig. 2). Consequently, we cannot determine the running down-core correlation R_{run} and thereby rule out poor sorting for many of our samples. This, however, is a prerequisite, if the $\overline{SS}$ data of an IRD-influenced sedimentary record are to be interpreted as a reliable proxy for bottom-current speed (McCave & Andrews 2019). Nevertheless, our $\overline{SS}$ data, which predominantly vary in a relatively narrow range between 16 and 22 µm in both cores seem to indicate only minor glacial-interglacial changes in bottom-current velocity (Figs. 4, 7), perhaps with a slightly higher speed during interglacials and at the end of the penultimate glacial period recorded at site PC727. This result is largely in agreement with detailed grain-size data published by Pudsey & Camerlenghi (1998) from other Drift 7 cores, although these authors did not remove biosiliceous components from their samples before they analysed grain size. In general, our findings are also in line with the results of measurements on core PC466 from the crest of Drift 4 (Vautravers et al. 2013). In core PC466 $\overline{SS}$ fluctuates between 15 and 27 µm (average 18 µm). According to the RPI-based age model for this core, higher $\overline{SS}$ is recorded at the very end of MIS 5, which spans the lowermost part of the core (NB: only two samples from MIS 1 were analysed, which may not be representative). Also, Vautravers et al. (2013) used a Coulter Counter MS3 and thus did not determine SS%. However, the authors concluded, based on an anti-correlation between $\overline{SS}$ and coarse fraction content (>63 µm), a significant impact of IRD deposition on the $\overline{SS}$ record at site PC466.

Conversion of the $\overline{SS}$ data from the two JR298 cores, which were analysed with a Coulter Counter MS3, into the corresponding SediGraph grain size using the procedure proposed by McCave et al. (2017) provides full ranges of 14-19 µm for site PC727 and 13-24 µm for site PC734. According to the relation between current-meter mooring data and $\overline{SS}$ of surface sediments from various locations in the Atlantic Ocean and Atlantic sector of the Southern Ocean obtained by McCave et al. (2017), bottom-current speed varied by 6.8 cm/s at site PC727 and 14.9 cm/s at site PC734. Translating the $\overline{SS}$ values into current speeds using a regional relation found by these authors for the Weddell and Scotia seas, yields a bottom-current speed range from 2 to 20 cm/s (Suppl. Fig. 6), with a long-term average speed of 7.0 cm/s at site PC727 and 6.8 cm/s at site PC734. Such speeds are in agreement with the range of modern bottom-current velocities measured around Drift 7 (Suppl. Fig. 6; Camerlenghi et al. 1997; Giorgetti et al. 2003). Bottom-current speeds exceeding ~13 cm/s are capable of winnowing some fine silt and clay particles, while erosional winnowing requires current speeds ≥20 cm/s (McCave & Hall 2006).

Bottom-current advection of clay-sized particles is evident from clay mineral assemblages in surface sediments. These assemblages show SW-ward transport of smectite-enriched detritus supplied from the South Shetland Islands along the continental rise offshore from the northern Antarctic Peninsula, and of chlorite- and illite-enriched detritus supplied from the central spine of the Antarctic Peninsula and Alexander Island along the rise offshore from the southern Antarctic Peninsula and further into the Bellingshausen Sea (Hillenbrand et al. 2003, 2005, 2009; Hillenbrand & Ehrmann 2002, 2005; Park et al. 2019). In interglacial sediments the far-travelled, distal clay mineral component is enriched with respect to the proximal component supplied from the adjacent shelf (Pudsey 2000; Hillenbrand & Ehrmann 2002; Lucchi et al. 2002), which is consistent with the clay mineral data presented here (Figs. 4, 7, 10, 15; Table 5). Based on the indications of only weak glacial-interglacial changes in bottom-current speed on the drift crests provided by detailed grain-size data (Figs. 4, 7; cf. Pudsey & Camerlenghi 1998), we attribute the chlorite increase in glacial-age sediments of our cores (Figs. 4, 7, 10, 15) and other cores from the study area to a "dilution" of bottom-current transported smectite-enriched detritus (cf. Pudsey 2000; Lucchi et al. 2002; Hillenbrand & Ehrmann, 2005). This dilution was caused by an enhanced supply of glacigenic, chlorite-enriched debris from the adjacent shelf regions in response to grounded ice sheet advance during glacial periods (Ó Cofaigh et al. 2014). This hypothesis is corroborated by the sedimentation rates for our cores, which are consistently higher during a glacial period than during the preceding and subsequent interglacial period (Table 3).

4.6. Deposition of iceberg-rafted debris and the role of bioturbation

As it is evident from both X-radiograph observations and the down-core gravel and sand records (Figs. 2-10), IRD in the sediments is mainly enriched during interglacials and at the end of glacials. In the JR298 cores, some of the sand content increase in interglacial sediments with high $CaCO_3$ content can be explained by increased planktic foraminifera abundance, because no carbonate was removed from the samples before grain-size analysis (section 2.). However, elevated sand contents at the end of glacials and during interglacials are also recorded in cores PS1565 and PS2556 (Figs. 9, 10), from which samples were decalcified before sieving. In core PS1565 sand-sized radiolarians probably contribute somewhat to the elevated sand content in the MIS 1 and early MIS 5 sediments (Fig. 13), but we can rule this out for core PS2556 because the radiolarian content in its sand fraction is <1.2% throughout (Braun 1997). In all cores, the sand content, and to a lesser extent the gravel content, exhibits occasionally discrete enrichments in glacial-age intervals (Figs. 2-10), a characteristic caused by the deposition of turbidites/slumps and bottom-current winnowing (see **Facies E** to **Facies I**, section 4.1. and Suppl. Text). The pattern of glacial-interglacial IRD deposition in our cores is consistent with previous IRD studies on the Antarctic Peninsula drifts (Pudsey & Camerlenghi 1998; Ó Cofaigh et al. 2001; Pudsey 2002; Cowan et al. 2008; Vautravers et al. 2013). High IRD supply was caused by the break-up of grounded ice masses on the adjacent West Antarctic shelf at the end of glacial periods (Hillenbrand et al. 2010; Ó Cofaigh et al. 2014) and seasonal open-water conditions during interglacial periods that allowed free drift of icebergs (Pudsey & Camerlenghi 1998; Pudsey 2000; Ó Cofaigh et al. 2001).

A surprising result of our investigation is the enrichment of gravel-sized IRD at the seafloor surfaces of the JR298 sites. With the exception of core PC727, these gravel maxima appear unprecedented when compared to the total time periods spanned by the cores, even if only those PCs which recovered sediments from previous interglacials are considered (Figs. 2-8; 14; Suppl. Fig. 1). Continuous down-core gravel clast counts by Ó Cofaigh et al. (2001) and detailed grain-size analyses by Pudsey & Camerlenghi (1998) on Antarctic Peninsula drift cores that also retrieved sediments deposited during interglacial MIS 5 and MIS 7, did not reveal absolute maxima of coarse grains at the core-tops. However, it is unclear whether the cores analysed by these authors retrieved (undisturbed) seafloor surface sediments. On the other hand, we cannot rule out a sampling bias for our JR298 cores because our down-core samples may have missed by chance gravel-rich horizons in glacial intervals (within **Facies E, F, G**) and interglacial intervals (within **Facies A** and **Facies B**) that are often only visible in the X-radiographs (Fig. 16; cf. Ó Cofaigh et al. 2001). Continuous down-core gravel counts were carried out on X-radiographs from cores PS1565 and PS2556, which do not show an unprecedented maximum at the core top either (Figs. 9, 10). However, GC PS2556-2 did not recover the modern seafloor surface (Braun 1997), and no X-radiographs are available for MUC PS2556-1. Equally, it is unclear for GC PS1565-2, whether it recovered the modern seabed surface.

Nevertheless, the gravel-sized IRD maximum detected at the surfaces of nearly all JR298 cores is such an outstanding feature that it requires further investigation. In the following discussion, we consider four different explanations. First, the IRD maximum could result from unprecedented ice loss and associated iceberg calving from the Pacific sector of the APIS and the Bellingshausen Sea sector of the WAIS. Although major ice loss has affected both sectors over recent decades (e.g., Wouters et al. 2015; Cook et al. 2016; Christie et al. 2016; Rignot et al. 2019), we would not expect IRD supply to our sites to be higher than across glacial terminations or during MIS 5e, when marine-based parts of the WAIS are assumed to have collapsed and the APIS is assumed to have been smaller (e.g., DeConto & Pollard 2016).

Second, enhanced IRD deposition at present could be caused by warming of Southern Ocean surface waters that both increased iceberg melting and reduced seasonal sea-ice cover, allowing icebergs to drift more freely. Despite overall Southern Ocean warming recorded over recent decades, near-surface water temperatures south of the Antarctic Polar Front have hardly warmed or have actually slightly cooled (Armour et al. 2016; Swart et al. 2018), whereas sea-ice cover in our study area has decreased (e.g., Parkinson 2019). Again, however, we would not expect that current IRD deposition is higher than during MIS 5e, when surface water temperatures south of the Antarctic Polar Front were higher than today and seasonal sea-cover was reduced (e.g., Chadwick et al. 2020).

Third, the bottom current affecting the JR298 core sites could be stronger today than in the past and, thus have enriched coarse-grained IRD by winnowing. Support for this scenario may come from the $\overline{SS}$ data in core PC734/GBC735, which reveal an absolute maximum at the seafloor surface (Fig. 7). However, we cannot rule out that this $\overline{SS}$ maximum is actually related to the high IRD content in the seafloor surface sediments itself (sections 3.2. and 4.5.; Suppl. Fig. 2). The only other available $\overline{SS}$ data from site PC727/GBC730 seem to be less impacted by IRD deposition (sections 3.2. and 4.5.; Suppl. Fig. 2), but at this site neither $\overline{SS}$ nor the gravel and sand content display absolute maxima at the surface (Fig. 4). Nevertheless, if we ignore the potential IRD caveats in our $\overline{SS}$ data (section 4.5.), the calculated maximum bottom-current speed of 20 cm/s is reached at the surface of site PC734/GBC735 (Suppl. Fig. 6). This velocity matches the maximum current speed measured in the 1990s (Giorgetti et al. 2003) and would allow some winnowing of clay and fine silt particles (McCave & Hall 2006). Strong support for the hypothesis of bottom-current winnowing comes from the presence of Mn-coated dropstones at the seabed surfaces of all JR298 sites (Fig. 14; Suppl. Fig. 1) because the growth of Mn-coatings requires sedimentation rates ≤1-2 cm/kyr (e.g., Löwemark et al. 2012; Dutkiewicz et al. 2019). However, we do not favour this explanation because the available AMS ^{14}C dates from seafloor surface sediments provided uncorrected average ages of 1050 ^{14}C yrs BP at site GBC735/PC734 and 1338 ^{14}C yrs BP at site GBC729/PC728 (Table 2). These ages, which also include dates on planktic foraminifera and thus cannot be explained with recent colonisation of an old seafloor substrate by benthic fauna, lie within the range of the Southern Ocean MRE and thus confirm recent deposition at both core sites (section 3.4.). Independently, a more recent age for the seafloor surface sediments at the studied sites is also consistent with the high TOC contents (Figs. 2-13). According to the coinciding high Ba/Al and Br/Al ratios, most of this TOC should consist of degradable, non-refractory organic material, which would have been remineralised at sedimentation rates ≤1-2 cm/kyr (Jung et al. 1997; Kasten et al. 2004). The AMS ^{14}C ages from the surface sediments at site GBC729/PC728 are slightly older than at site GBC735/PC734 (section 3.4.; Table 2), suggesting that some winnowing influenced the former site. This conclusion is corroborated by the seafloor surface photos from the two locations as they display a higher concentration of coarse-grained debris at site GBC729/PC728 than at site GBC735/PC734 (Fig. 14).

The apparent conflict between the recent AMS ^{14}C dates for the seafloor surface sediments and the presence of Mn-coated dropstones leads us to a fourth explanation, i.e. the “biological upward pumping” of IRD. This process has been proposed by McCave (1988), who investigated a large number of box cores collected outside of the modern zone of IRD deposition on the Nova Scotia continental margin. The author observed terrigenous clasts >1-2 mm near the surface of strongly bioturbated muds in several cores, but only at sites, where the mud was underlain by a diamicton (below ~40 cm. sub-bottom depth). McCave (1988) attributed this finding to constant upward pumping of terrigenous particles >1-2 mm from the diamicton source layer during the deposition of the overlying mud, facilitated by extensive burrowing of the sediments by detritus-feeding, infaunal organisms that were unable to ingest particles larger than sand. The author furthermore suggested that in other ocean basins biological pumping maintains Mn-nodules at the seafloor surface over (tens of) thousands of years. Piper & Fowler (1980) and Sanderson (1985) had previously highlighted the role of bioturbation in maintaining Mn-nodules at seabed surfaces.

Biological pumping also would explain the enrichment of Mn-coated, gravel-sized IRD at the surfaces of the JR298 cores (Figs. 2-8, 14; Suppl. Fig. 1). As in the study of McCave (1988) the sediments near the seafloor consist of extensively bioturbated to homogenised muds (**Facies A** and **Facies B**; section 4.1.) and were deposited at sedimentation rates ranging from 1-10 cm/kyr (Table 3). According to the gravel percentage data, IRD contents within or at the base of the bioturbated MIS 1 sediments of the JR298 cores are very low (Figs. 2-8), but both gravel clasts observed in the X-radiographs and sand contents reveal scattered IRD in these muds (Fig. 16). The lack of a potential distinct gravel source layer implies that the IRD has been maintained at the seabed surface since its deposition. Gravel-grain counts on X-radiographs of cores PS1565 and PS2556 (Figs. 9, 10) and other drift cores (Ó Cofaigh et al. 2001) reveal high concentrations of gravel-sized IRD in sediments deposited from the end of MIS 2 throughout MIS 1. Such IRD-enriched sediments may provide a feasible gravel source. We speculate that the process of biological pumping may have been more active at the JR298 sites than at sites PS1565 and PS2556 and at the locations of cores analysed by Ó Cofaigh et al. (2001) because most of the JR298 cores were recovered from water depths ≤3000 m. Sotaert et al. (1996) and Middelburg et al. (1997) showed that the biological mixing coefficient, i.e. the degree of burrowing, is ≤1 below 3000 m, but increases exponentially with decreasing water depth. In the JR298 cores, IRD enrichments resembling those observed at the modern surface do not occur in the sediments deposited during MIS 5 or MIS 7; but with benthic activity decreasing towards the end of a (peak) interglacial in response to decreasing biological productivity, we would expect any pre-existing sharp IRD peaks to be "smeared out". Biological pumping may even be able to move (micro-)fossils and fossil fragments >150 µm to the seafloor surface or maintain them there over a considerable time period (McCave 1988; Thomson et al. 1995). Whilst relative maxima in sand content at the surfaces of the JR298 sites may lend some support to the hypothesis that grains <1 mm may also be affected by biological pumping, the good match between the modern Southern Ocean MRE and our AMS ^{14}C ages (section 3.4.; Table 2), which were obtained from various benthic and planktic (micro-)fossils of different sizes, do not support the hypothesis of (micro-)fossils having been "pumped upwards". In summary, however, our results indicate potential stratigraphic displacement of gravel-sized IRD over at least 10s of centimetres (cf. McCave 1988). This finding highlights that at core sites from water depths ≤3000 m and with low to medium sedimentation rates (~1-10 cm/kyr) caution is required in interpreting IRD records that are based on contents and/or abundances of relatively large grains (>1 mm) only.

5. Summary and conclusions

New sediment records from the West Antarctic continental margin in the eastern Pacific sector of the Southern Ocean targeted predominantly drift crests at ≤3000 m water depth. Most cores retrieved sediment intervals containing calcareous foraminifera (almost exclusively planktic foraminifera), allowing AMS ^{14}C dating of surface sediments and obtaining down-core $\delta^{18}O$ data. In combination with tephrochronological constraints and lithostratigraphical down-core changes in response to glacial-interglacial cycles, the $\delta^{18}O$ data were used to establish age models for the cores. Accordingly, Late Quaternary sedimentation rates varied from ≤1 to ~20 cm/kyr and were higher during glacials.

Facies analysis confirmed previous interpretations in showing that bottom-current activity with glacigenic detritus being supplied from the adjacent shelf by down-slope transport processes exerted the main control on sediment deposition on the drifts. $\overline{SS}$ data from the drift crests suggest only minor changes in bottom-current speeds over glacial- interglacial cycles and that the current velocity changed over these timescales within the same range as over recent annual timescales. Sediment facies furthermore revealed that gravitational down-slope transport can occasionally affect deposition at shallow drift sites.

A comparison of palaeoproductivity proxies emphasizes that biogenic barium and bromine are the most reliable proxies for the supply and deposition of marine organic matter. In contrast, TOC content is affected by considerable post-depositional remineralisation and input of fossil, refractory organic matter, whilst $CaCO_3$ content can occasionally be overprinted by dissolution. Biogenic opal content can be influenced by dilution with calcareous microfossils. Enrichments of solid-phase manganese at the end of glacials and during interglacials provide not only evidence for the onset of well oxygenated bottom-water conditions at glacial terminations, but also for non-steady-state diagenetic processes. “Pinning” of the redox front below the seafloor surface over prolonged time periods and possible vertical shifts of the redox front within the sediment column in response to changes in bottom-water oxygenation, biological productivity and sedimentation rates led to major burn-down of organic carbon across glacial terminations and during interglacials. This type of diagenesis probably also altered the magnetic mineralogy of the sediments and led to their delayed remanence acquisition, which may explain the differences between our new age models for the cores and previously published, RPI-based age models. Pore-water and RPI data from ODP Leg 178 cores, however, suggest that non-steady-state diagenesis mainly affects the oxic part of the sediment column. At ODP sites 1096 and 1101 from the crests of Drift 7 and Drift 4 (Fig. 1) the base of the oxic zone was observed at sub-bottom depths of ~12-25 m, respectively (Barker et al. 1999). Given the sedimentation rates for the JR298 cores recovered from drift crests (Table 3), we can assume that at these locations sediments deposited between ~70 and 770 ka may have been affected by non-steady-state diagenesis.

Nearly all seafloor surface sediments recovered from ≤3000 m water depth on the drifts are characterised by unprecedented IRD maxima and Mn-coating of large dropstones. The required Mn-growth rates are in conflict with modern AMS ^{14}C ages on calcareous (micro-)fossils from the surface sediments. The most likely explanation for this discrepancy is upward pumping of gravel grains and larger clasts through extensive bioturbation, which ensured the maintenance of IRD at the seabed surface throughout interglacial periods. The resulting stratigraphic displacement needs to be taken into account in interpretations of IRD-records.

6. Acknowledgements

We thank the Captain, officers, crew, and shipboard scientists of RRS *James Clark Ross* cruise JR298, especially J. Channell. Furthermore, we acknowledge S. MacLachlan and her team from the British Ocean Sediment Core Research Facility (BOSCORF Southampton) and V. O'Mahoney and her colleagues from The Queen's Veterinary School Hospital (University of Cambridge) for assistance with physical properties measurements and X-raying, respectively. We are grateful to J. Rolfe, (University of Cambridge), S. Haessner (University of Leipzig) and M. Seebeck and R. Fröhlking (AWI) for support with laboratory analyses. N. Odling (Grant Institute, School of GeoSciences, University of Edinburgh) is acknowledged for conducting the XRF analyses on the discrete sediment samples. This study forms part of the British Antarctic Survey's *Polar Science for Planet Earth Programme* and was made possible by NERC UK-IODP grants NE/J006513/1 and NE/J006548/1. This study has been carried out in collaboration with "The Drifters" Research Group at Royal Holloway University of London (RHUL) and is related to the TASDRACC Project CTM2017-89711-C2-01-P & CTM2017-89711-C2-02-P.

7. References

Armour, K.C., Marshall, J., Scott, J.R., Donohoe, A., Newsom, E.R., 2016. Southern Ocean warming delayed by circumpolar upwelling and equatorward transport. Nat. Geosci. 9, 549-554.

Arndt, J.E., 15 others, 2013. The International Bathymetric Chart of the Southern Ocean (IBCSO) Version 1.0—A new bathymetric compilation covering circum-Antarctic waters. Geophys. Res. Lett. 40, 3111-3117.

Barker, P.F., Camerlenghi, A., Acton, G.D., et al., 1999. Proceedings of the Ocean Drilling Program, Initial Reports 178 (CD-ROM). Available from: Ocean Drilling Program, Texas A&M University, College Station, TX 77845-9547, U.S.A.

Barker, P.F., Camerlenghi, A., Acton G.D., Ramsay, A.T.S. et al., 2002. Proceedings of the Ocean Drilling Program, Scientific Results 178 (CD-ROM). Available from: Ocean Drilling Program, Texas A&M University, College Station, TX 77845-9547, U.S.A.

Bart, P.J., Hillenbrand, C.-D., Ehrmann, W., Iwai, M., Winter, D., Warny, S.A., 2007. Are Antarctic Peninsula Ice Sheet grounding events manifest in sedimentary cycles on the adjacent continental rise? Mar. Geol. 236, 1-13.

Berkman, P.A., Forman, S.L., 1996. Pre-bomb radiocarbon and the reservoir correction for calcareous marine species in the Southern Ocean. Geophys. Res. Lett. 23, 363-366.

Berkman, P.A., 16 others, 1998. Circum-Antarctic coastal environmental shifts during the Late Quaternary reflected by emerged marine deposits. Antarct. Sci. 10, 345-362.

Bonn, W.J., Gingele, F.X., Grobe, H., Mackensen, A., Fütterer, D.K., 1998. Palaeoproductivity at the Antarctic continental margin: opal and barium records for the last 400 ka. Palaeogeogr. Palaeoclimatol. Palaeoecol. 139, 195-211.

Braun, B., 1997. Rekonstruktion glaziomariner Sedimentationsprozesse am Kontinentalrand des westlichen Bellingshausenmeeres. Diploma Thesis, Geological Institute of the University of Würzburg, Germany, 83 pp.

Camerlenghi, A., Crise, A., Pudsey, C.J., Accerboni, E., Laterza, R., Rebesco, M., 1997. Ten-month observation of the bottom current regime across a sediment drift of the Pacific margin of the Antarctic Peninsula. Antarct. Sci. 9, 426-433.

Chadwick, M., Allen, C.S., Sime, L.C. & Hillenbrand, C.-D., 2020. Analysing the timing of peak warming and minimum winter sea-ice extent in the Southern Ocean during MIS 5e. Quat. Sci. Rev. 229, 106134.

Channell, J.E.T., Xuan, C., 2009. Self-reversal and apparent magnetic excursions in Arctic sediments. Earth Planet. Sci. Lett. 284, 124-131.

Channell, J.E.T., Larter, R.D., Hillenbrand, C.-D., Vautravers, M., Hodell, D.A., Hernández-Molina, F.J., Gohl, K., Rebesco, M., 2008. IODP Proposal 732-Full2: Sediment drifts off the Antarctic Peninsula and West Antarctica. https://docs.iodp.org/Proposal_Cover_Sheets/732-Full2_Channell_cover.pdf.

Channell, J.E.T., Xuan, C., Crowhurst, S.J., Hodell, D.A., Larter, R.D., 2019. Relative paleointensity (RPI) and age control in Quaternary sediment drifts off the Antarctic Peninsula. Quat. Sci. Rev. 211, 17-33.

Christie, F.D.W., Bingham, R.G., Gourmelen, N., Tett, S.F.B., Muto, A., 2016. Four decade record of pervasive grounding line retreat along the Bellingshausen margin of West Antarctica. Geophys. Res. Lett. 43, 5741-5749.

Cook, A.J., Holland, P.R., Meredith, M.P., Murray, T., Luckman, A., Vaughan, D.G., 2016. Ocean forcing of glacier retreat in the western Antarctic Peninsula. Science 353, 283-286.

Cortese, G., Gersonde, R., Hillenbrand, C.-D., Kuhn, G., 2004. Opal sedimentation shifts in the World Ocean over last 15 Myr. Earth Planet. Sci. Lett. 224, 509-527.

Cowan, E.A., Hillenbrand, C.-D., Hassler, L.E., Ake, M.T., 2008. Coarse-grained terrigenous sediment deposition on continental rise drifts: a record of Plio-Pleistocene glaciation on the Antarctic Peninsula. Palaeogeogr. Palaeoclimatol. Palaeoecol. 265, 275-291.

Cunningham, A.P., Larter, R.D., Barker, P.F., Gohl, K., Nitsche, F.-O., 2002. Tectonic evolution of the Pacific margin of Antarctica: 2. Structure of late Cretaceous-early Tertiary plate boundaries in the Bellingshausen Sea from seismic reflection and gravity data. Journal of Geophysical Research 107 (B12), 2346. doi:10.1029/2002JB001897.

Davies, S.M., 2015. Cryptotephras: The revolution in correlation and precision dating. J. Quat. Sci. 30, 114-130.

De Lange, G.J., Van Os, B., Pruysers, P.A., Middelburg, J.J., Castradori, D., Van Santvoort, P., Mueller, P.J., Eggenkamp, H., Prahl, F.G., 1994. Possible early diagenetic alteration of palaeo proxies. In: Zahn, R., Pedersen, T.F., Kaminski M.A., Labeyrie, L. (Eds.), Carbon Cycling in the Glacial Ocean: Constraints on the Ocean's Role in Global Change. NATO ASI Series 17, Kluwer Academic Publishers, Dordrecht, pp. 225-258.

DeConto, R.M., Pollard, D., 2016. Contribution of Antarctica to past and future sea-level rise. Nature 531, 591-597.

Di Roberto, A., Colizza, E., Del Carlo, P., Petrelli, M., Finocchiaro, F., Kuhn, G., 2019. First marine cryptotephra in Antarctica found in sediments of the western Ross Sea correlates with englacial tephras and climate records. Nat. Sci. Repts. 9, 10628, https://doi.org/10.1038/s41598-019-47188-3.

Dowdeswell, J.A., Ó Cofaigh, C., Pudsey, C.J., 2004. Continental slope morphology and sedimentary processes at the mouth of an Antarctic palaeo-ice stream. Mar. Geol. 204, 203-214.

Dowdeswell, J.A., Ó Cofaigh, C., Noormets, R., Larter, R.D., Hillenbrand, C.-D., Benetti, S., Evans, J., Pudsey, C.J., 2008. A major trough-mouth fan on the continental margin of the Bellingshausen Sea, West Antarctica: The Belgica Fan. Mar. Geol. 252, 129-140.

Dutkiewicz, A., Judge, A., Müller, R.D., 2019. Environmental predictors of deep-sea polymetallic nodule occurrence in the global ocean. Geology 48, 293-297.

Ehrmann, W., Hillenbrand, C.-D., Smith, J.A., Graham, A.G.C., Kuhn, G., Larter, R.D., 2011. Provenance changes between recent and glacial-time sediments in the Amundsen Sea embayment, West Antarctica: clay mineral assemblage evidence. Antarct. Sci. 23, 471-486.

Elderfield, H., Ferretti, P., Greaves, M., Crowhurst, S.J., McCave, I.N., Hodell, D.A., Piotrowski, A.M., 2012. Evolution of ocean temperature and ice volume through the Mid-Pleistocene Climate Transition. Science 337, 704-709.

Escutia, C., Bárcena, M.A., Lucchi, R.G., Romero, O., Ballegeer, A.M., Gonzalez, J.J., Harwood, D.M., 2009. Circum-Antarctic warming events between 4 and 3.5 Ma recorded in marine sediments from the Prydz Bay (ODP Leg 188) and the Antarctic Peninsula (ODP Leg 178) margins. Global Planet. Change 69, 170-184.

Funk, J.A., von Dobeneck, T., Reitz, A., 2004a. Integrated rock magnetic and geochemical quantification of redoxomorphic iron mineral diagenesis in Late Quaternary sediments from the equatorial Atlantic. In: Wefer, G., Mulitza, S., Ratmeyer, V. (Eds.), The South Atlantic in the Late Quaternary: Reconstruction of Material Budgets and Current Systems. Springer, Berlin, Heidelberg, New York, pp. 237-260.

Funk, J.A., von Dobeneck, T., Wagner, T., Kasten, S., 2004b. Late Quaternary sedimentation and early diagenesis in the equatorial Atlantic Ocean: patterns, trends and processes deduced from rock magnetic and geochemical records. In: Wefer, G., Mulitza, S., Ratmeyer, V. (Eds.), The South Atlantic in the Late Quaternary. Reconstruction of Material Budgets and Current Systems. Springer, Berlin, Heidelberg, New York, pp. 461-497.

Gales, J., Hillenbrand, C.-D., Larter, R., Laberg, J.S., Melles, M., Benetti, S., Passchier, S., 2018. Processes influencing differences in Arctic and Antarctic trough mouth fan sedimentology. In Le Heron, D.P., Hogan, K.A., Phillips, E.R., Huuse, M., Busfield, M.E., Graham, A.G.C. (Eds,), Glaciated Margins: The Sedimentary and Geophysical Archive, Geol. Soc. London Special Publ. 475, pp. 203-221.

Gebbie, G., Peterson, C.D., Lisiecki, L.E., Spero, H.J., 2015. Global-mean marine $\delta^{13}C$ and its uncertainty in a glacial state estimate. Quat. Sci. Rev. 125, 144-159.

Giorgetti, G., Crise, A., Laterza, R., Perini, L., Rebesco, M., Camerlenghi, A., 2003. Water masses and bottom boundary layer dynamics above a sediment drift of the Antarctic Peninsula Pacific Margin. Antarct. Sci. 15, 537-546.

Graham, A.G.C., Nitsche, F.O., Larter, R.D., 2011. An improved bathymetry compilation for the Bellingshausen Sea, Antarctica, to inform ice-sheet and ocean models. Cryosphere 5, 95-106. http://dx.doi.org/10.5194/tc-5-95-2011.

Grobe, H., 1987. A simple method for the determination of ice-rafted debris in sediment cores. Polarforschung 57, 123-126.

Grobe, H., Mackensen, A., 1992. Late Quaternary climatic cycles as recorded in sediments from the Antarctic continental margin. In: Kennett, J.P., Warnke, D.A. (Eds.), The Antarctic Paleoenvironment: a Perspective on Global Change, Antarct. Res. Ser. 56. American Geophysical Union, Washington D.C., pp. 349-376.

Guyodo, Y., Acton, G.D., Brachfeld, S., Channell, J.E.T., 2001. A sedimentary paleomagnetic record of the Matuyama Chron from the western Antarctic margin (ODP Site 1101). Earth Planet. Sci. Lett. 191, 61-74.

Hass, H.C., 2002. A method to reduce the influence of ice-rafted debris on a grain size record from northern Fram Strait, Arctic Ocean. Polar Res. 21, 299-306.

Head, K.H., 2006. Manual of Soil Laboratory Testing: Volume 1: Soil Classification and Compaction Tests (3rd ed.). Whittles Publishing, Caithness, UK. 412 pp.

Hennekam, R., De Lange, G., 2012. X-ray fluorescence core scanning of wet marine sediments: methods to improve quality and reproducibility of high-resolution paleoenvironmental records. Limnol. Oceanogr. Methods 10, 991-1003.

Hepp, D.A., Mörz, T., Grützner, J., 2006. Pliocene glacial cyclicity in a deep-sea sediment drift (Antarctic Peninsula Pacific Margin). Palaeogeogr. Palaeoclimatol. Palaeoecol. 231, 181-198.

Hepp, D.A., Mörz, T., Hensen C., Frederichs, T., Kasten, S., Riedinger, N., Hay, W.W., 2009. A late Miocene–early Pliocene Antarctic deepwater record of repeated iron reduction events. Mar. Geol. 266, 198-211.

Hernández-Molina, F.J., Larter, R.D., Maldonado, A., Rodríguez-Fernández, J., 2006. Evolution of the Antarctic Peninsula Pacific margin offshore from Adelaide Island since the late Miocene: an example of a glacial passive margin. Terra Antart. Rep.12, 81-90.

Hernández-Molina, F.J., Larter, R.D., Maldonado, A., 2017. Neogene to Quaternary stratigraphic evolution of the Antarctic Peninsula, Pacific Margin offshore of Adelaide Island: Transitions from a non-glacial, through glacially-influenced to a fully glacial state. Global Planet. Change 156, 80-111.

Hillenbrand, C.-D., 1994. Spätquaräre Sedimentationsprozesse am Kontinentalrand des nordöstliche Bellingshausenmeeres (Antarktis). Diploma Thesis, Geological Institute of the University of Würzburg, Germany, 124 pp.

Hillenbrand, C.-D., Cortese, G., 2006. Polar stratification: A critical view from the Southern Ocean. Palaeogeogr. Palaeoclimatol. Palaeoecol. 242, 240-252.

Hillenbrand, C.-D., Ehrmann, W., 2002. Distribution of clay minerals in drift sediments on the continental rise west of the Antarctic Peninsula, ODP Leg 178, Sites 1095 and 1096. In: Barker, P.F., Camerlenghi, A., Acton, G.D., Ramsay, A.T.S. (Eds.), Proc. ODP Sci. Results, 178, pp. 1-29. (CD-ROM). Available from: Ocean Drilling Program, Texas A&M University, College Station, TX 77845-9547, U.S.A.

Hillenbrand, C.-D., Ehrmann, W., 2005. Late Neogene to Quaternary environmental changes in the Antarctic Peninsula region: evidence from drift sediments. Global Planet. Change 45, 165-191.

Hillenbrand, C.-D., Fütterer, D.K., 2002. Neogene to Quaternary deposition of opal on the continental rise west of the Antarctic Peninsula, ODP Leg 178, Sites 1095, 1096 and 1101. In: Barker, P.F., Camerlenghi, A., Acton, G.D., Ramsay, A.T.S. (Eds.), Proc. ODP Sci. Results, 178, pp. 1-33. (CD-ROM). Available from: Ocean Drilling Program, Texas A&M University, College Station, TX 77845-9547, U.S.A.

Hillenbrand, C.-D., Fütterer, D.K., Grobe, H., Frederichs, T., 2002. No evidence for a Pleistocene collapse of the West Antarctic Ice Sheet from continental margin sediments recovered in the Amundsen Sea. Geo-Mar. Lett. 22, 51-59.

Hillenbrand, C.-D., Grobe, H., Diekmann, B., Fütterer, D.K., 2003. Distribution of clay minerals and proxies for productivity in surface sediments of the Bellingshausen and Amundsen seas (West Antarctica) — relation to modern environmental conditions. Mar. Geol. 193, 253-271.

Hillenbrand, C.-D., Baesler, A., Grobe, H., 2005. The sedimentary record of the last glaciation in the western Bellingshausen Sea (West Antarctica): implications for the interpretation of diamictons in a polar-marine setting. Mar. Geol. 216, 191-204.

Hillenbrand, C.-D., Moreton, S.G., Caburlotto, A., Pudsey, C.J., Lucchi, R.G., Smellie, J.L., Benetti, S., Grobe, H., Hunt, J.B., Larter, R.D., 2008a. Volcanic time-markers for Marine Isotopic Stages 6 and 5 in Southern Ocean sediments and Antarctic ice cores: implications for tephra correlations between palaeoclimatic records. Quat. Sci. Rev. 27, 518-540.

Hillenbrand, C.-D., Camerlenghi, A., Cowan, E.A., Hernández-Molina, F.J., Lucchi, R.G., Rebesco, M., Uenzelmann-Neben, G., 2008b. The present and past bottom-current flow regime around the sediment drifts on the continental rise west of the Antarctic Peninsula. Mar. Geol. 255, 55-63.

Hillenbrand, C.-D., Ehrmann, W., Larter, R.D., Benetti, S., Dowdeswell, J.A., Ó Cofaigh, C., Graham, A.G.C., Grobe, H., 2009. Clay mineral provenance of sediments in the southern Bellingshausen Sea reveals drainage changes of the West Antarctic Ice Sheet during the Late Quaternary. Mar. Geol. 265, 1-18.

Hillenbrand, C.-D., Larter, R.D., Dowdeswell, J.A., Ehrmann, W., Ó Cofaigh, C., Benetti, S., Graham, A.G.C., Grobe, H., 2010. The sedimentary legacy of a palaeo-ice stream on the shelf of the southern Bellingshausen Sea: clues to West Antarctic glacial history during the Late Quaternary. Quat. Sci. Rev. 29, 2741-2763.

Hillenbrand, C.-D., 14 others, 2017. West Antarctic Ice Sheet retreat driven by Holocene warm water incursions. Nature 547, 43-48.

Huang, T.C., Watkins, N.D., Shaw, D.M., 1975. Atmospherically transported volcanic glass in deep-sea sediments: volcanism in sub-Antarctic latitudes of the South

Pacific during late Pliocene and Pleistocene time. Geol. Soc. Am. Bull. 86, 1305-1315.

Imbrie, J., Hays, J.D., Martinson, A. McIntyre, A., Mix, A.C., Morley, J.J., Pisias, N.G., Prell, W.L., Shackleton, N.J., 1984. The orbital theory of Pleistocene climate: Support from a revised chronology of the marine $\delta^{18}O$ record. In: Berger, A. (Ed.), Milankovitch and Climate, part 1, D. Reidel, Norwell, Mass., pp. 269-305.

Jaccard, S.L., Hayes, C.T., Martínez-García, A., Hodell, D.A., Anderson, R.F., Sigman, D.M., Haugh, G.H., 2013. Two modes of change in southern ocean productivity over the past million years. Science 339, 1419-1423.

Jaccard, S.L., Galbraith, E.D., Martínez-García, A., Anderson, R.F., 2016. Covariation of deep Southern Ocean oxygenation and atmospheric CO_2 through the last ice age. Nature 530, 207-210.

Jimenez-Espejo, F.J., 12 others, 2020. Late Pleistocene oceanographic and depositional variations along the Wilkes Land margin (East Antarctica) reconstructed with geochemical proxies in deep-sea sediments. Global Planet. Change 184, 103045.

Jung, M., Ilmberger, J., Mangini, A., Emeis, K.-C., 1997. Why some Mediterranean sapropels survived burn-down (and others did not). Mar. Geol. 141, 51-60.

Kasten, S., Zabel, M., Heuer, V., Hensen, C., 2004. Processes and signals of nonsteadystate diagenesis in deep-sea sediments and their pore waters. In: Wefer, G., Mulitza, S., Ratmeyer, V. (Eds.), The South Atlantic in the Late Quaternary. Reconstruction of material budgets and current systems. Springer, Berlin, Heidelberg, New York, pp. 431-459.

Korff, L., von Dobeneck, T., Frederichs, T., Kasten, S., Kuhn, G., Gersonde, R., Diekmann, B., 2016. Cyclic magnetite dissolution in Pleistocene sediments of the abyssal northwest Pacific Ocean: Evidence for glacial oxygen depletion and carbon trapping. Paleoceanography 31, 600-624.

Kyle, P.R., Seward, D., 1984. Dispersed rhyolitic tephra from New Zealand in deep-sea sediments of the Southern Ocean. Geology 12, 487-490.

Lamy, F., Gersonde, R., Winckler, G., Esper, O., Jaeschke, A., Kuhn, G., Ullermann, J., Martínez-García, A., Lambert, F., Kilian, R. (2014). Increased dust deposition in the Pacific Southern Ocean during glacial periods. Science 343, 403-407.

Larter, R.D., Cunningham, A.P., 1993. The depositional Pattern and distribution of glacial-interglacial sequences on the Antarctic Peninsula Pacific margin. Mar. Geol. 109, 203-219.

Larter, R.D., 17 others, 2014. Reconstruction of changes in the Amundsen Sea and Bellingshausen Sea sector of the West Antarctic Ice Sheet since the Last Glacial Maximum. Quat Sci Rev. 100, 55-86.

Larter, R.D., Hogan, K.A., Dowdeswell, D.A., 2016. Large sediment drifts on the upper continental rise west of the Antarctic Peninsula. In: Dowdeswell, J.A., Canals, M., Jakobsson, M., Todd, B.J., Dowdeswell, E.K. & Hogan, K.A. (Eds.), Atlas of Submarine Glacial Landforms: Modern, Quaternary and Ancient. Geol. Soc. London, Memoirs 46, pp. 401-402.

Lisiecki, L.E., Raymo, M.E., 2005. A Pliocene–Pleistocene stack of 57 globally distributed benthic $\delta^{18}O$ records. Paleoceanography 20, PA1003, doi:10.1029/2004PA001071.

Löwemark, L., O'Regan, M., Hanebuth, T.J.J., Jakobsson M., 2012. Late Quaternary spatial and temporal variability in Arctic deep-sea bioturbation and its relation to Mn cycles. Palaeogeogr. Palaeoclimatol. Palaeoecol. 365, 192-208.

Löwemark, L., März C., O'Regan, M., Gyllencreutz, R., 2014. Arctic Ocean Mn-stratigraphy: genesis, synthesis and interbasin correlation. Quat. Sci. Rev. 92, 97-111.

Lucchi, R.G., Rebesco, M., 2007. Glacial contourites on the Antarctic Peninsula margin: insight for palaeoenvironmental and palaeoclimatic conditions. In: Viana, A.R., Rebesco, M. (Eds.), Economic and Palaeoceanographic Significance of Contourite Deposits. Geol. Soc. London Special Publ. 276, pp. 111-127.

Lucchi, R.G., Rebesco, M., Camerlenghi, A., Busetti, M., Tomadin, L., Villa, G., Persico, D., Morigi, C., Bonci, M.C., Giorgetti, G., 2002. Mid-late Pleistocene glacimarine sedimentary processes of a high-latitude, deep-sea sediment drift (Antarctic Peninsula Pacific margin). Mar. Geol. 189, 343-370.

Macri, P., Sagnotti, L., Lucchi, R.G., Rebesco, M., 2006. A stacked record of relative geomagnetic paleointensity for the past 270 kyr from the western continental rise of the Antarctic Peninsula. Earth Planet. Sci. Lett. 252, 162-179.

Mangini, A., Eisenhauer, A., Walter, P., 1990. The response of manganese in the ocean to the climatic cycles in the Quaternary. Paleoceanography 5, 811-821.

Mangini, A., Jung, M., Laukenmann, S., 2001. What do we learn from peaks of uranium and of manganese in deep sea sediments? Mar. Geol. 177, 63-78.

Meinhardt, A.-K., März, C., Schuth, S., Lettmann, K. A., Schnetger, B., Wolff, J.-O., Brumsack, H.-J., 2016. Diagenetic regimes in Arctic Ocean sediments: implications for sediment geochemistry and core correlation. Geochim. Cosmochim. Acta 188, 125-146.

McCave, I.N., 1988. Biological pumping upwards of the coarse fraction of deep sea sediments. J. Sed. Petrol. 58, 148-158.

McCave, I.N., Andrews, J.T., 2019. Distinguishing current effects in sediments delivered to the ocean by ice. I. Principles, methods and examples. Quat. Sci. Rev. 212, 92-107.

McCave, I.N., Hall, I.R., 2006. Size sorting in marine muds: Processes, pitfalls, and prospects for paleoflow-speed proxies. Geochem., Geophys, Geosys. 7, Q10N05, doi:10.1029/2006GC001284.

McCave, I.N., Manighetti, B., Robinson, S.G., 1995. Sortable silt and fine sediment size/composition slicing: parameters for palaeocurrent speed and palaeoceanography. Paleoceanography 10, 593-610.

McCave, I.N., Crowhurst, S.C., Kuhn, G., Hillenbrand, C.-D., Meredith, M.P., 2014. Minimal change in Antarctic Circumpolar Current flow speed between the last Glacial and Holocene. Nat. Geosci. 7, 113-116.

McCave, I.N., Thornalley, D.J.R., Hall, I.R., 2017. Relation of sortable silt grain size to deep-sea current speeds: calibration of the 'Mud Current Meter'. Deep-Sea Res. I 127, 1-12.

McGinnis, J.P., Hayes, D.E., Driscoll, N.W., 1997. Sedimentary processes across the continental rise of the southern Antarctic Peninsula. Mar. Geol. 141, 91-109.

Middelburg, J.J., Soetaert, K., Herman, P.M.J., 1997. Empirical relationships for use in global diagenetic models. Deep-Sea Res. I 44, 327-344.

Moreton, S.G., Smellie, J.L., 1998. Identification and correlation of distal tephra layers in deep-sea sediment cores, Scotia Sea, Antarctica. Annals Glaciol. 27, 285-289.

Nitsche, F.O., Cunningham, A.P., Larter, R.D., Gohl, K., 2000. Geometry and development of glacial continental margin depositional systems in the Bellingshausen Sea. Mar. Geol. 162, 277-302.

Nürnberg, C.C., Bohrmann, G., Schlüter, M., Frank, M., 1997. Barium accumulation in the Atlantic sector of the Southern Ocean: results from 190.000-year records. Paleoceanography 12, 594–603.

Ó Cofaigh C., Dowdeswell J.A., Pudsey C.J., 2001. Late Quaternary iceberg rafting along the Antarctic Peninsula continental rise and in the Weddell and Scotia Seas. J. Quat. Res. 56, 308-321.

Ó Cofaigh C., 17 others, 2014. Reconstruction of ice-sheet changes in the Antarctic Peninsula since the Last Glacial Maximum. Quat. Sci. Rev. 100, 87-110.

Park, Y.K., Lee, J.I., Jung, J., Hillenbrand, C.-D., Yoo, K.-C., Kim, J., 2019. Elemental compositions of smectites reveal detailed sediment provenance changes during glacial and interglacial periods: The southern Drake Passage and Bellingshausen Sea, Antarctica. Minerals 9, 322, doi:10.3390/min9050322.

Parkinson, C.L., 2019. A 40-y record reveals gradual Antarctic sea ice increases followed by decreases at rates far exceeding the rates seen in the Arctic. Proc. Natl. Acad. Sci. 116, 14414-14423.

Peterson, C.D., Lisiecki, L.E., Stern, J.V, 2014. Deglacial whole-ocean $\delta^{13}C$ change estimated from 480 benthic foraminiferal records. Paleoceanography 29, 549-563.

Piper, D.I., Fowler, B., 1980. New constraint on the maintenance of Mn nodules at the sediment surface. Nature 286, 880-883.

Presti, M., Barbara, L., Denis, D., Schmidt, S., De Santis, L., Crosta, X., 2011. Sediment delivery and depositional patterns off Adélie Land (East Antarctica) in relation to late Quaternary climatic cycles. Mar. Geol. 284, 96-113.

Pudsey, C.J., 2000. Sedimentation on the continental rise west of the Antarctic Peninsula over the last three glacial cycles. Mar. Geol. 167, 313-338.

Pudsey, C.J., 2002. Neogene record of Antarctic Peninsula glaciation in continental rise sediments: ODP Leg 178, Site 1095. In: Barker, P.F., Camerlenghi, A., Acton, G.D., Ramsay, A.T.S. (Eds.), Proc. ODP Sci. Results, 178, pp. 1-25. (CD-ROM). Available from: Ocean Drilling Program, Texas A&M University, College Station, TX 77845-9547, U.S.A.

Pudsey, C.J., Camerlenghi, A., 1998. Glacial-interglacial deposition on a sediment drift on the Pacific margin of the Antarctic Peninsula. Antarct. Sci. 10, 286-308.

Pudsey, C.J., Howe, J.A., 1998. Quaternary history of the Antarctic Circumpolar Current: evidence from the Scotia Sea. Mar. Geol. 148, 83-112.

Rebesco, M., Larter, R.D., Camerlenghi, A., Barker, P.F., 1996. Giant sediment drifts on the continental rise west of the Antarctic Peninsula. Geo-Mar. Lett. 16, 65-75.

Rebesco, M., Larter, R.D., Barker, P.F., Camerlenghi, A., Vanneste, L.E., 1997. The history of sedimentation on the continental rise west of the Antarctic Peninsula. In: Barker, P.F., Cooper, A. (Eds.), Geology and Seismic Stratigraphy of the Antarctic Margin: Part 2. Antarct. Res. Ser. 71. American Geophysical Union, Washington DC, pp. 29-49.

Rebesco, M., Camerlenghi, A., Zanolla, C., 1998. Bathymetry and morphogenesis of the Continental Margin West of the Antarctic Peninsula. Terra Antart. 5, 715-725.

Rebesco, M., Pudsey, C., Canals, M., Camerlenghi, A., Barker, P., Estrada, F., Giorgetti, A., 2002. Sediment drift and deep-sea channel systems, Antarctic Peninsula Pacific Margin. In: Stow, D.A.V., Pudsey, C.J., Howe, J.A., Faugeres, J.C., Viana, A.R. (Eds.), Deep-Water Contourite Systems: Modern Drifts and Ancient Series, Seismic and Sedimentary Characteristics. Geol. Soc. London Memoirs 22, pp. 353-371.

Rebesco, M., Camerlenghi, A., Volpi, V., Neagu, C., Accettella, D., Lindberg, B., Cova, A., Zgur, F., and the MAGICO party, 2007. Interaction of processes and importance of contourites: insights from the detailed morphology of sediment drift 7, Antarctica. In: Viana, A.R., Rebesco, M. (Eds.), Economic and Palaeoceanographic Significance of Contourite Deposits. Geol. Soc. London Special Publ. 276, 95-110.

Rebesco, M., Hernández-Molina, F.J., Van Rooij, D., Wåhlin, A., 2014. Contourites and associated sediments controlled by deep-water circulation processes: state of the art and future considerations. Mar. Geol. 352, 111-154.

Reitz, A., Hensen, C., Kasten, S., Funk, J.A., de Lange, G.J., 2004. A combined geochemical and rock-magnetic investigation of a redox horizon at the last glacial/interglacial transition. Phys. Chem. Earth 29, 921-931.

Rignot, E., Mouginot, J., Scheuchl, B., van den Broeke, M., van Wessem, M.J., Morlighem, M., 2019. Four decades of Antarctic Ice Sheet mass balance from 1979-2017. Proc. Natl. Acad. Sci. USA 116, 1095-1103.

Roberts, A.P., 2015. Magnetic mineral diagenesis. Earth-Sci. Rev. 151, 1-47. doi:10.1016/j.earscirev.2015.09.010.

Sagnotti, L., Macri, P., Camerlenghi, A., Rebesco, M., 2001. Environmental magnetism of Antarctic late Pleistocene sediments and interhemispheric correlation of climatic events. Earth Planet. Sci. Lett. 192, 65-80.

Sanderson, B., 1985. How bioturbation supports manganese nodules at the sediment-water interface. Deep-Sea Res. 32, 1281-1285.

Scheuer, C., Gohl, K., Larter, R.D., Rebesco, M., Udintsev, G., 2006. Variability in Cenozoic sedimentation along the continental rise of the Bellingshausen Sea, West Antarctica. Mar. Geol. 227, 279-298.

Shane, P.A.R., Froggatt, P.C., 1992. Composition of widespread volcanic glass in deep-sea sediments of the Southern Pacific Ocean: an Antarctic source inferred. Bull. Volcanol. 54, 595-601.

Sikes, E.L., Samson, C.R., Guilderson, T.P., Howard, W.R., 2000. Old radiocarbon ages in the southwest Pacific Ocean during the last glacial period and deglaciation. Nature 405, 555-559.

Skinner, L.C, McCave, I.N., 2003. Analysis and modelling of gravity- and piston coring based on soil mechanics. Mar. Geol. 199, 181-204.

Skinner, L.C., Muschitiello, F., Scrivner, A.E., 2019. Marine reservoir age variability over the last deglaciation: Implications for marine carbon cycling and prospects for regional radiocarbon calibrations. Paleoceanogr. Paleoclimatol. 34, 1807-1815.

Smith, J.A., 14 others, 2017. Sub-ice-shelf sediments record history of twentieth-century retreat of Pine Island Glacier. Nature 541, 77-80.

Soetaert, K., Herman, P.M.J., Middelburg, J.J., de Stigter, H.S., van Weering, T.C.E., Epping, E., Helder, W., 1996. Modelling ^{210}Pb-derived mixing activity in ocean margin sediments: diffusive versus non-local mixing. J. Mar. Res. 54, 1207-1227.

Stow, D., Smillie, Z., 2020. Distinguishing between deep-water sediment facies: turbidites, contourites and hemipelagites. Geosci. 10, 68, doi:10.3390/geosciences10020068.

Swart, N.C., Gille, S.T., Fyfe, J.C., Gillett, N.P., 2018. Recent Southern Ocean warming and freshening driven by greenhouse gas emissions and ozone depletion. Nat. Geosci. 11, 836-841.

Tarduno, J.A., Wilkison, S.L., 1996. Non-steady state magnetic mineral reduction, chemical lock-in, and delayed remanence acquisition in pelagic sediments. Earth Planet Sci. Lett. 144, 315-326.

Thomson, J., Cook, G.T., Anderson, R., Mackenzie, A.B., Harkness, D.D., McCave, I.N., 1995. Radiocarbon age offsets in different-sized carbonate components of deep-sea sediments. Radiocarbon 37, 91-101.

Tjallingii, R., Röhl, U.,Kölling, M., Bickert, T., 2007. Influence of the water content on X-ray fluorescence core-scanning measurements in soft marine sediments, Geochem. Geophys. Geosyst. 8, Q02004, doi.org/10.1029/2006GC001393.

Turney, C.S.M., 31 others, 2020. Early Last Interglacial ocean warming drove substantial ice mass loss from Antarctica. Proc. Natl. Acad. Sci. USA, 117: 3996-4006.

Vautravers, M.J., Hodell, D.A., Channel, J.E.T., Hillenbrand, C.-D., Hall, M., Smith, J.A. & Larter, R.D., 2013. Palaeoenvironmental records from the West Antarctic Peninsula drift sediments over the last 75 ka. In: Hambrey, M.J., Barker, P. F., Barrett, P. J., Bowman, V., Davies, B., Smellie, J.L. & Tranter, M. (Eds.), Antarctic Palaeoenviroments and Earth-Surface Processes, Geol. Soc. London Special Publ. 318, pp. 263-276.

Venuti, A., Florindo, F., Carburlotto, A., Hounslow, M.W., Hillenbrand, C.-D., Strada, E., Talarico, F.M., Cavallo, A., 2011. Late Quaternary sediments from deep-sea sediment drifts on the Antarctic Peninsula Pacific margin: climatic control on provenance of minerals. J. Geophys. Res. 116, B06104. doi:10.1029/2010JB007952.

Villa, G., Persico, D., Bonci, M.C., Lucchi, R.G., Morigi, C., Rebesco, M., 2003. Biostratigraphic characterization and Quaternary microfossil palaeoecology in sediment drifts west of the Antarctic Peninsula - implications for cyclic glacial–interglacial deposition. Palaeogeogr. Palaeoclimatol. Palaeoecol. 198, 237-263.

Wagner, M., Hendy, I.L., 2017. Trace metal evidence for a poorly ventilated glacial Southern Ocean. Quat. Sci. Rev. 170, 109-120.

Weltje, G.J., Tjallingii, R., 2008. Calibration of XRF core scanners for quantitative geochemical logging of sediment cores: theory and application. Earth Planet. Sci. Lett. 274, 423-438.

Wiers, S., Snowball, I., O'Regan, M., Almqvist, B., 2019. Late Pleistocene chronology of sediments from the Yermak Plateau and uncertainty in dating based on geomagnetic excursions. Geochem. Geophys. Geosyst. 20, 3289-3310. doi:10.1029/2018GC007920.

Wiers, S., Snowball I, O'Regan, M., Pearce, C., Almqvist, B., 2020. The Arctic Ocean manganese cycle, an overlooked mechanism in the anomalous palaeomagnetic sedimentary record. Front. Earth Sci. 8, 75, doi:10.3389/feart.2020.00075.

Williams, T.J., Hillenbrand, C.-D., Piotrowski, A.M., Allen, C.S., Frederichs, T., Smith, J.A., Ehrmann, W., Hodell, D.A., 2019. Paleocirculation and ventilation history of Southern Ocean sourced deep water masses during the last 800,000 years. Paleoceanography Paleoclimatol. 34, 833-852.

Wouters, B., Martin-Español, A., Helm, V., Flament, T., van Wessem, J.M., Ligtenberg, S.R.M., van den Broeke, M.R., Bamber, J.L., 2015. Dynamic thinning of glaciers on the Southern Antarctic Peninsula, Science 348, 899-903.

Wu, L., Wang, R., Xiao, W., Ge, S., Chen, Z., Krijgsman, W., 2017. Productivity-climate coupling recorded in Pleistocene sediments off Prydz Bay (East Antarctica). Palaeogeogr. Palaeoclimatol. Palaeoecol. 485, 260-270.

Wu, L., Wang, R., Xiao, W., Krijgsman, W., Li, Q., Ge, S., Ma, T., 2018. Late Quaternary deep stratification-climate coupling in the Southern Ocean: Implications for changes in abyssal carbon storage. Geochem. Geophys. Geosyst. 19, 379-395. doi:10.1002/2017GC007250.

Xuan, C., Channell, J.E.T., 2010. Origin of apparent magnetic excursions in deep-sea sediments from Mendeleev-Alpha Ridge, Arctic Ocean. Geochem. Geophys. Geosyst. 11, Q02003. doi:10.1029/2009GC002879.

Xuan, C., Channell, J.E.T., Polyak, L., Darby, D.A., 2012. Paleomagnetism of Quaternary sediments from Lomonosov Ridge and Yermak Plateau: implications for age models in the Arctic Ocean. Quat. Sci. Rev. 32, 48-63. doi:10.1016/j.quascirev.2011.11.015.

Ziegler, M., Jilbert, T., de Lange, G.J., Lourens, L.J., Reichart, G.-J., 2008. Bromine counts from XRF scanning as an estimate of the marine organic carbon content of sediment cores. Geochem. Geophys. Geosyst. 9, Q05009. doi:10.1029/2007GC001932.

8. Table and figure captions

Tables

Table 1: Cruise, core ID, gear (GBC: giant box core, GC: gravity core, MUC: multiple core, PC: piston core), location (BS: Bellingshausen Sea), latitude (Lat), longitude (Long), water depth (WD), and recovery (Rec) for the sediment cores investigated in this study. Where applicable, the IDs for sites of IODP proposal 732-FULL-2 (Channell et al. 2008) are given under "Location".

Table 2: AMS ^{14}C dates on calcareous (micro-)fossils from seafloor surface sediments at sites GBC729/PC728 and GBC735/PC734.

Table 3: Age-depth fix points and linear sedimentation rates (LSR) for the investigated sediment cores. Ages for Marine Isotope Stage (MIS) boundaries are from Lisiecki & Raymo (2005). The LSR given for the lowermost part of a core is an estimated minimum based on the assumption that the next older interglacial sediments at the site lie just below the maximum penetration depth of the core.

Table 4: Facies identified in the JR298 sediment cores.

Table 5: Reconstructed changes in the investigated sedimentary records throughout Late Quaternary glacial-interglacial cycles.

Figures

Figure 1: Bathymetric map of the study area with locations of sediment cores analysed for this study (black symbols) and other core sites mentioned in the text (white dots). Numbering of the drifts west of the Antarctic Peninsula (*D1* to *D8*) follows Rebesco et al. (2002). Bathymetry is from IBCSO (Arndt et al. 2013). Belgica TMF: Belgica Trough Mouth Fan; BSD: Bellingshausen Sea Drift. Inset map shows study area within wider context of Antarctica. APIS: Antarctic Peninsula Ice Sheet; EAIS: East Antarctic Ice Sheet; WAIS: West Antarctic Ice Sheet.

Figure 2: Lithology and sedimentological data for core PC723/GBC724. Assignment of core intervals to Marine Isotope Stages (MIS) from Lisiecki & Raymo (2005) is also shown, with interglacial MIS highlighted by grey shading. Numbers in gravel column mark age-depth fix points (ages in ka) according to the RPI-based "trial" age model of

Channell et al. (2019), which the authors consider to be of poor quality, with bold numbers highlighting interglacial ages.

Figure 3: Lithology and sedimentological data for core PC726/GBC725. Assignment of core intervals to Marine Isotope Stages (MIS) from Lisiecki & Raymo (2005) is also shown, with interglacial MIS highlighted by grey shading. Numbers in gravel column mark age-depth fix points (ages in ka) according to the RPI-based age model of Channell et al. (2019), with bold numbers highlighting interglacial ages.

Figure 4: Lithology and sedimentological data for core PC727/GBC730. Assignment of core intervals to Marine Isotope Stages (MIS) from Lisiecki & Raymo (2005) is also shown, with interglacial MIS highlighted by grey shading.

Figure 5: Lithology and sedimentological data for core PC728/GBC729. Assignment of core intervals to Marine Isotope Stages (MIS) from Lisiecki & Raymo (2005) is also shown, with interglacial MIS highlighted by grey shading. Numbers in gravel column mark age-depth fix points (ages in ka) according to the RPI-based age model of Channell et al. (2019), with bold numbers highlighting interglacial ages.

Figure 6: Lithology and sedimentological data for core PC732/GBC731. Assignment of core intervals to Marine Isotope Stages (MIS) from Lisiecki & Raymo (2005) is also shown, with interglacial MIS highlighted by grey shading. Numbers in gravel column mark age-depth fix points (ages in ka) according to the RPI-based age model of Channell et al. (2019), with bold numbers highlighting interglacial ages.

Figure 7: Lithology and sedimentological data for core PC734/GBC735. Assignment of core intervals to Marine Isotope Stages (MIS) from Lisiecki & Raymo (2005) is also shown, with interglacial MIS highlighted by grey shading.

Figure 8: Lithology and sedimentological data for core PC736/GBC722. Assignment of core intervals to Marine Isotope Stages (MIS) from Lisiecki & Raymo (2005) is also shown, with interglacial MIS highlighted by grey shading. Numbers in gravel column mark age-depth fix points (ages in ka) according to the RPI-based age model of Channell et al. (2019), with bold numbers highlighting interglacial ages.

Figure 9: Lithology and sedimentological data for core PS2556-2/-1. Assignment of core intervals to Marine Isotope Stages (MIS) from Lisiecki & Raymo (2005) is also shown, with interglacial MIS highlighted by grey shading.

Figure 10: Lithology and sedimentological data for core PS1565-2. Assignment of core intervals to Marine Isotope Stages (MIS) from Lisiecki & Raymo (2005) is also shown, with interglacial MIS highlighted by grey shading.

Figure 11: Productivity proxies analysed on discrete samples (black dots) and with an XRF scanner in core PC723/GBC724. Mn/Al ratios are also shown.

Figure 12: Productivity proxies analysed on discrete samples (black dots) and with an XRF scanner in core PC727/GBC730. Mn/Al ratios are also shown.

Figure 13: Productivity proxies analysed on discrete samples (black dots) in core PS1565-2. Mn/Al ratios and abundances of micro-Mn nodules (in the fraction >63 µm) are also shown.

Figure 14: Seafloor surface sediments recovered at sites GBC729/PC728 and GBC735/PC734. AMS^{14}C dates obtained from calcareous (micro-)fossils from the two samples are given in Table 2.

Figure 15: Ternary diagrams for clay mineral assemblages across the core transect PS1565 – PC734 – PC727 from NE to SW along the Antarctic Peninsula continental rise (data for core PS1565 are from Hillenbrand & Ehrmann 2002). Clay mineral assemblages were re-calcuated on a kaolinite-free basis because kaolinite is present in trace amounts only. Clay mineral data from smectite-enriched tephra layers are excluded.

Figure 16: Example X-radiographs (negatives) for facies identified in the JR298 cores (Table 4). **Facies A**: bioturbated mud with scattered gravel grains; **Facies B**: structureless mud with scattered gravel grains; **Facies C**: mud alternating with thin silt and (partly normally graded) sandy silt layers; **Facies D**: mud alternating with subtle, (sub-)millimetre thin silt laminae; **Facies E**: mud alternating with a few centimetre thick gravelly sand and sandy gravel layers; **Facies F**: laminated mud with scattered gravel grains; **Facies G**: normally graded sandy gravel to gravelly sand with erosional base; **Facies H**: normally graded sand overlain by muddy sand; **Facies I**: deformed mud with silty to sandy layers and scattered gravel grains; **Facies J**: cross-laminated mud alternating with silt; **Facies K**: structureless bed of silty to sandy volcanic glass.

Figure1

Click here to access/download;Figure;Fig_1.jpg

Fig.1

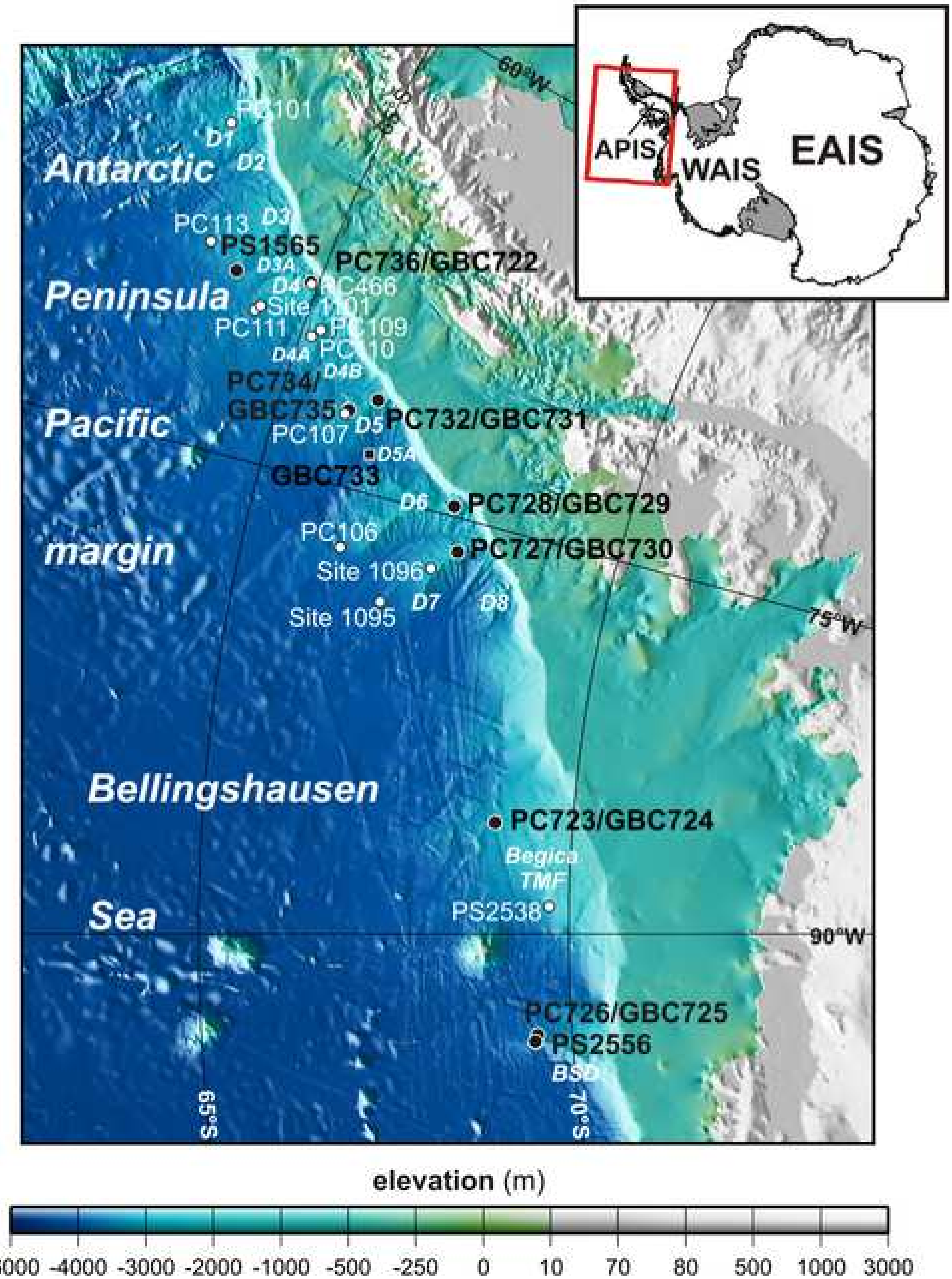

Figure2

Click here to access/download;Figure;Fig_2.jpg

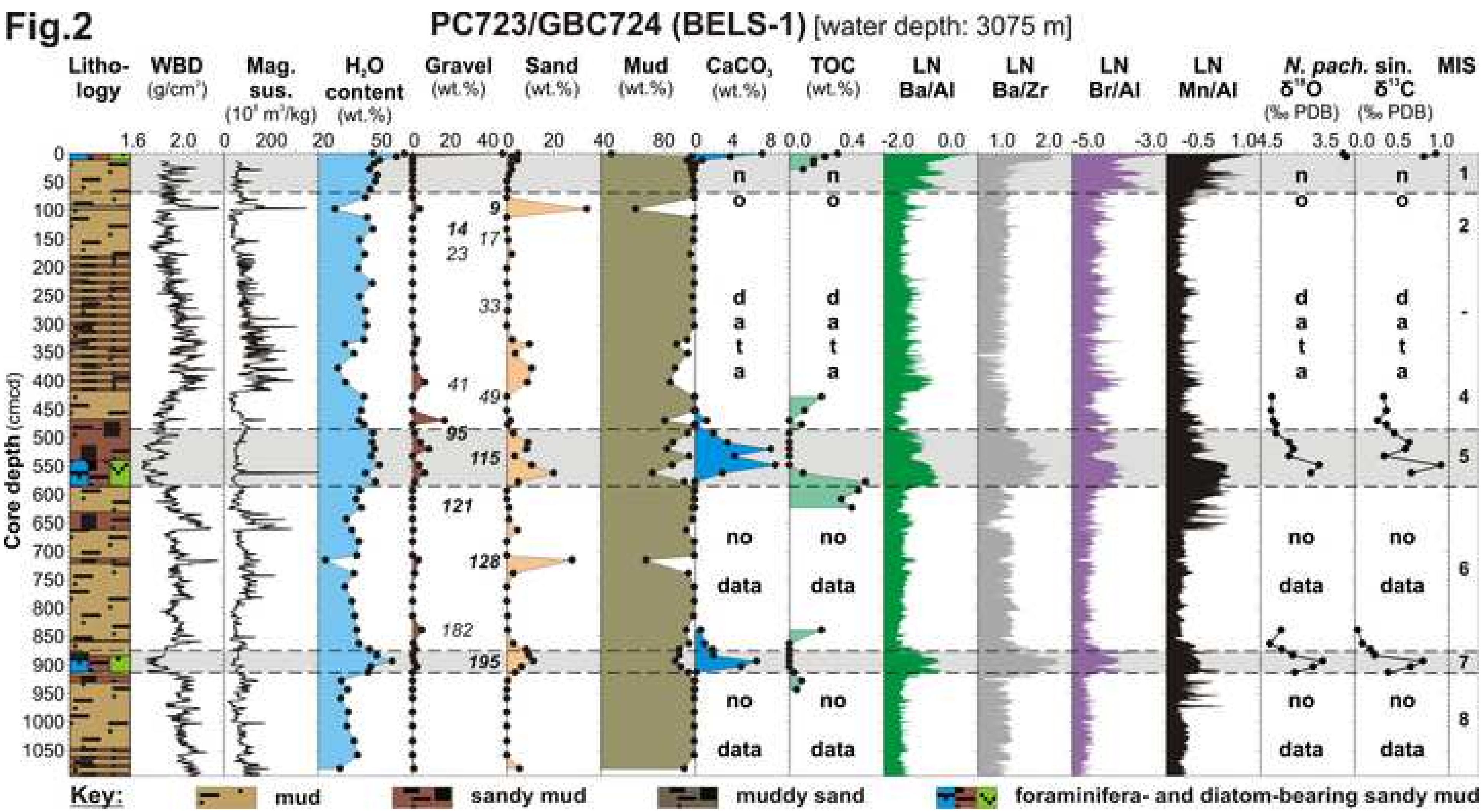

Figure3

Click here to access/download;Figure;Fig_3.jpg

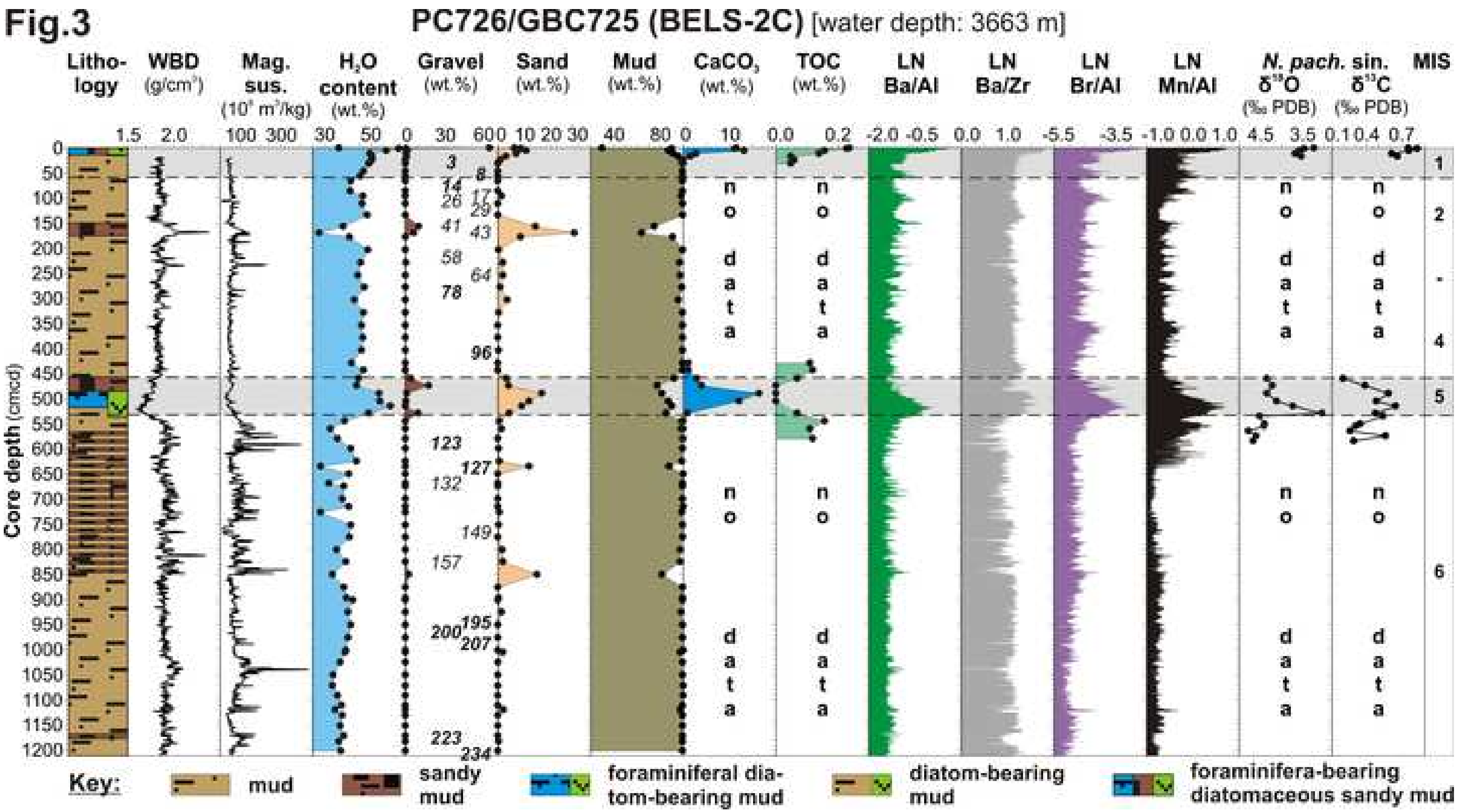

Figure4

Click here to access/download;Figure;Fig_4.jpg

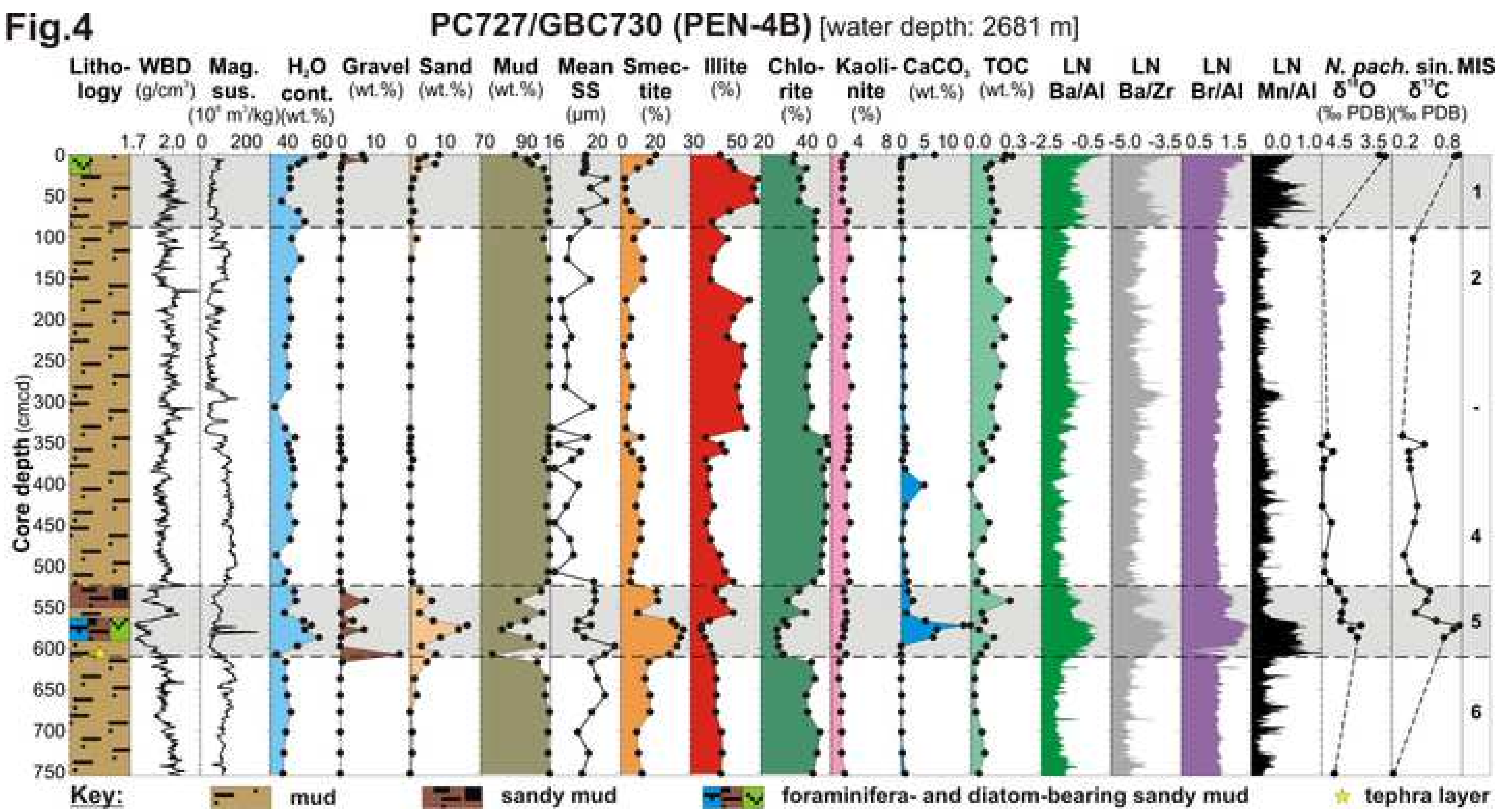

Figure5

Click here to access/download;Figure;Fig_5.jpg

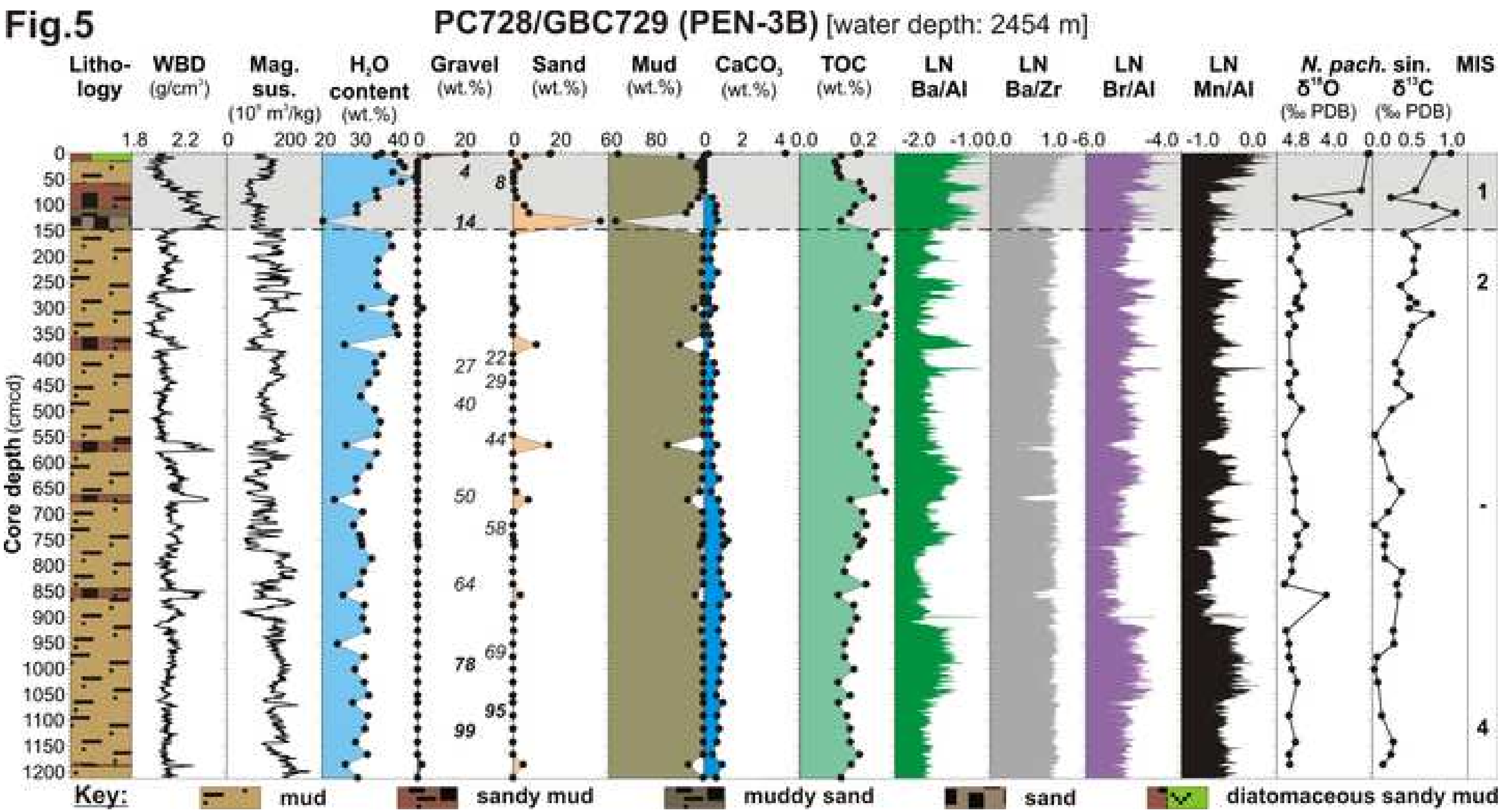

Figure6

Click here to access/download;Figure;Fig_6.jpg

Fig.6

PC732/GBC731 (PEN-2B) [water depth: 2647 m]

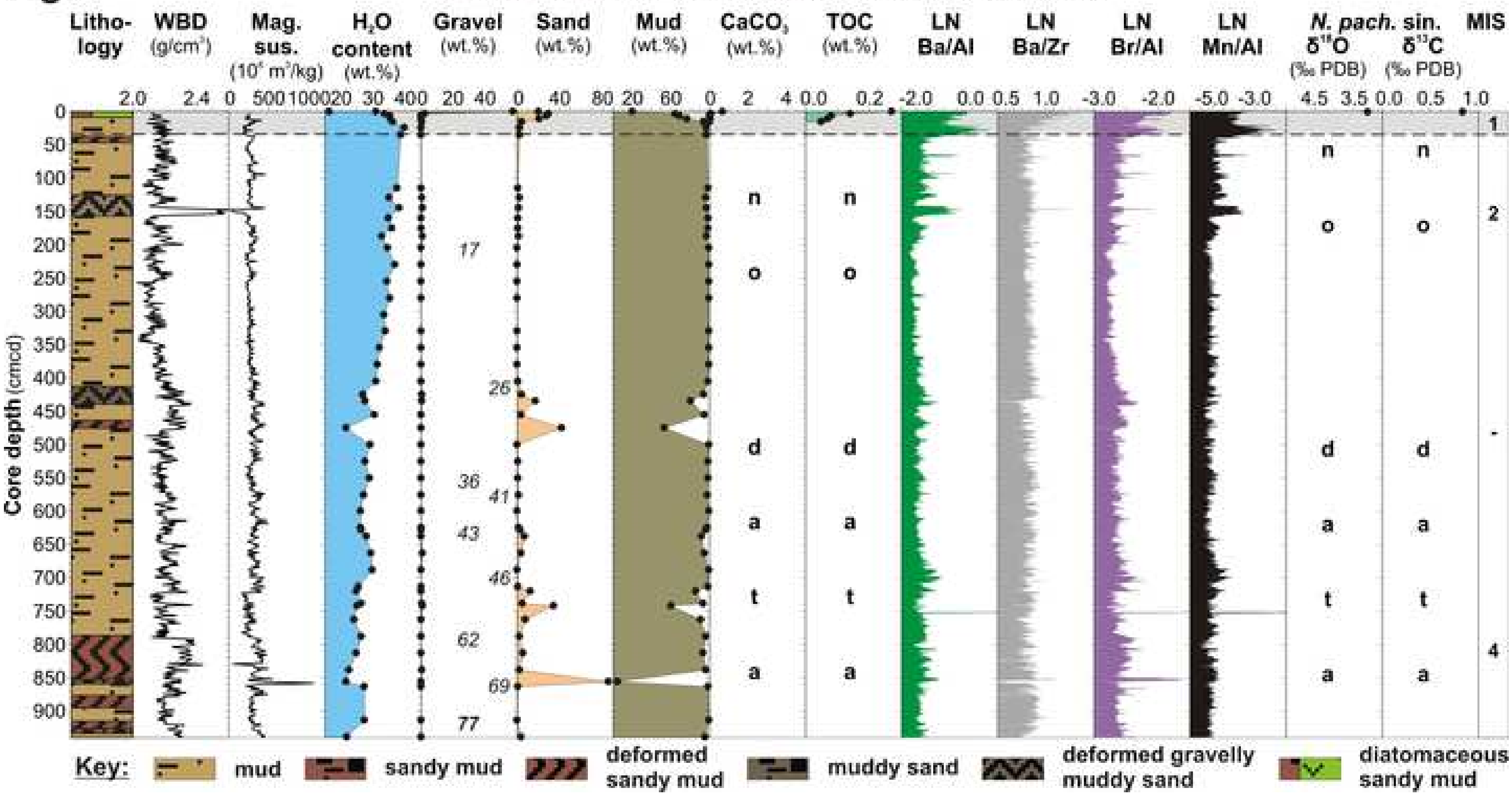

Figure7

Click here to access/download;Figure;Fig_7.jpg

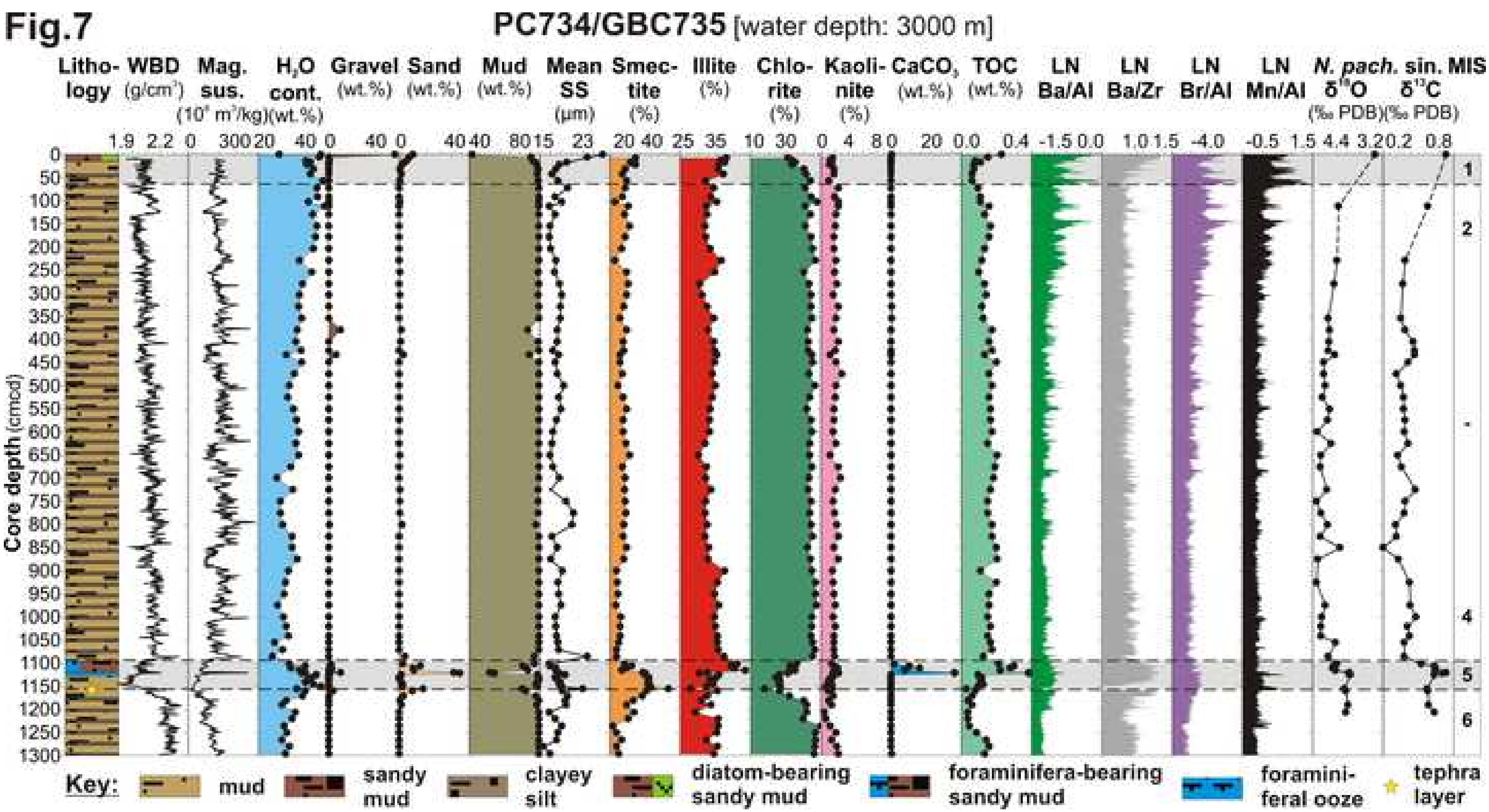

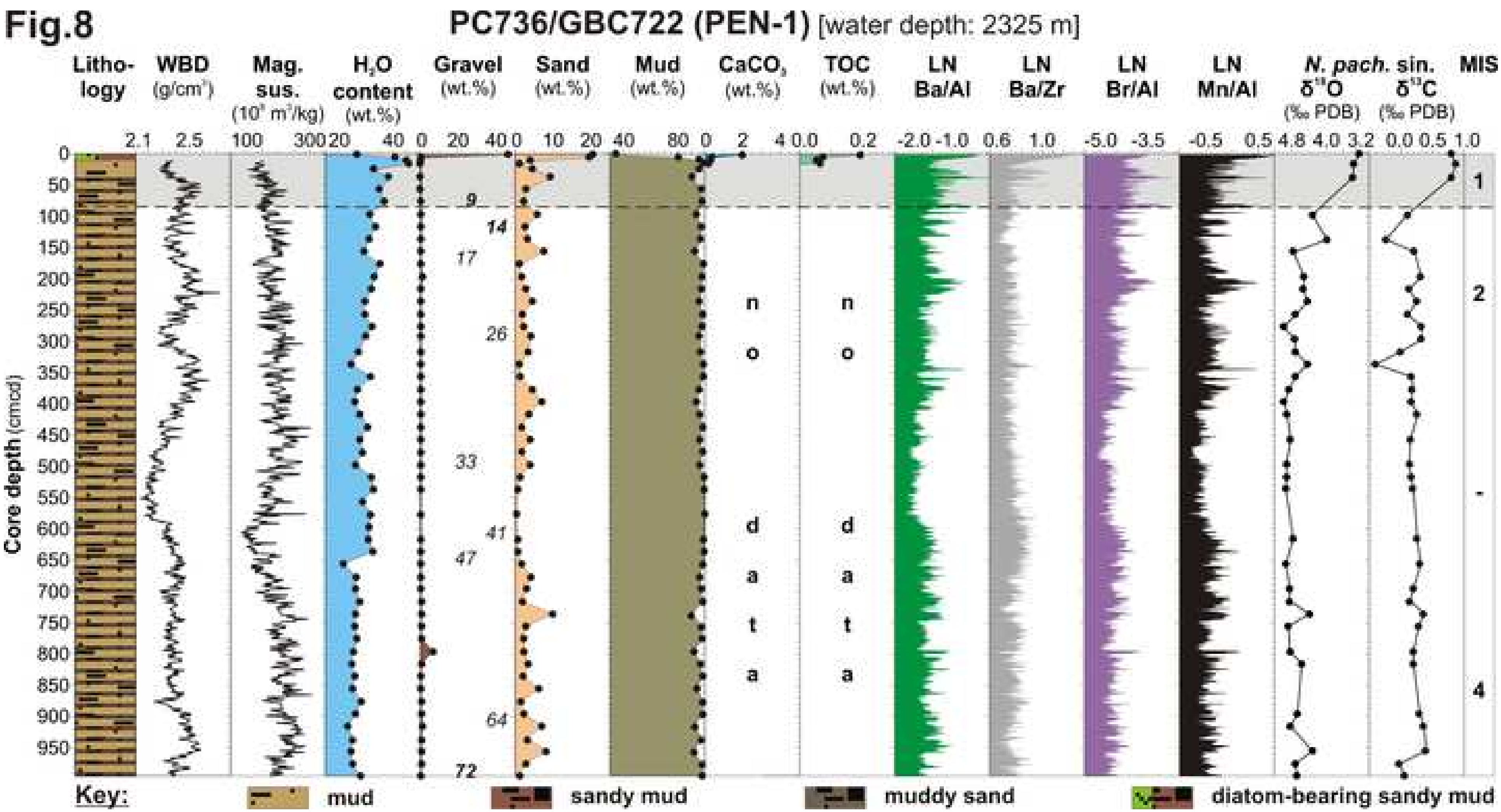
Fig.8
PC736/GBC722 (PEN-1) [water depth: 2325 m]
Litho-logy
WBD (g/cm³)
Mag. sus. (10⁻⁸ m³/kg)
H₂O content (wt.%)
Gravel (wt.%)
Sand (wt.%)
Mud (wt.%)
CaCO₃ (wt.%)
TOC (wt.%)
LN Ba/Al
LN Ba/Zr
LN Br/Al
LN Mn/Al
N. pach. sin. δ¹⁸O (‰ PDB)
δ¹³C (‰ PDB)
MIS
Core depth (cmcd)
no data
no data
Key:
mud
sandy mud
muddy sand
diatom-bearing sandy mud

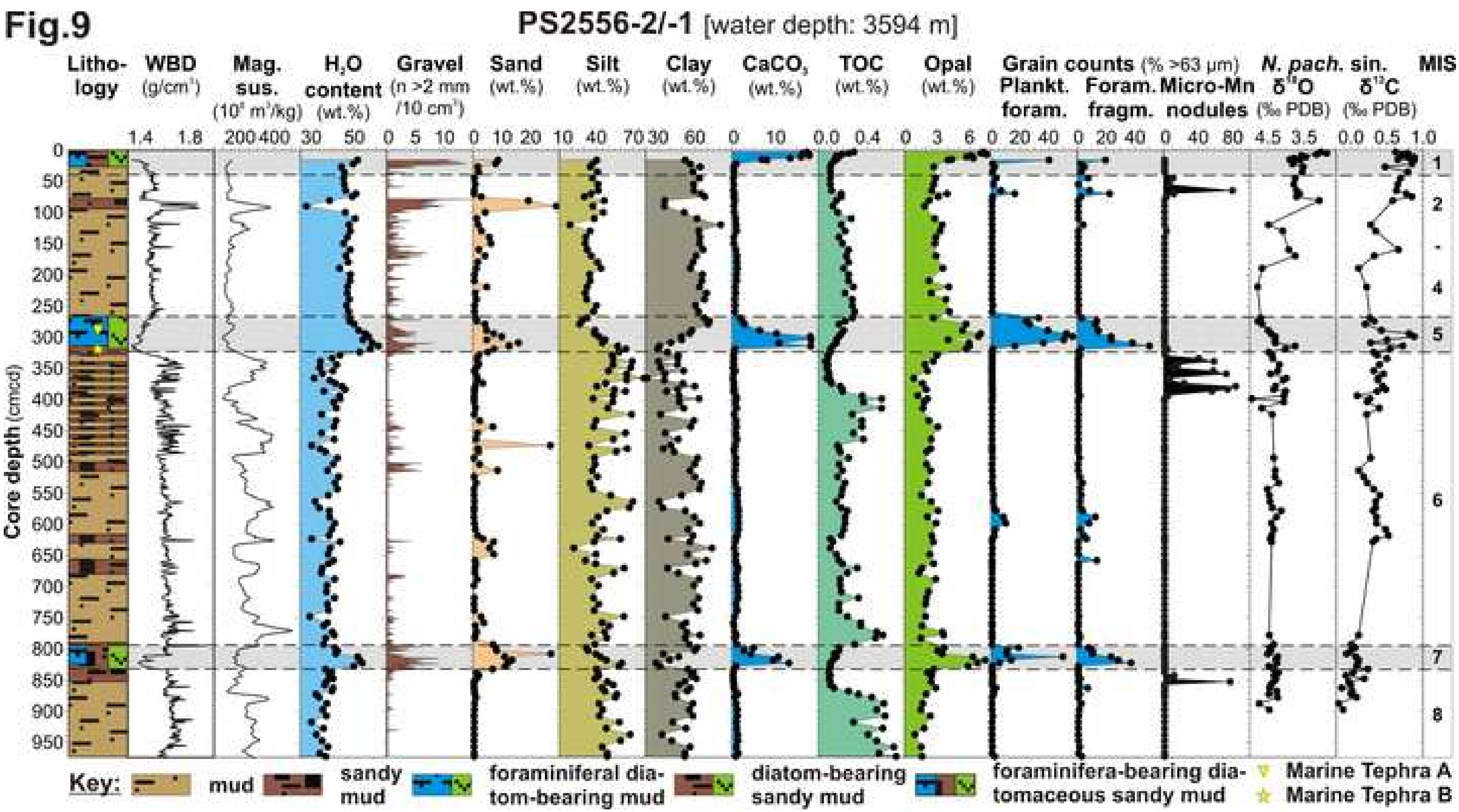
Fig.9
PS2556-2/-1 [water depth: 3594 m]
Litho-logy
WBD (g/cm³)
Mag. sus. (10⁻⁶ m³/kg)
H₂O content (wt.%)
Gravel (n >2 mm /10 cm³)
Sand (wt.%)
Silt (wt.%)
Clay (wt.%)
CaCO₃ (wt.%)
TOC (wt.%)
Opal (wt.%)
Grain counts (% >63 µm)
Plankt. foram.
Foram. fragm.
Micro-Mn nodules
N. pach. sin. δ¹⁸O (‰ PDB)
δ¹³C (‰ PDB)
MIS
Core depth (cmcd)
Key:
mud
sandy mud
foraminiferal diatom-bearing mud
diatom-bearing sandy mud
foraminifera-bearing diatomaceous sandy mud
Marine Tephra A
Marine Tephra B

Figure10

Click here to access/download;Figure;Fig_10.jpg

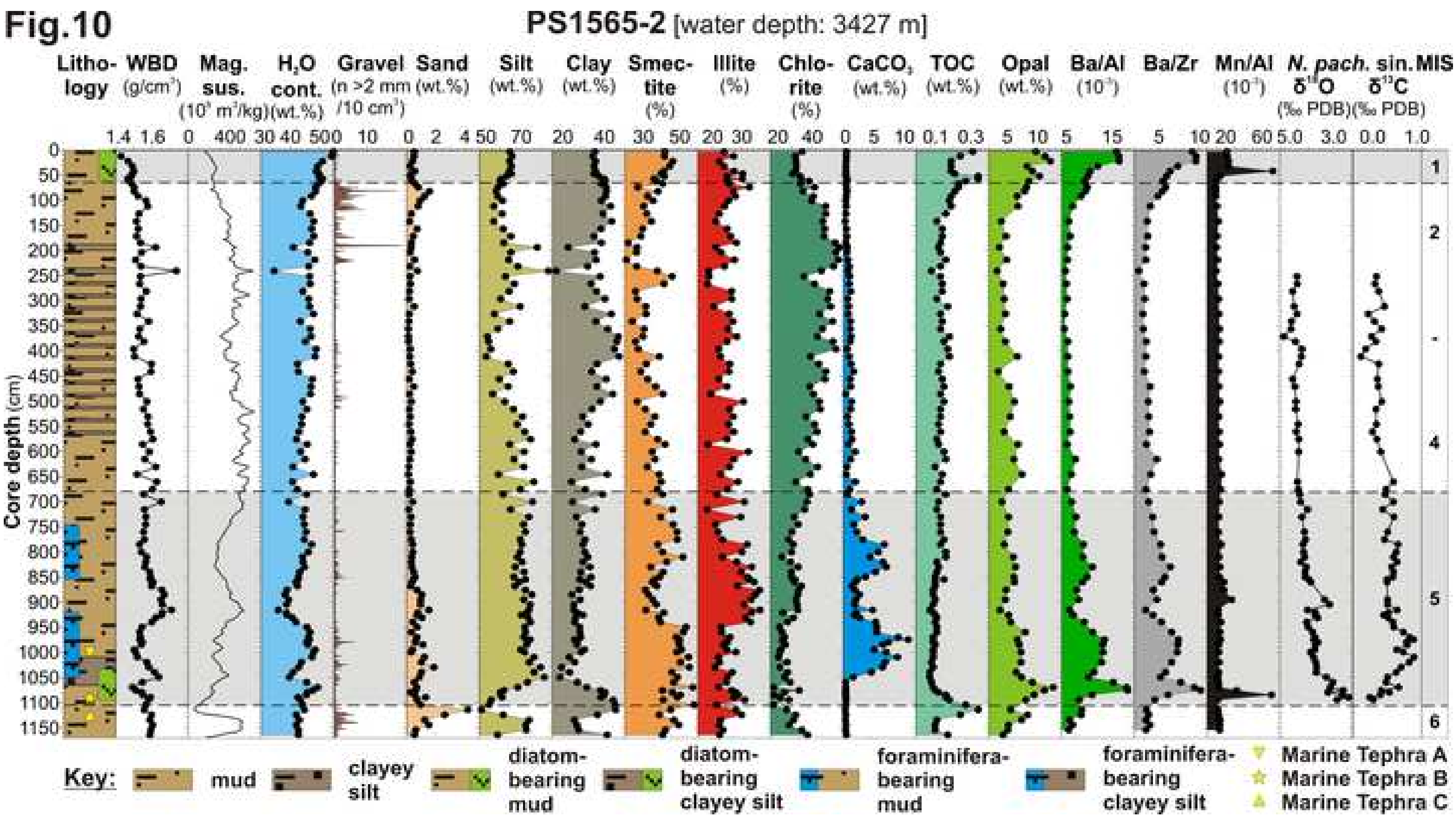

Figure11

Click here to access/download;Figure;Fig_11.jpg

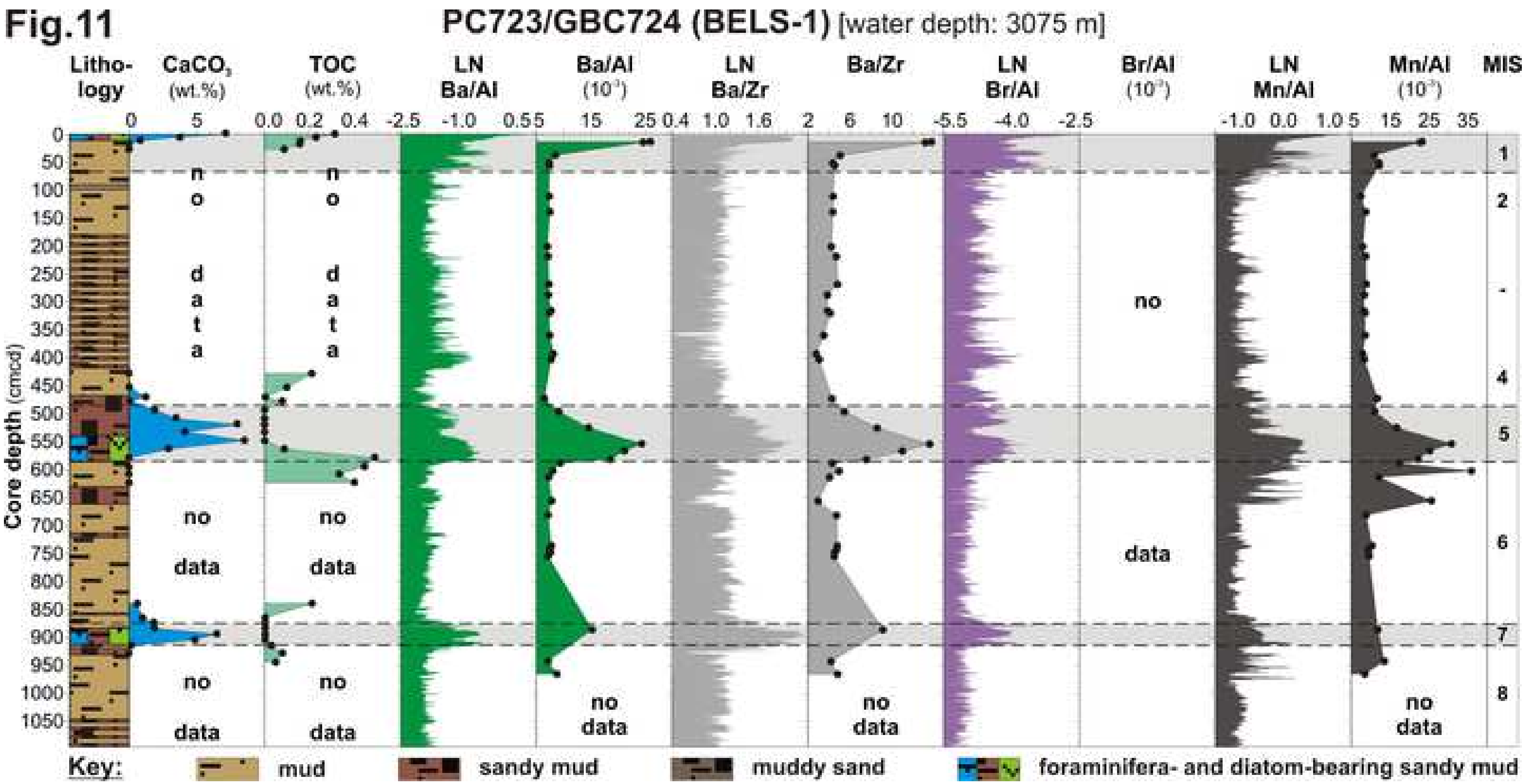

Figure12

Click here to access/download;Figure;Fig_12.jpg

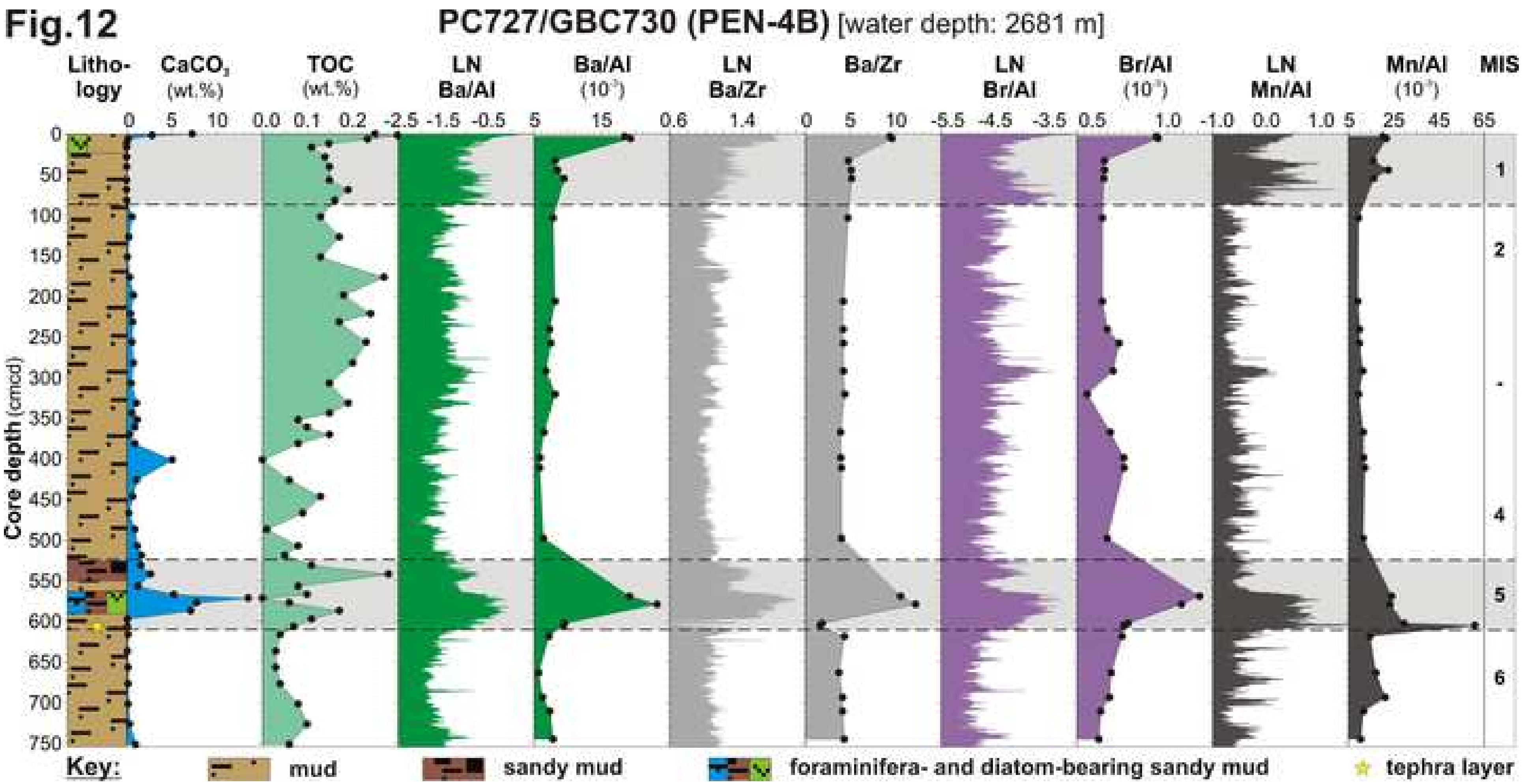

Figure13

Click here to access/download;Figure;Fig_13.jpg

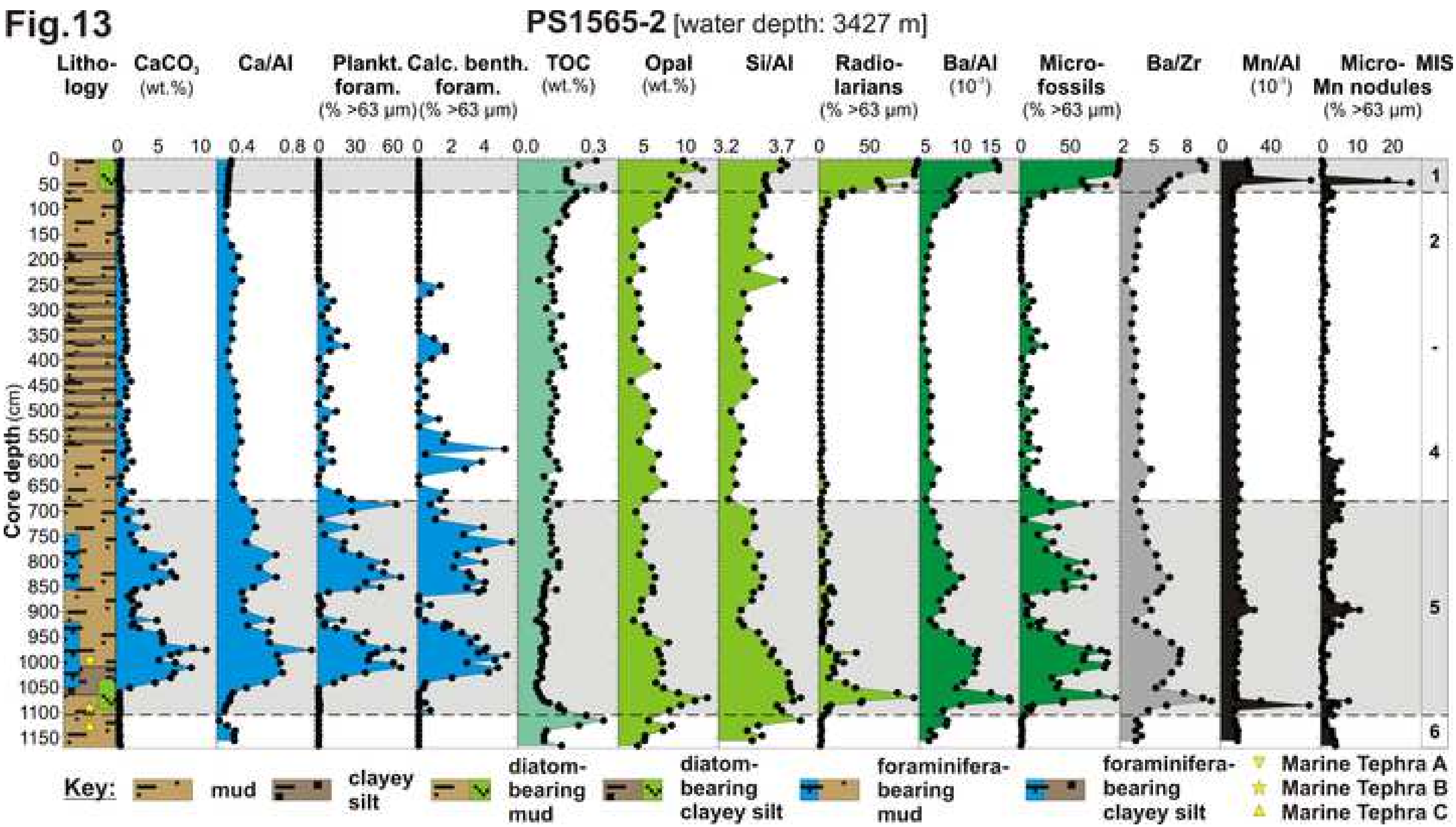

Figure14

Click here to access/download;Figure;Fig_14.jpg

Fig.14

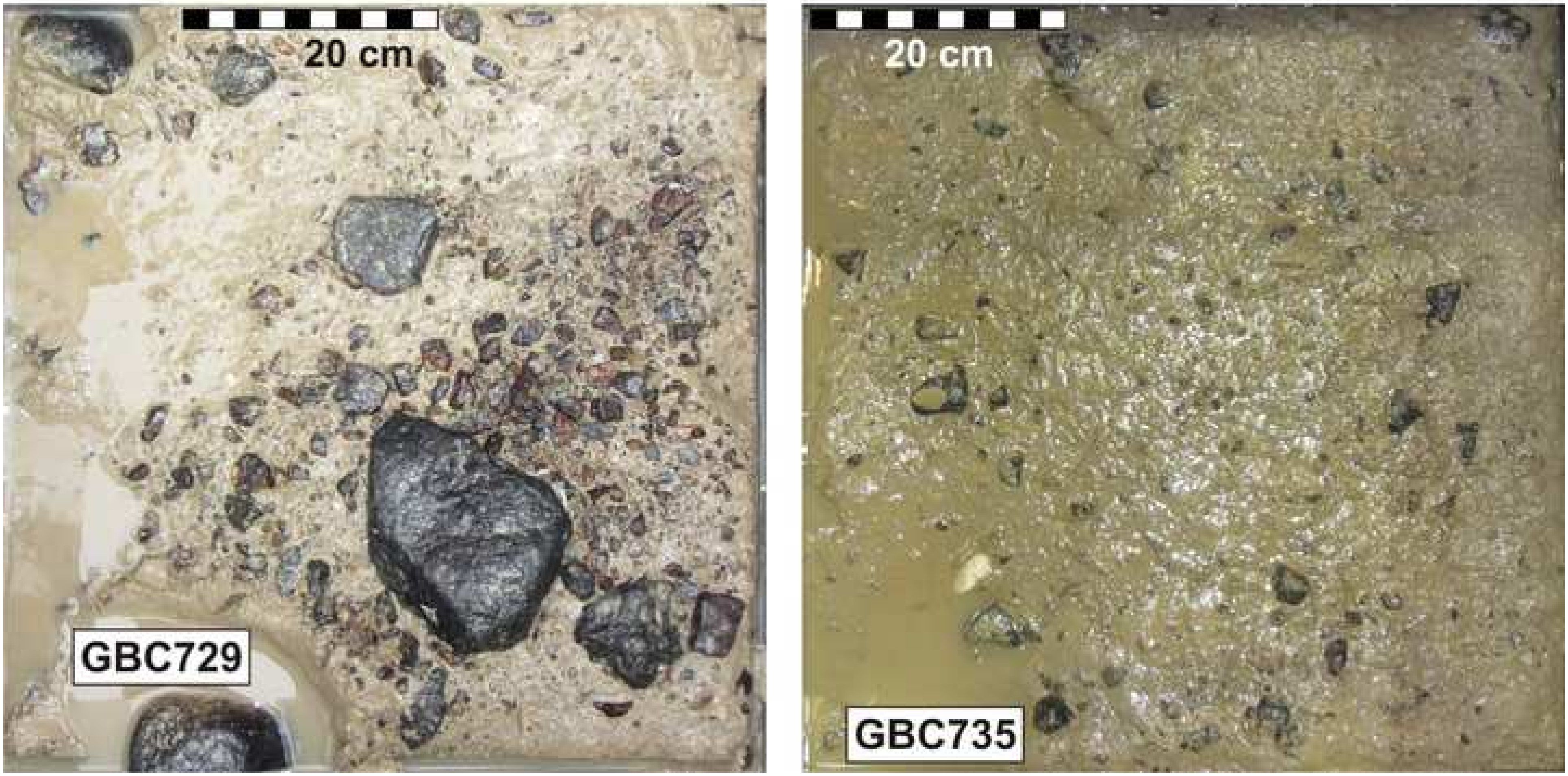

Fig.15

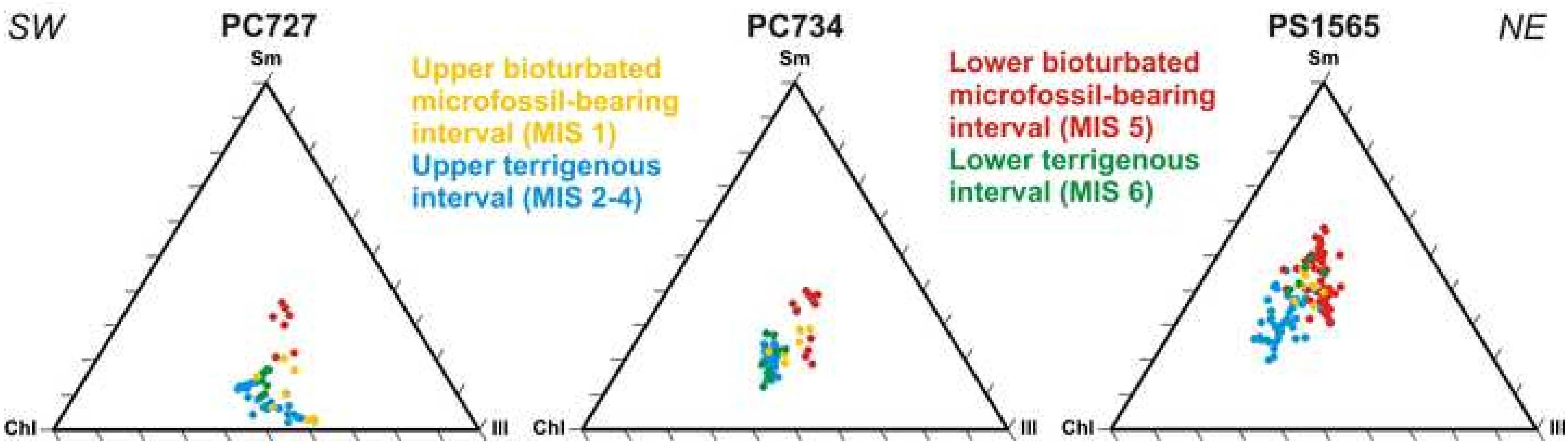
SW
PC727
PC734
PS1565
NE
Sm
Chl
Ill
Upper bioturbated microfossil-bearing interval (MIS 1)
Upper terrigenous interval (MIS 2-4)
Lower bioturbated microfossil-bearing interval (MIS 5)
Lower terrigenous interval (MIS 6)

Figure16

Fig.16

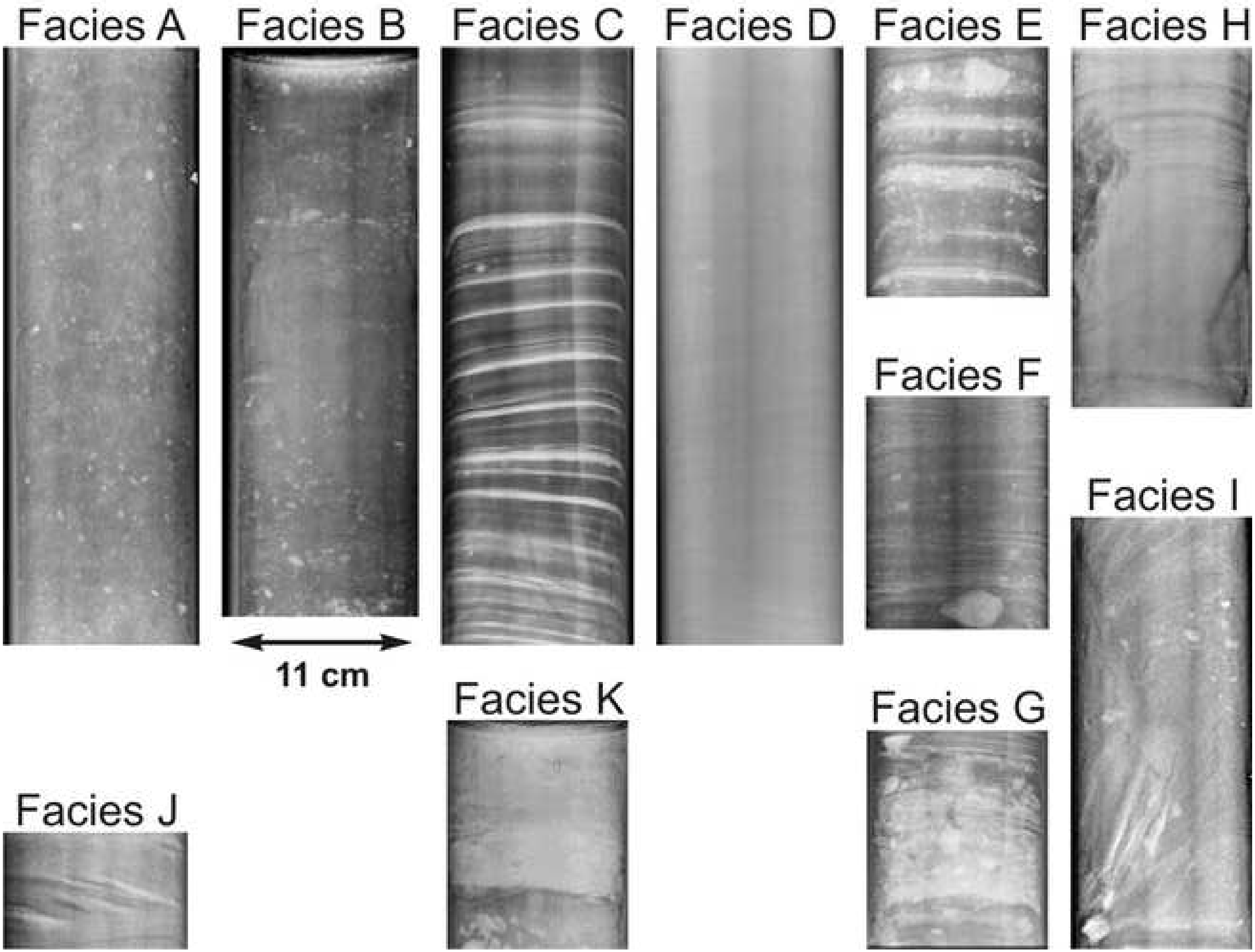

Suppl. Fig.1

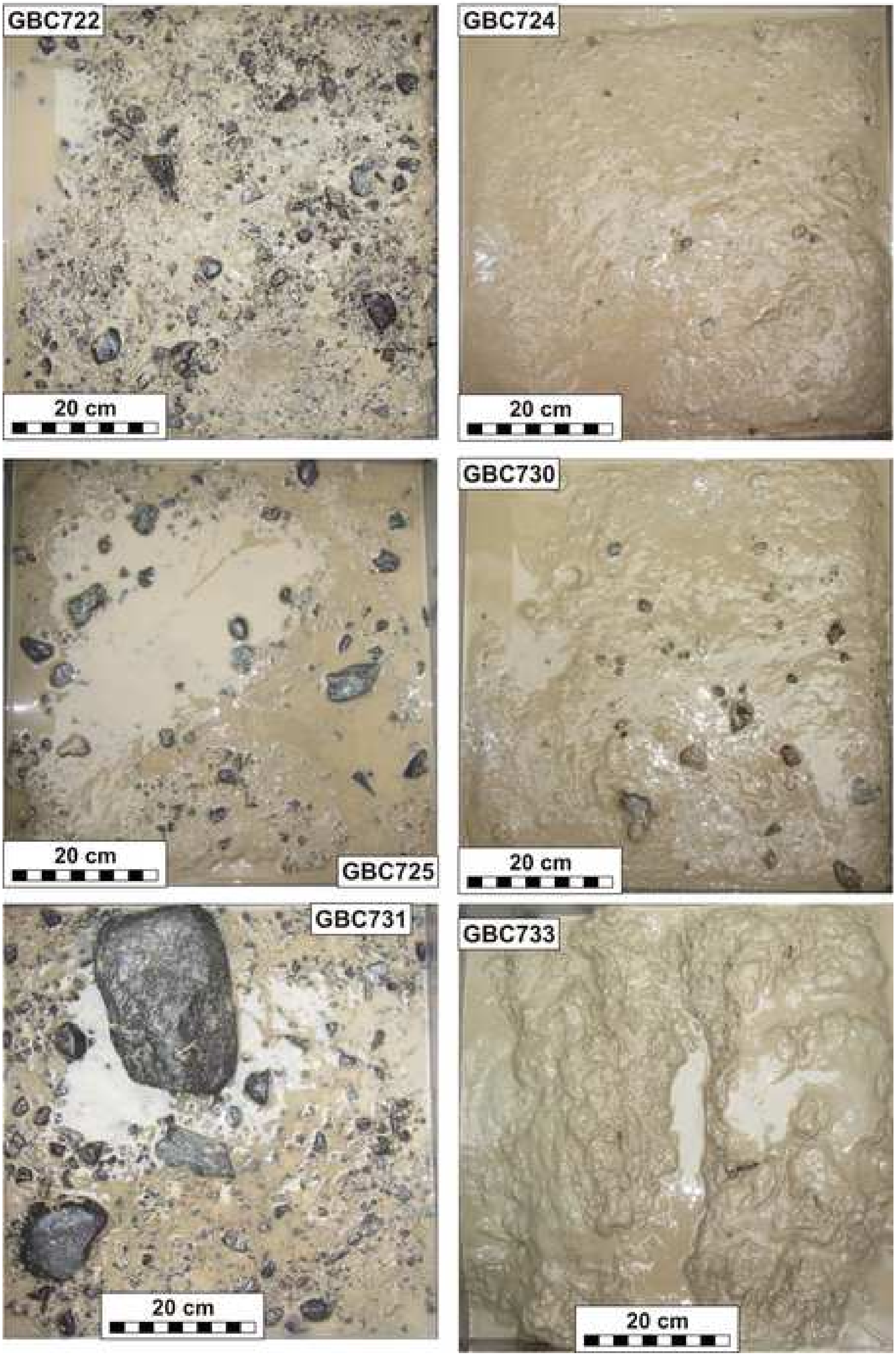
GBC722
20 cm
GBC724
20 cm
20 cm
GBC725
GBC730
20 cm
GBC731
20 cm
GBC733
20 cm

Suppl. Fig.2

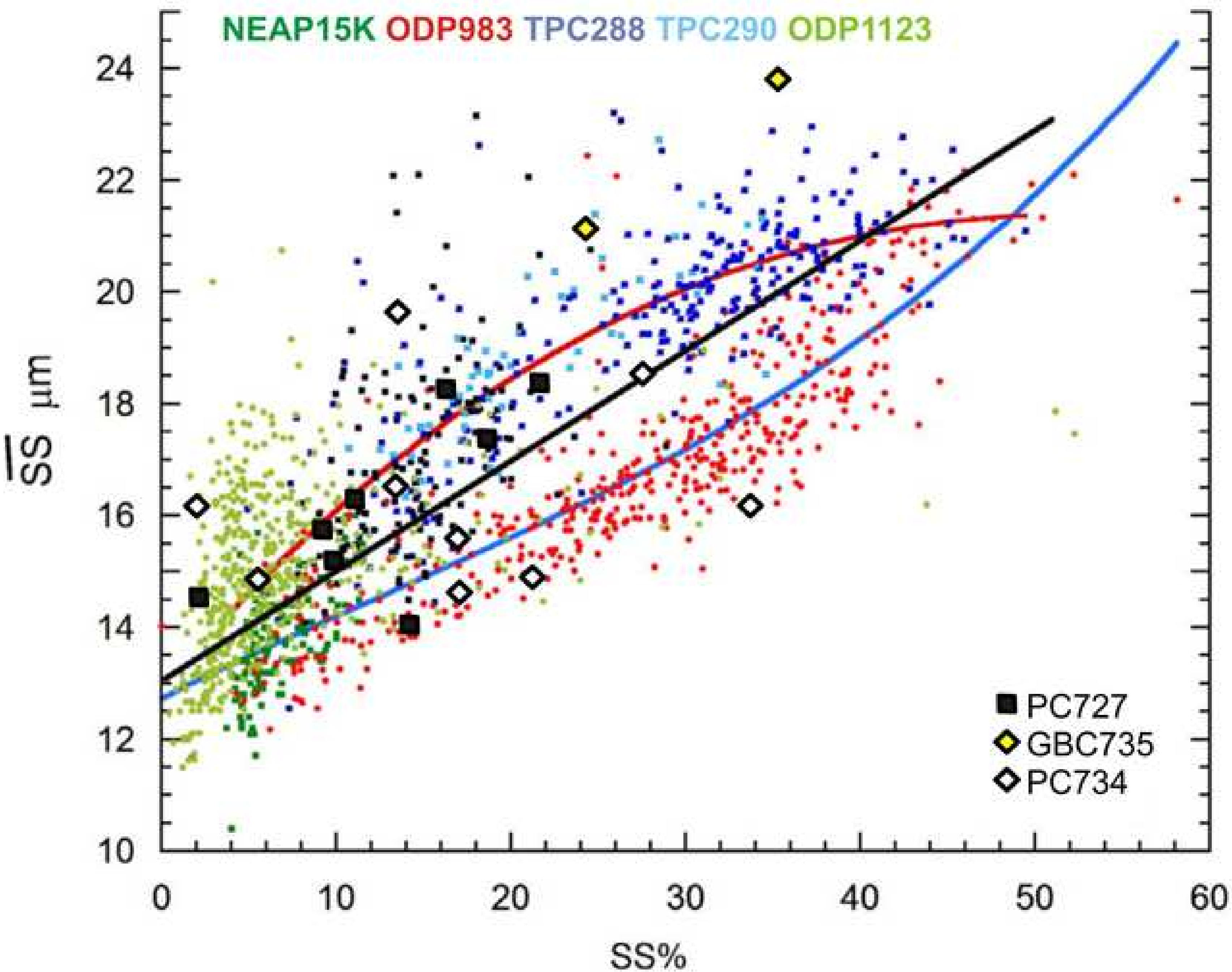
NEAP15K ODP983 TPC288 TPC290 ODP1123
24
22
20
18
16
14
12
10
$\overline{SS}$ µm
0
10
20
30
40
50
60
SS%
PC727
GBC735
PC734

Suppl. Fig.3a)

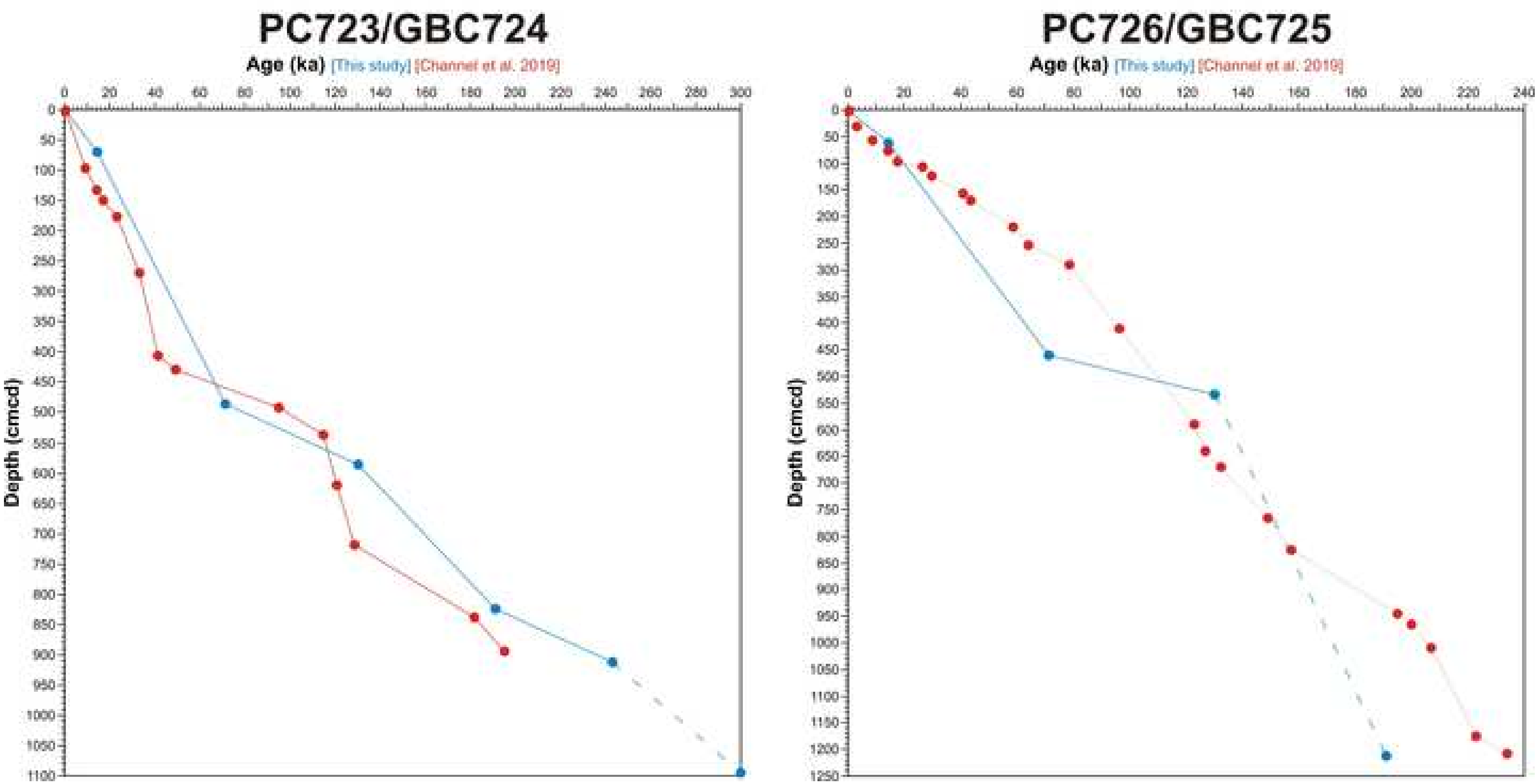
PC723/GBC724
Age (ka) [This study] [Channel et al. 2019]
Depth (cmcd)
PC726/GBC725
Age (ka) [This study] [Channel et al. 2019]
Depth (cmcd)

Suppl. Fig.3b)

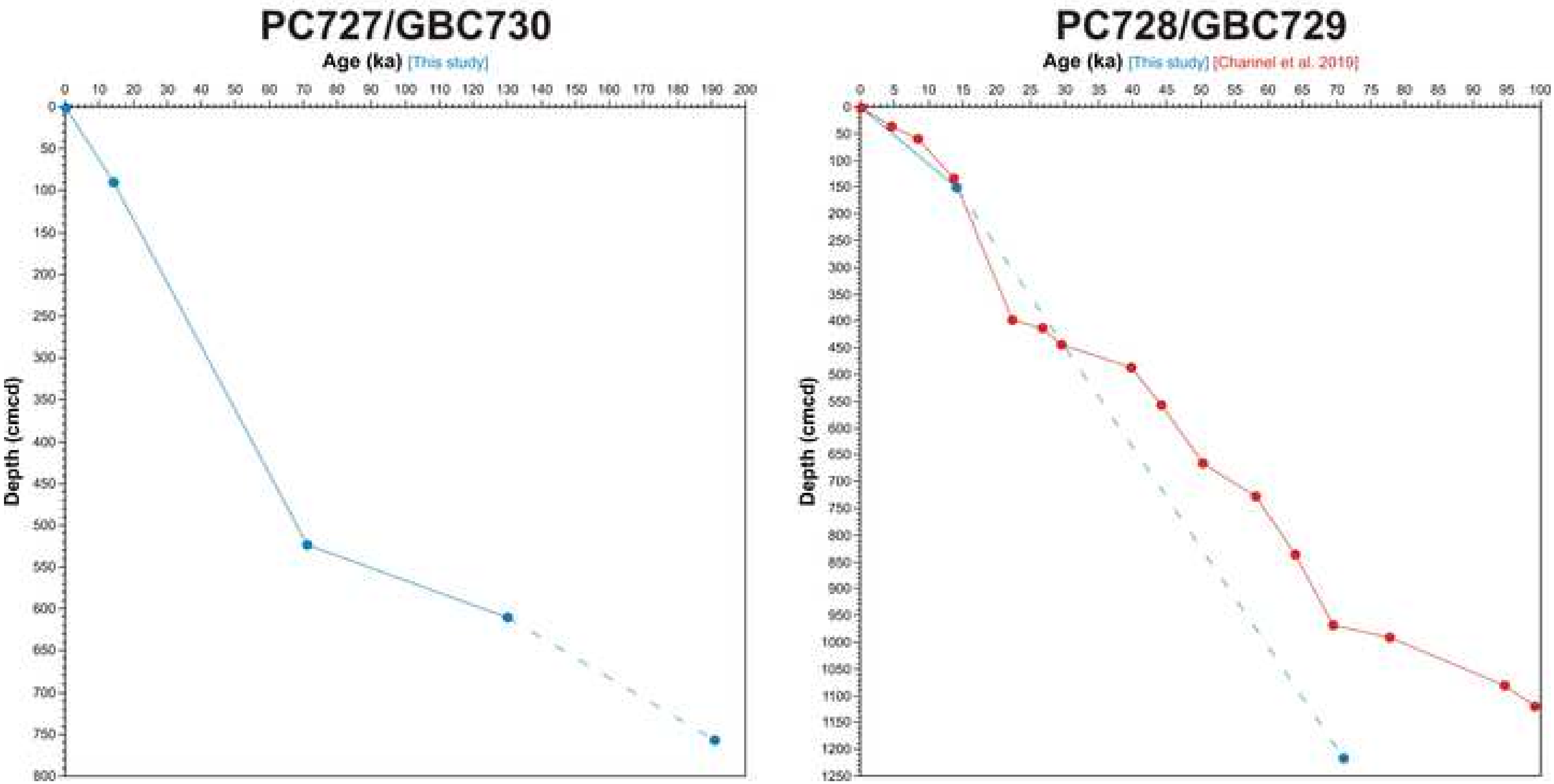
PC727/GBC730
Age (ka) [This study]
Depth (cmcd)
PC728/GBC729
Age (ka) [This study] [Charinel et al. 2019]
Depth (cmcd)

Suppl_Fig3c

Click here to access/download;Figure;Suppl_Fig_3c.jpg

Suppl. Fig.3c)

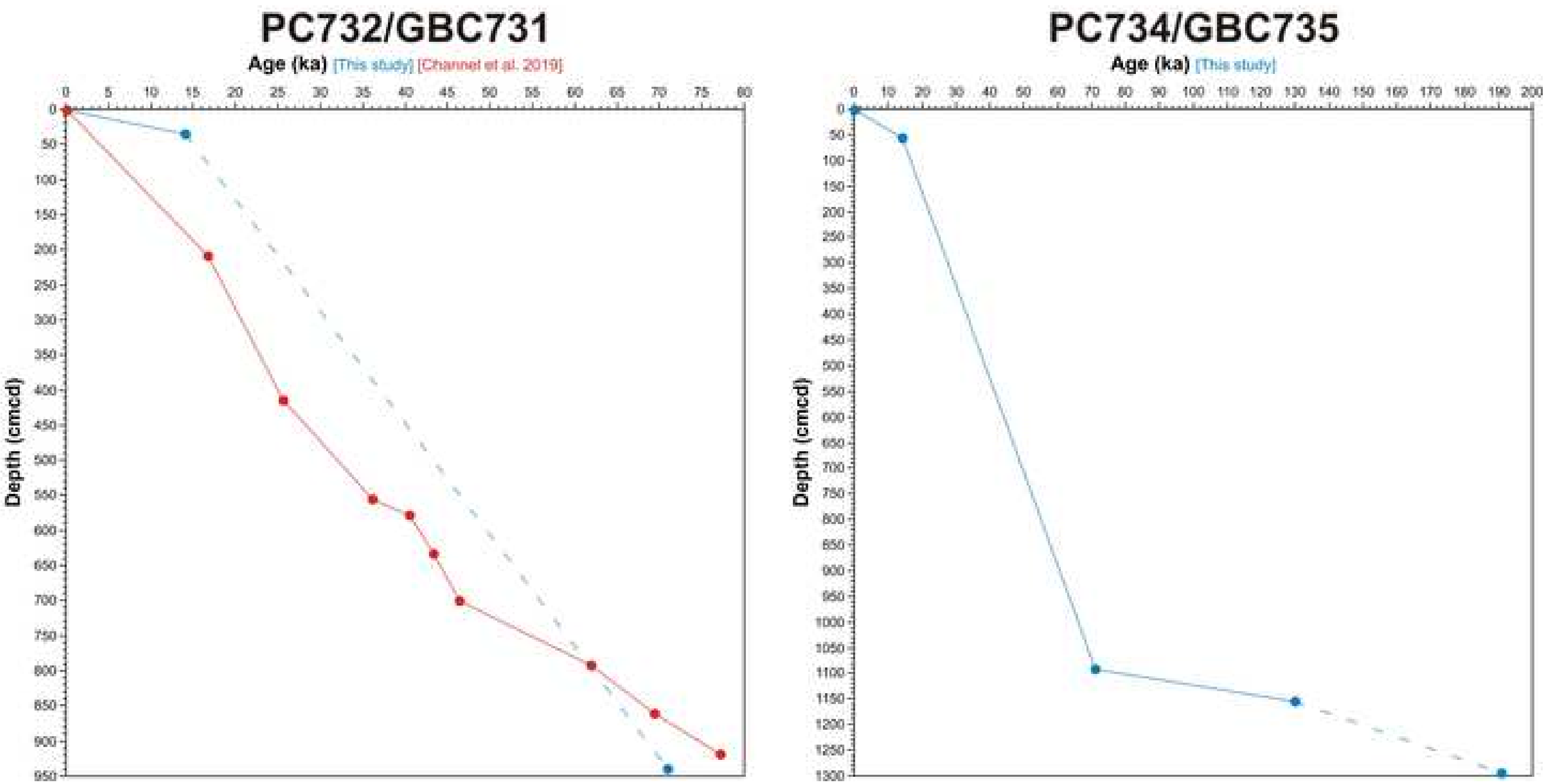

Suppl_Fig3d

Click here to access/download;Figure;Suppl_Fig_3d.jpg

Suppl. Fig.3d)

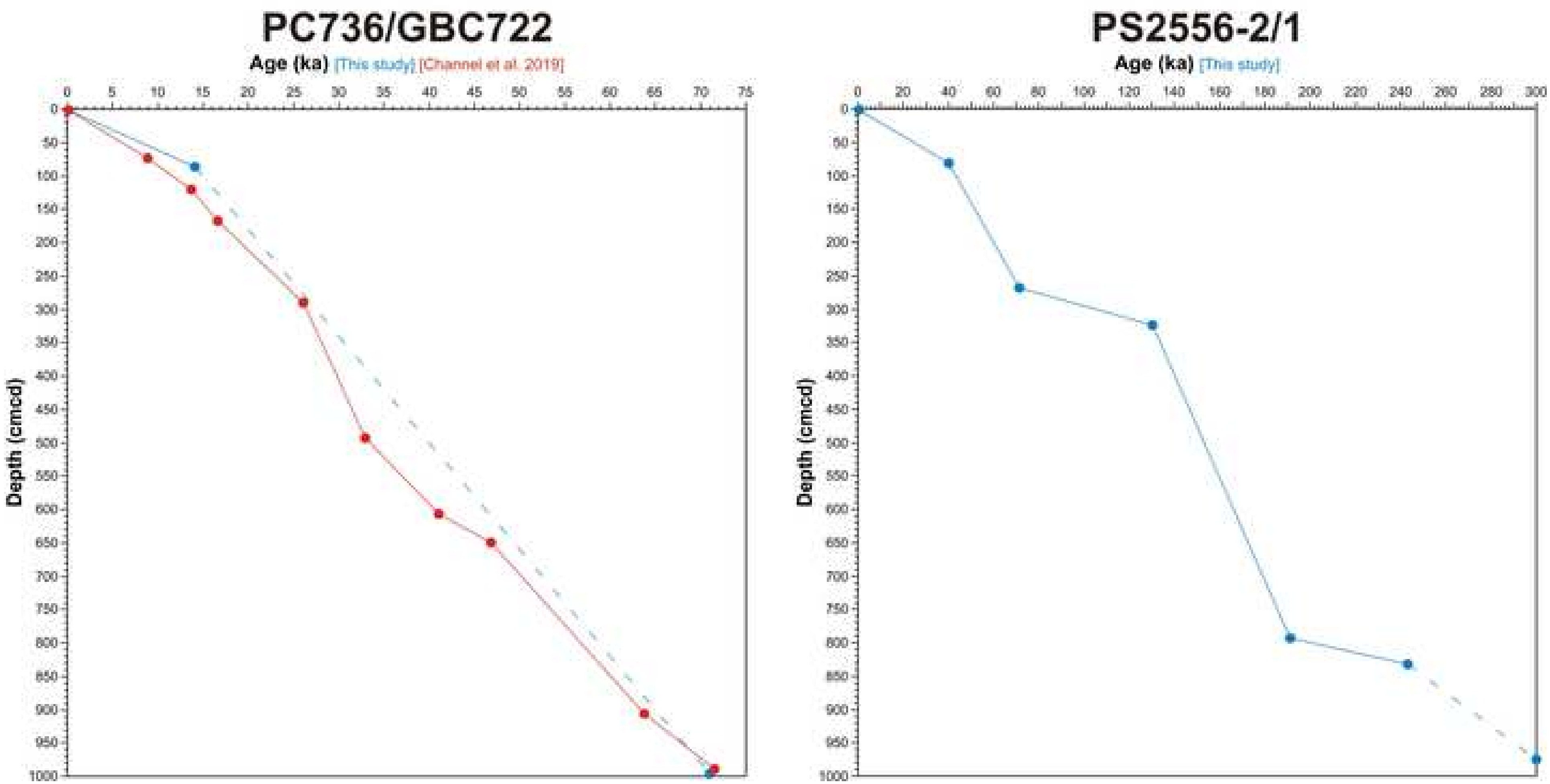

Suppl. Fig.3e)

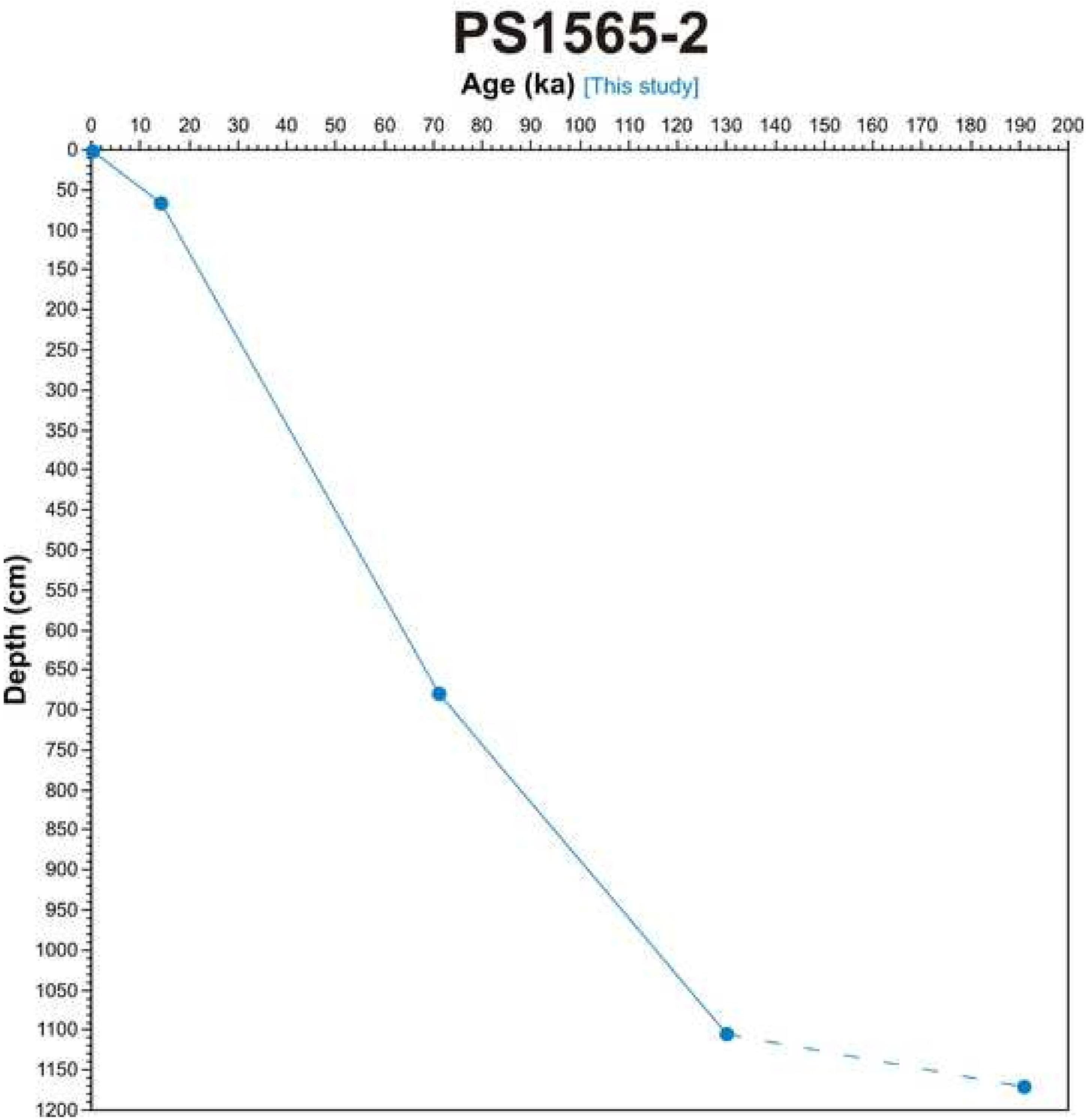

PS1565-2
Age (ka) [This study]
0
10
20
30
40
50
60
70
80
90
100
110
120
130
140
150
160
170
180
190
200
Depth (cm)
0
50
100
150
200
250
300
350
400
450
500
550
600
650
700
750
800
850
900
950
1000
1050
1100
1150
1200

Suppl. Fig.4

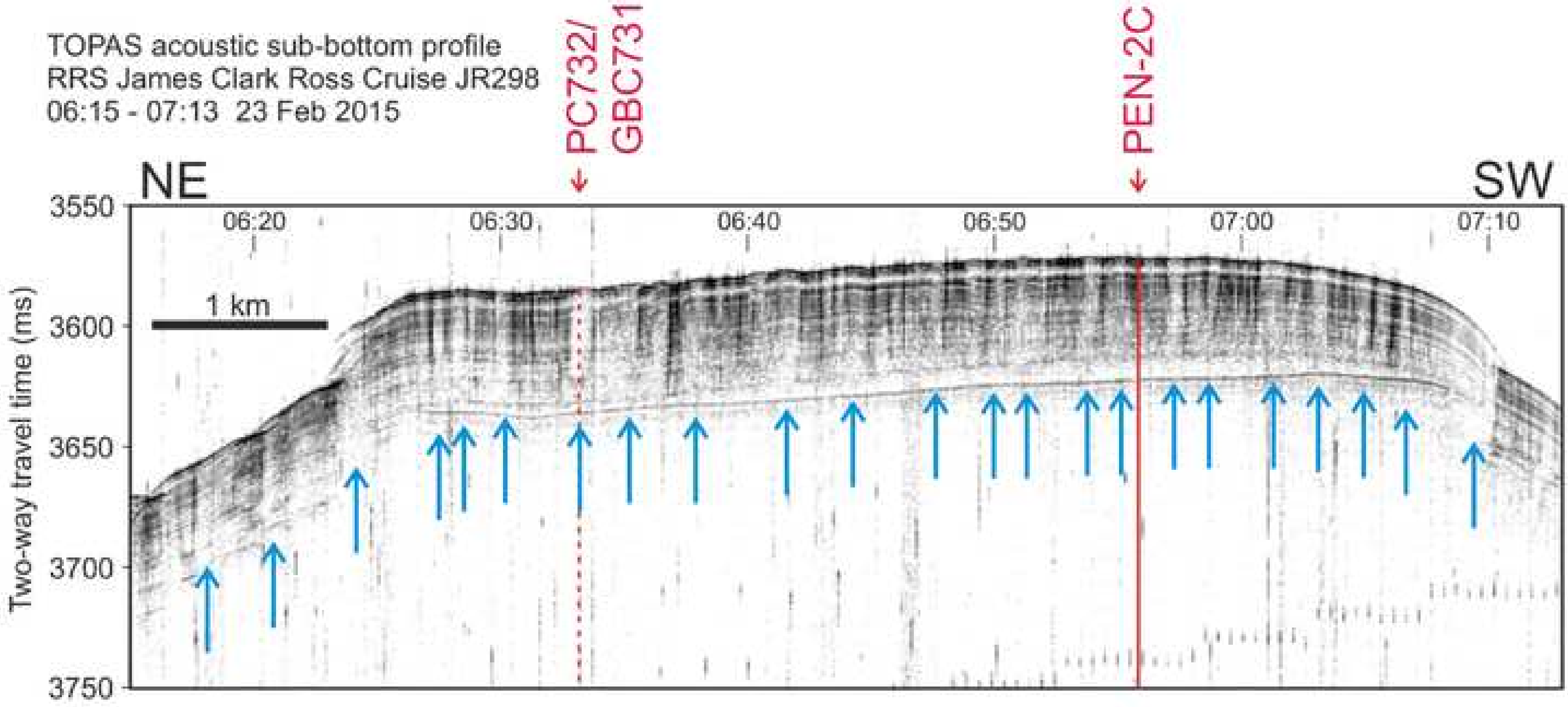
TOPAS acoustic sub-bottom profile
RRS James Clark Ross Cruise JR298
06:15 - 07:13 23 Feb 2015
PC732/
GBC731
PEN-2C
NE
SW
3550
3600
3650
3700
3750
Two-way travel time (ms)
06:20
06:30
06:40
06:50
07:00
07:10
1 km

Suppl_Fig5 Click here to access/download;Figure;Suppl_Fig_5.jpg

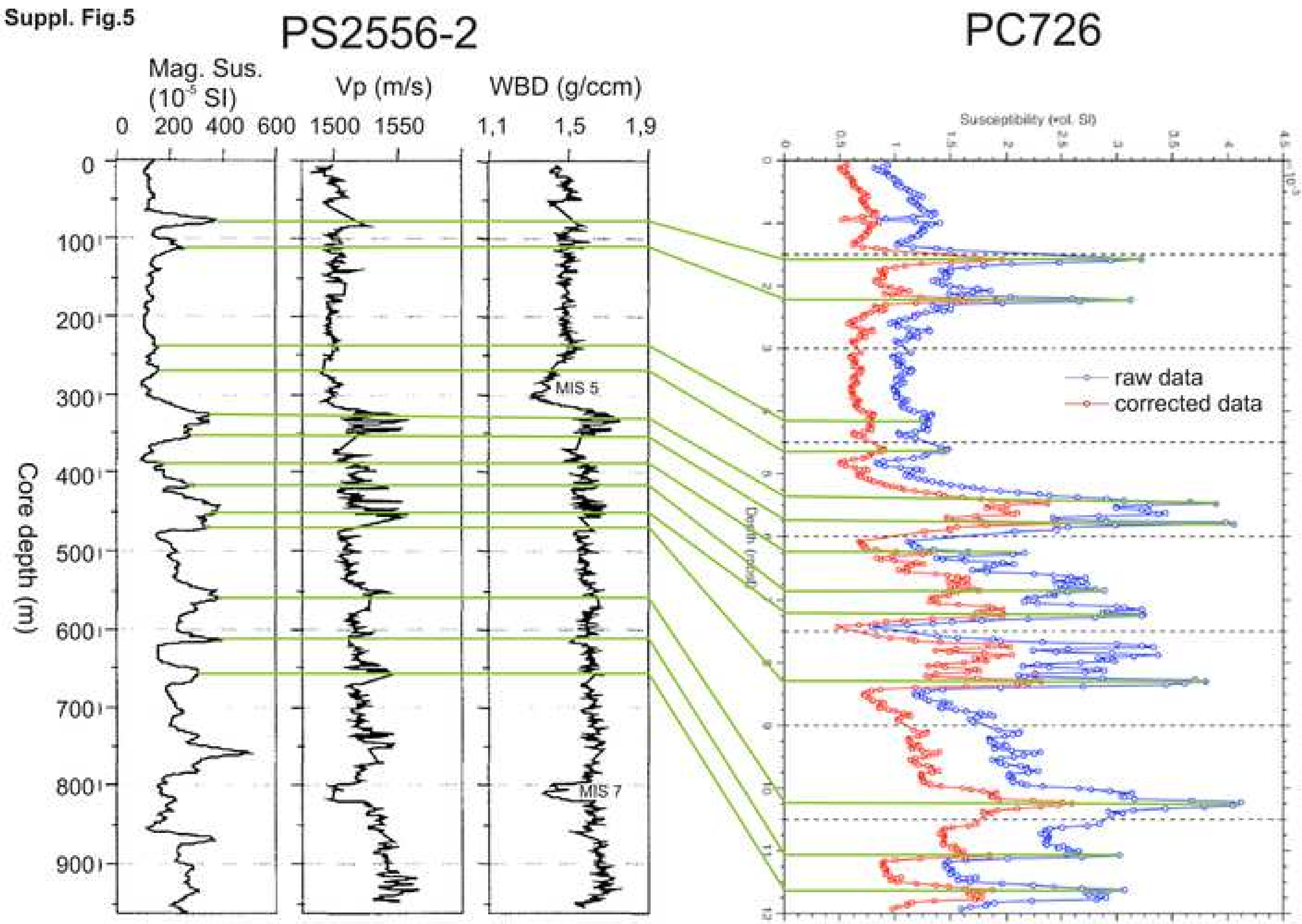

Suppl. Fig.6

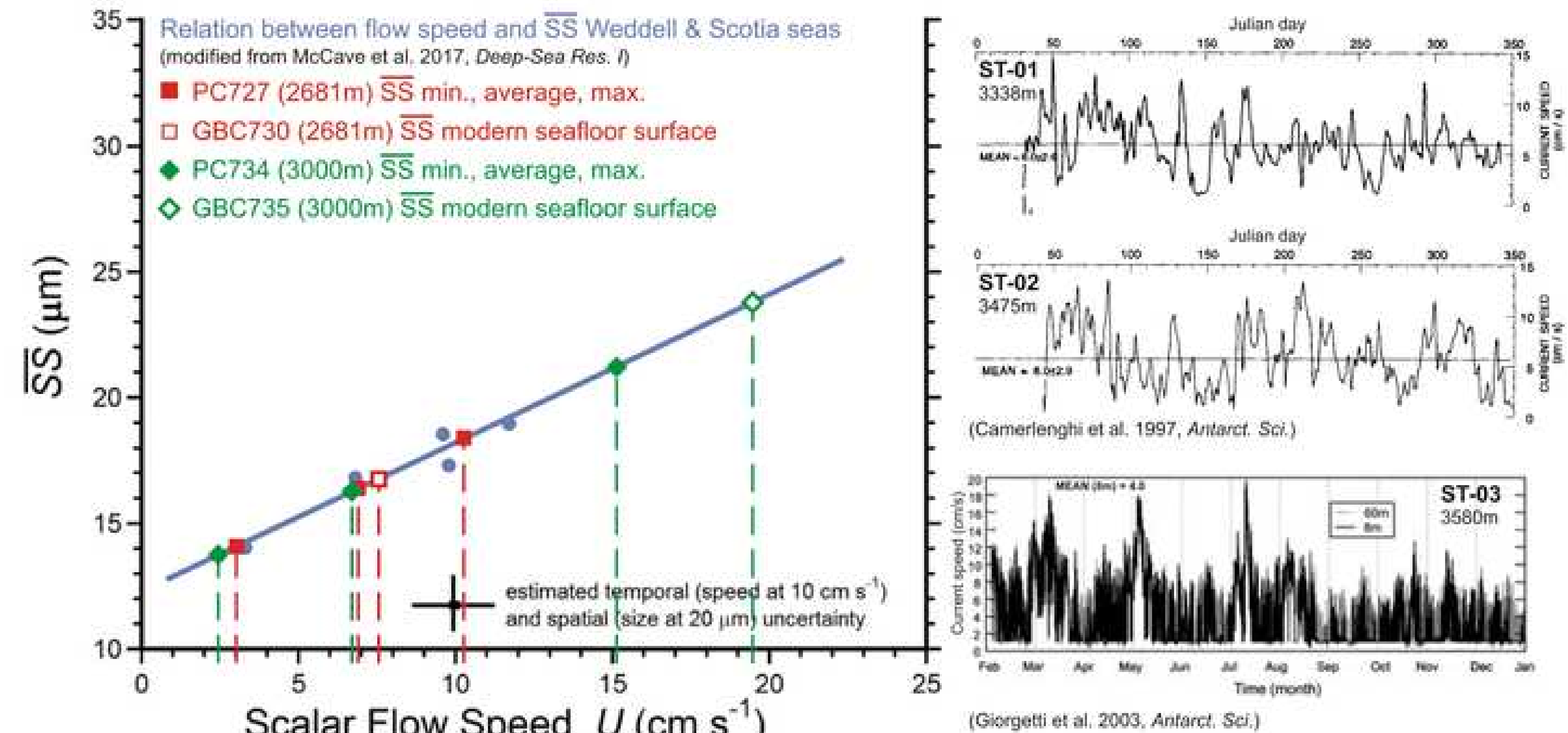
Relation between flow speed and SS Weddell & Scotia seas
(modified from McCave et al. 2017, Deep-Sea Res. I)
PC727 (2681m) SS min., average, max.
GBC730 (2681m) SS modern seafloor surface
PC734 (3000m) SS min., average, max.
GBC735 (3000m) SS modern seafloor surface
estimated temporal (speed at 10 cm s-1)
and spatial (size at 20 μm) uncertainty
SS (μm)
Scalar Flow Speed U (cm s-1)
35
30
25
20
15
10
0
5
10
15
20
25
Julian day
ST-01
3338m
MEAN
CURRENT SPEED
ST-02
3475m
MEAN
(Camerlenghi et al. 1997, Antarct. Sci.)
ST-03
3580m
Current speed (cm/s)
Feb
Mar
Apr
May
Jun
Jul
Aug
Sep
Oct
Nov
Dec
Jan
Time (month)
(Giorgetti et al. 2003, Antarct. Sci.)

Table1

Click here to access/download
Data in Brief
Table 1.docx

Table2

Click here to access/download
Data in Brief
Table 2.docx

Table3

Click here to access/download
Data in Brief
Table 3.docx

Table4

Click here to access/download
Data in Brief
Table 4.docx

Table5

Supplementary_Text

Click here to access/download
Data in Brief
Supplementary_Text.docx